How chemistry controls electron localization in 3d[1] perovskites: a Wannier-function study.

E. Pavarini[1], **A. Yamasaki**[2], **J. Nuss**[2], **and O. K. Andersen.**[2]

[1]INFM and Dipartimento di Fisica "A.Volta," Università di Pavia, Via Bassi 6, I-27100 Pavia, Italy

[2]Max-Planck-Institut für Festkörperforschung, Heisenbergstrasse 1, D-70569 Stuttgart, Germany

E-mail: eva.pavarini@pv.infn.it, A.Yamasaki@fkf.mpg.de, oka@fkf.mpg.de

Abstract. In the series of $3d\,(t_{2g})^1$ perovskites, $SrVO_3$–$CaVO_3$–$LaTiO_3$–$YTiO_3$, the transition-metal d electron becomes increasingly localized and undergoes a Mott transition between $CaVO_3$ and $LaTiO_3$. By defining a low-energy Hubbard Hamiltonian in the basis of Wannier functions for the t_{2g} LDA band and solving it in the single-site dynamical mean-field (DMFT) approximation, it was recently shown (Pavarini *et al* (2004) *Phys. Rev. Lett.* **92** 176403) that simultaneously with the Mott transition there occurs a strong suppression of orbital fluctuations due to splitting of the t_{2g} levels. The present paper reviews and expands this work, in particular in the direction of exposing the underlying chemical mechanisms by means of *ab initio* LDA Wannier functions generated with the Nth order muffin-tin orbital (NMTO) method. The Wannier functions for the occupied oxygen-p band illustrate the importance of oxygen-p to large cation-d covalency for the progressive $GdFeO_3$-type distortion along the series. The oxygen-p orbitals which $pd\sigma$-bond to the cations are the same as those which $pd\pi$-bond to the transition-metal t_{2g} orbitals. As a consequence, the Wannier functions for the t_{2g} band exhibit residual covalency between the transition-metal t_{2g}, the large cation-d, and the oxygen-p states. This residual covalency, which increases along the series, turns out to be responsible not only for the splittings, Δ, of the t_{2g} levels, but also for non-cubic perturbations of the hopping integrals, both of which are decisive for the Mott transition. We find good agreement with the optical and photoemission spectra for all four materials, with the crystal-field splittings and orbital polarizations recently measured for the titanates, and with the metallization volume (pressure) for $LaTiO_3$. The metallization volume for $YTiO_3$ is predicted and the role of the Jahn-Teller distortion is discussed. For use in future many-body calculations, we tabulate the t_{2g} on-site and hopping matrix elements for all four materials and give an analytical expression for the orthorhombic Hamiltonian in the $\mathbf{k}+\mathbf{Q}$ representation. Using conventional super-exchange theory, our on-site and hopping matrix elements reproduce the observed magnetic orders in $LaTiO_3$ and $YTiO_3$, but the results are sensitive to detail, in particular for $YTiO_3$ where, without the JT distortion, the magnetic order would be antiferromagnetic C- or A-type, rather than ferromagnetic. It is decisive that upon increasing the $GdFeO_3$-type distortion, the nearest-neighbour hopping between the lowest and the upper-level Wannier functions becomes stronger than the hopping between the lowest-level Wannier functions. Finally, we show that the non-cubic perturbations responsible for this behaviour make it possible to unfold the orthorhombic t_{2g} LDA bandstructure to a pseudo-cubic zone. In this zone, the lowest band is separated from the two others by a direct gap and has a width, W_I, which is

significantly smaller than that, W, of the entire t_{2g} band. The progressive $GdFeO_3$-type distortion thus favours electron localization by decreasing W, by increasing Δ/W, and by decreasing W_I/W. Our conclusions concerning the roles of $GdFeO_3$-type and JT distortions agree with those of Mochizuki and Imada (2003 *Phys. Rev. Lett.* **91** 167203).

Submitted to: *New J. Phys.*

PACS numbers: 71.27.+a, 71.30.+h, 71.15.Ap, 71.70.Ch, 75.

Contents

1. Introduction

Transition-metal perovskites have been studied for half a century, and most intensively during the last decade, for their fascinating electronic and magnetic properties arising from narrow $3d$ bands and strong Coulomb correlations [1, 2, 3]. The $3d\,(t_{2g})^1$ series $SrVO_3$–$CaVO_3$–$LaTiO_3$–$YTiO_3$ is a paradigm because it has no complicating multiplet effects, a progressing structural distortion illustrated at the top of figure 1, and greatly varying electronic properties: while Sr and Ca vanadate are correlated metals, with optical mass enhancements of respectively ∼3 and ∼4 [4, 5, 6], La and Y titanate are Mott insulators, with gaps of respectively 0.2 and 1 eV [7]. These two Mott insulators, which essentially mark the end points of a series of rare-earth titanates $RTiO_3$,[3, 8] have very different metallization pressures, 11 GPa for $LaTiO_3$ and much larger for $YTiO_3$ [9]. Moreover, they exhibit different orbital physics [10] and, at low temperature, $LaTiO_3$ is a 3-dimensional (G-type) antiferromagnet with T_N=150 K [11] and a small moment of $0.57\,\mu_B$ [12], while $YTiO_3$ is a ferromagnet with a low Curie temperature of T_C=30 K and a good-sized moment of $0.8\mu_B$ [11, 13].

In the Mott-Hubbard picture the metal-insulator transition occurs when the ratio of the on-site Coulomb repulsion to the one-electron bandwidth exceeds a critical value, $(U/W)_c$. As figure 1 shows, in the ABO_3 perovskites the B $3d$ ions are on a nearly cubic (orthorhombic) lattice and at the centres of corner-sharing O_6 octahedra. The $3d$ band thus splits into covalent O p B d π antibonding t_{2g} bands and covalent O p B d σ antibonding e_g bands, of which the former lie lower, have less O character, and couple less to the octahedra than the latter. Simple theories for the d^1 perovskites [2] are based on a Hubbard model with three independent, two-dimensional, *degenerate*, $\frac{1}{6}$-filled t_{2g} bands per B ion, and the variation of the electronic properties along the series is ascribed to a progressive reduction of W due to the increased bending of the $pd\pi$ hopping paths, the B-O-B bonds seen in figure 1.

But this need not be the whole story, because the value of $(U/W)_c$ is expected [14] to decrease with decreasing degeneracy. Such a decrease of degeneracy can be achieved by splitting the t_{2g} levels by merely ZW, the reduced bandwidth associated with quasiparticle excitations in the correlated metal [15]. As a consequence, if the level-splitting increased along the series, this could significantly influence the Mott transition.

However, unlike in e_g band perovskites, where large (10%) cooperative Jahn-Teller (JT) distortions of the oxygen octahedron indicate that the orbitals are not degenerate but spatially ordered, the octahedron in the t_{2g} band perovskites is nearly perfect. For that reason the t_{2g} orbitals have often been assumed to be degenerate. If that is the case, quantum fluctuations will lead to an orbital *liquid* [10, 16, 17] rather than orbital ordering in the Mott insulating phase. The observation of an isotropic, small gap spin-wave spectrum both in antiferromagnetic $LaTiO_3$ and also in ferromagnetic $YTiO_3$ [10] has lent support to this orbital-liquid scenario, because if the orbital moments were quenched, such a spectrum would seem accidental. On the other hand, the predicted contribution to the specific heat from the orbital liquid has not been observed in $LaTiO_3$

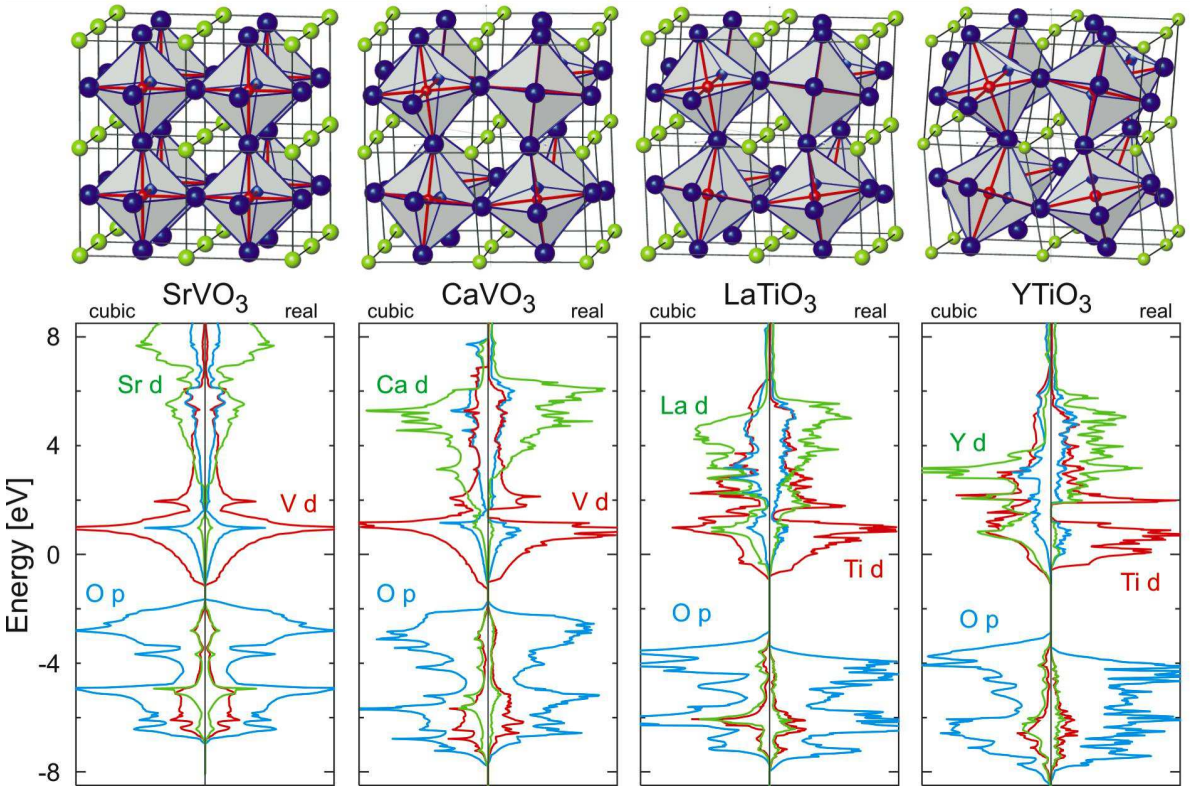

Figure 1. Crystal structures and electronic bandstructures for the series of $3d\,(t_{2g})^1$ orthorhombic ABO_3 perovskites considered in this paper; A (green) B (red) O (blue). The bottom part shows densities of one-electron states (DOSs) calculated in the LDA for the real structures (right-hand panels) and for hypothetical, cubic structures with the same volumes (left-hand panels). The green, red, and blue DOSs are projected onto, respectively, A d, B $3d$, and O $2p$ orthonormal orbitals [41]. The B $3d\,(t_{2g})$ bands are positioned around the Fermi level (zero of energy) and their widths, W, decrease from $\sim$3 to $\sim$2 eV along the series. The much wider B $3d\,(e_g)$ bands are at higher energies. This figure resulted from linear muffin-tin orbitals (LMTO) calculations in which the energies, $\epsilon_{\nu Rl}$, of the linear, partial-wave expansions were chosen at the centres of gravity of the *occupied,* partial DOS. Since those energies are in the O p band, the LMTO errors proportional to $(\varepsilon - \epsilon_{\nu Rl})^4$ slightly distort the *un*occupied parts of the DOS.

[18]. Moreover, a 3% JT stretch of one of the basal O squares into a rectangle was recently discovered in $LaTiO_3$ [12, 19]. This is of similar magnitude as the JT distortion known to exist in $YTiO_3$ where, however, the square is stretched into a rhomb [20].

By *ab initio* calculation of the Wannier functions of the LDA t_{2g} band, it was recently found [21] that in $LaTiO_3$ and $YTiO_3$ the t_{2g} degeneracy is lifted at the classical level. This is *not* due to the small JT distortions, but to the $GdFeO_3$-type distortion which tilts and rotates the corner-sharing octahedra as illustrated in figure 2. As we shall see in the present paper, this distortion is partly driven by the covalency between occupied oxygen p states and empty A-cation d states, which pulls each O1 (O2) closer to *one* (*two*) of its four nearest A neighbours. As a result, each A cation has 4 of its

12 near oxygens pulled closer in. In addition, the A cube gets distorted so that *one* diagonal becomes the shortest. The t_{2g} degeneracy is now lifted, essentially by residual covalent interactions between empty A d orbitals and full B t_{2g} and O p orbitals, the details of which are different in $LaTiO_3$ and $YTiO_3$. These residual covalent interactions not only perturb the on-site, but also the hopping matrix elements of the Hamiltonian.

Already forty years ago, Goodenough [22] speculated that covalency between occupied O p and empty A d orbitals may be a driving force behind the $GdFeO_3$-type distortion, and this hypothesis was recently supported in an extensive series of semiempirical simulations [23].

That the $GdFeO_3$-type distortion lifts the t_{2g} degeneracy in the titanates had been realized slightly earlier by Mochizuki and Imada [24], but only after a long search by them and other groups for a model Hamiltonian which could reproduce all observed magnetic and orbital orderings [25, 26, 27, 28, 29]. These model Hartree-Fock and strong-coupling studies for the entire family of $3d^n$ perovskites mapped out the roles played JT distortions, spin-orbit coupling, e_g degrees of freedom, orbital misalignment caused by the $GdFeO_3$ distortion, and, finally, by the electrostatic field and hybridization from the A cations which enter via the $GdFeO_3$-type distortion.

What enabled the single, independent study in reference [21] to reach the same conclusion concerning the role of the $GdFeO_3$-type distortion, was the use of parameter-free density-functional (LDA) theory to generate t_{2g} Wannier functions for a representative series of real materials by means of a new technique [30]. The point is that it is virtually impossible to know *a priori* which on-site and hopping matrix elements are important, and what their values are. To extract them with the required accuracy from experiments and/or from LDA bandstructures is often impossible, and in this respect the t_{2g} perovskites are particularly nasty: at first sight, the t_{2g} Hamiltonian of these nearly cubic materials is the simplest possible, but cation covalency in the presence of $GdFeO_3$-type distortion makes it far more complicated than, *e.g.*, the e_g Hamiltonian relevant for the $t_{2g}^3 e_g^1$ manganites, which have similar $GdFeO_3$ distortions. The reason is that the t_{2g} orbitals interact with the *same* oxygen p orbitals as the cation orbitals do. This is not the case for e_g orbitals.

Now the problem that relevant parameters might be overlooked in model calculations occurs less frequently with the LDA+U method, because this method uses a complete basis set. In fact, at about the time when Mizokawa and Fujimori [25] carried out their pioneering model calculations, Solovyev, Hamada, Sawada, and Terakura [31, 32] performed LDA+U calculations in which the value of the on-site Coulomb repulsion, U, was adjusted to the observed optical gaps. Those calculations yielded the correct magnetic orders in $LaTiO_3$ and $YTiO_3$, but the underlying mechanism was not recognized. The magnetic moment and orbital order predicted for $YTiO_3$ were subsequently confirmed by NMR [33] and neutron scattering [34].

The static mean-field approximation used in Hartree-Fock and LDA+U calculations cannot describe the paramagnetic-metal to paramagnetic-insulator (Mott) transition. To be more specific, this approximation is inadequate for strongly correlated metals

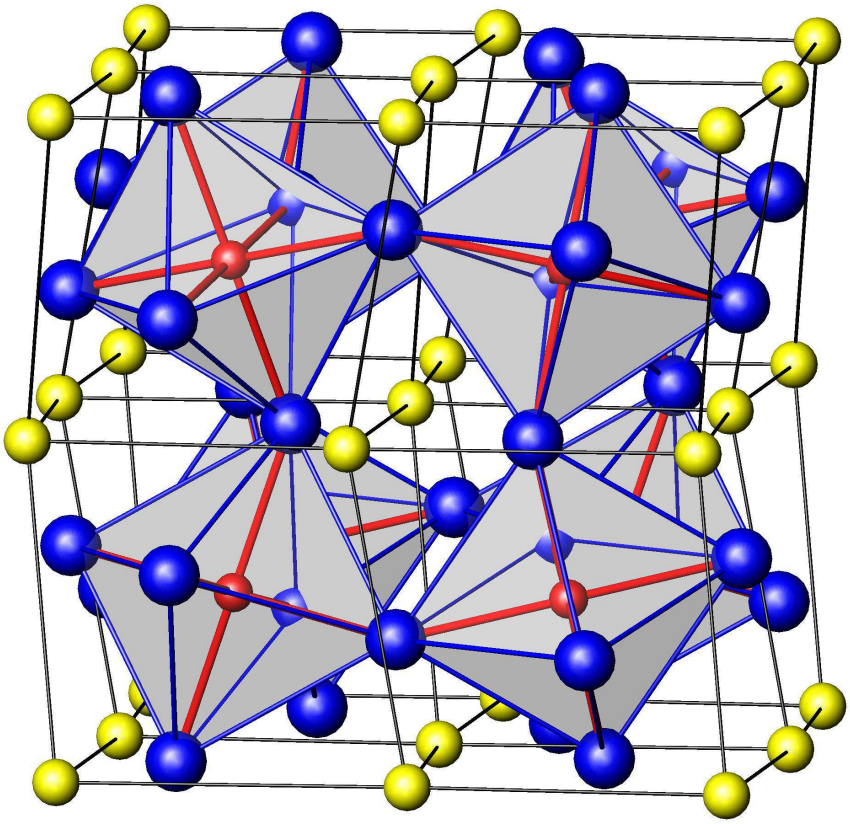

Figure 2. Crystal structure of a $GdFeO_3$-distorted ABO_3 perovskite ($YTiO_3$) in *Pbnm* symmetry. The horizontal AO-planes perpendicular to the z-axis are mirrors. The global x-axis points outward in the front and the y-axis to the right. The B-sites (red) form a primitive monoclinic, nearly cubic lattice with the following translation vectors: $\mathbf{R}_x = [1 + (\beta + \alpha)/2]\,\hat{\mathbf{x}} + [(\beta - \alpha)/2]\,\hat{\mathbf{y}}$, $\mathbf{R}_y = [(\beta - \alpha)/2]\,\hat{\mathbf{x}} + [1 + (\beta + \alpha)/2]\,\hat{\mathbf{y}}$, and $\mathbf{R}_z = (1 + \gamma)\,\hat{\mathbf{z}}$ with α, β and γ small. The latter vector is orthogonal to the two former, which have the same length, but need not be quite orthogonal to each other. For $LaTiO_3$ ($YTiO_3$), $|\hat{\mathbf{x}}| = |\hat{\mathbf{y}}| = |\hat{\mathbf{z}}| = 397.1$ (385.8) pm and $\alpha = 33$ (-258), $\beta = 1$ (407), $\gamma = -33$ (-137) $\times 10^{-4}$. The position of a B-site is: $\mathbf{R} = x\mathbf{R}_x + y\mathbf{R}_y + z\mathbf{R}_z$ with x, y, and z integers. The structure is orthorhombic with 4 ABO_3 units per cell, *e.g.*, the four in the front plane, which we shall label 1 (bottom left, xyz=000), 2 (bottom right, 010), 3 (top left, 001) and 4 (top right, 011). The orthorhombic translation vectors are: $\mathbf{a} = (\hat{\mathbf{x}} - \hat{\mathbf{y}})(1 + \alpha) = \mathbf{R}_x - \mathbf{R}_y$, $\mathbf{b} = (\hat{\mathbf{x}} + \hat{\mathbf{y}})(1 + \beta) = \mathbf{R}_x + \mathbf{R}_y$, and $\mathbf{c} = 2\hat{\mathbf{z}}(1 + \gamma) = 2\mathbf{R}_z$. Reflection in a vertical bc-plane containing a B-site ($a \leftrightarrow -a$, or equivalently, $x \leftrightarrow y$), followed by a translation $\mathbf{R}_y = \frac{1}{2}(\mathbf{b} + \mathbf{a})$, takes the crystal into itself (glide plane). All A-ions (yellow) and all B-ions (red) are equivalent, but there are two kinds of oxygen (blue): O1 in a mirror A-plane, and O2 in a vertical, buckled A-plane. Proceeding along the series in figure 1, the $GdFeO_3$-type distortion tilts the corner-sharing octahedra by 0, 9, 13 (12), and 20° around the b-axes in alternating directions, and rotates them around the c-axis by 0, 7, 10 (9), and 13° in alternating directions [12, 20, 42, 43]. Here, the values in parentheses are from the older data [44].

and for Mott insulators at temperatures above the magnetic ordering temperature. For such purposes, the dynamical mean-field approximation (DMFT) [35] has recently been developed and applied to solve low-energy Hubbard Hamiltonians derived from the LDA [36]. The calculations reported in reference [21] employed the above-mentioned basis of LDA t_{2g} Wannier functions, and a single, adjusted value of U for all four materials. This implementation of the LDA+DMFT approach properly describes orbital fluctuations in the multiband Hubbard model by including the *off*-diagonal mm'-matrix elements of the self-energy matrix, taken to be local in DMFT. All earlier implementations had used a scalar self-energy, as is appropriate for cubic systems [37, 38]. A recent LDA+DMFT calculation for $La_{1-x}Sr_xTiO_3$ used the eigenrepresentation of the on-site LDA Hamiltonian and then neglected the off-diagonal elements of the self-energy [39], apparently a reasonable approximation for this system.

This paper is a pedagogical review of the calculations reported in reference [21] and a presentation of many new results. The use of LDA Wannier functions to bring out the materials aspects is emphasized. The paper takes off (section 2) with a discussion of the chemistry: after analyzing the high-energy part of the LDA bandstructures displayed in figure 1, we demonstrate the role of O-A covalency in driving the progressive $GdFeO_3$ distortion. In particular, we visualize the bonds by means of the O $2p$ Wannier functions. In section 3, we zoom in on the low-energy LDA t_{2g}-bands and discuss their Wannier functions, first in the cubic xy, yz, xz-representation and then in the crystal-field representation. The influence of the $GdFeO_3$-type and JT distortions on the orbital energies, inter-orbital couplings, and the bandstructures is discussed in detail, and the on-site and hopping integrals are tabulated for use in future many-body calculations. In section 4 we set up the t_{2g} Hubbard Hamiltonian and explain how it is solved with the DMFT many-body technique. Using the same value of U for all four materials, the resulting high-temperature electronic structures are presented in section 5. They reproduce the increased localization observed along the series, including the mass enhancements, the Mott transition, and the gap sizes. For the Mott insulators, it turns out that the Coulomb correlation localizes the electron almost exclusively in one orbital, and more so for $YTiO_3$ than for $LaTiO_3$, and that this orbital is the eigenfunction of the lowest t_{2g} level in the LDA. The roles of band-width reduction and level splittings are analyzed, and it is concluded that these alone do not suffice to explain the strong decrease of $(U/W)_c$ found by DMFT when progressing through the series. We then compute the metallization volumes for the titanates, compare with most recent high-pressure experiments [9], and discuss the role of the $GdFeO_3$-type and JT distortions. In order to further elucidate the difference in the electronic structure of the Mott insulators $LaTiO_3$ and $YTiO_3$ we present calculations of the onset of the optical conductivity. In section 6 we use our computed orbital orders and hopping integrals to calculate the magnetic exchange couplings, J_{se}, within conventional super-exchange theory. Reasonable agreement with the observed magnetic orders is obtained, but –as evidenced by the extensive model calculations [25, 26, 27, 28, 29], and as pointed out by Ulrich *et al.* [40] – such J_{se} values are extremely sensitive to detail, in particular in

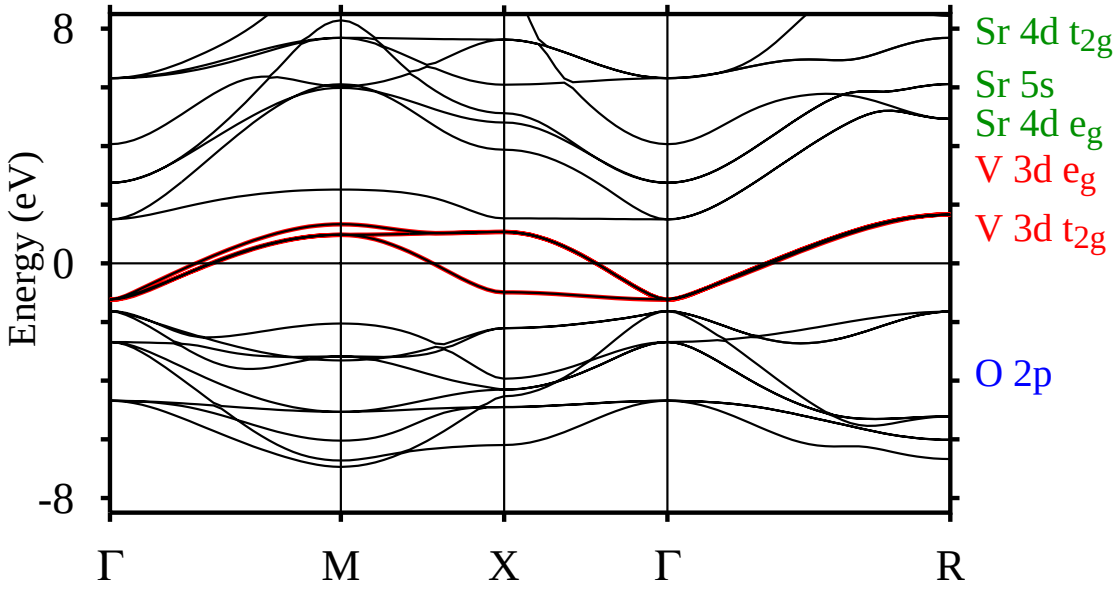

Figure 3. LDA bandstructure of cubic $SrVO_3$. The Brillouin zone (BZ) is shown in blue in figure 9. As is discussed in appendix A, the bands obtained with the downfolded, truly minimal V $3d\,(t_{2g})$ NMTO basis (red) are indistinguishable from those obtained with the full NMTO basis (black).

$YTiO_3$ where we find the small JT distortion to be decisive for the ferromagnetism. In section 7 we uncover the ingredient so far missing in our understanding of the calculated trend in $(U/W)_c$, namely the formation of a lowest subband, whose width is significantly smaller than W. Specifically, the Nth-order muffin-tin orbitals (NMTO) method enables us to show that the complicated orthorhombic LDA t_{2g} bandstructures for the titanates can be approximately folded out to a pseudo-cubic zone and that, in this representation, the lowest band is separated from the two upper bands by a direct gap. The development of this orbitally ordered band from the three degenerate cubic bands is explained and the relation to the increasing tendency towards ferromagnetism with increasing $GdFeO_3$-distortion is pointed out. In section 8 we sum up our main conclusions. Appendix A explains how downfolding within the NMTO method [30] is used to construct truly minimal basis sets which pick out selected bands, such as the O p or B t_{2g} bands. When symmetrically orthonormalized, such a truly minimal basis set constitutes a set of atom-centred, highly localized Wannier functions. Finally, since a weak point of the present calculations is our use of the standard LMTO-ASA method [41] to generate the LDA potentials, we give the technical details in appendix B.

2. High-energy LDA bandstructures and O-A covalent mechanism of the $GdFeO_3$-type distortion

In the present section we shall use the LDA bandstructures shown in figures 1, 3, and 4, as well as the oxygen p band Wannier functions, to demonstrate the role of O p − A d covalency for the $GdFeO_3$-type distortion, and the role of O p − B d covalency for the stability of the octahedron and the splitting of the B $3d$ band into separate t_{2g} and e_g bands. This will set the stage for understanding the role of covalency for the splitting of the t_{2g} levels.

Apart from providing insights into the bonding, the LDA bands –except for the t_{2g} bands, which we shall treat separately with a Hubbard model– give information about the one-electron high-energy excitations. Specifically, we shall approximate these excitations by the LDA Hamiltonian plus a self-energy, $\Sigma(\varepsilon)$, which only couples inside t_{2g} space and is independent of the crystal momentum, $\mathbf{k}$. To compute this self-energy is the task of the LDA+DMFT to be considered in section 4. Future calculations might choose to include in the many-body calculation a larger basis set of Wannier functions than those describing merely the low-energy t_{2g} bands. For that reason, too, it makes sense to consider first the high-energy LDA band structure and the O p Wannier functions.

2.1. Bandstructures

The bottom part of figure 1 exhibits densities of states (DOSs) projected onto various groups of orbitals, O p, B d, and A d, of a standard set of nearly orthonormal LMTOs [41]. These DOS projections provide information about the mixing of characters due to hybridization between various kinds of orbitals. Consider for instance the panel relating to $SrVO_3$: in the O p bands (mainly blue), we see V d character (red), and in the V d bands (mainly red), we see O p character (blue). This hybridization between the O p and the V d bands has pushed them apart, and since the oxygen bands are occupied and the V d bands are nearly empty, band-structure energy has been gained; this is O-B covalency. Some orbitals hybridize more than others, *e.g.*, σ bonds are stronger than π bonds, and it is therefore the lower part of the O p band and the upper, e_g part of the V d band which have the most foreign character mixed in. The less familiar result of this figure is that it also exhibits a large amount of O-A (blue-green) covalency. We shall see that this is because each oxygen has two p orbitals σ bonding with Sr, but only one σ bonding with V. That, to some extent, compensates for the distance to Sr being $\sqrt{2}$ longer than the distance to V.

When we move along the series $SrVO_3$–$CaVO_3$–$LaTiO_3$–$YTiO_3$ a tilt is expected if the ionic radius is such that the Goldschmidt tolerance factor, $(r_A + r_O)/\left[\sqrt{2}\,(r_B + r_O)\right]$, is smaller than 1. The radii satisfy: $r_{Sr^{2+}} \sim r_{La^{3+}} > r_{Ca^{2+}} \sim r_{Y^{3+}}$, while $r_{V^{5+}} < r_{Ti^{4+}}$ (in this scheme the d electron is taken as localized), and the tolerance factor decreases by about 10% along the series, although it is the same for $CaVO_3$ and $LaTiO_3$. The progressive tilt is thus partly due to the fact that the size of

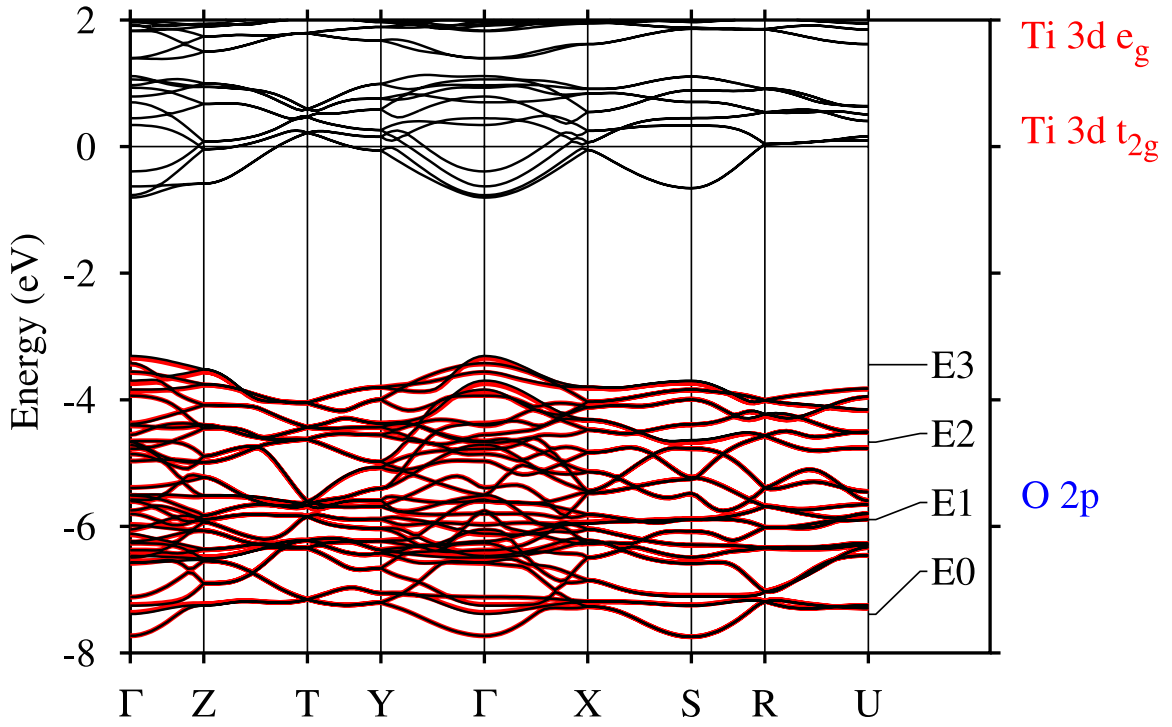

Figure 4. LDA bandstructure of orthorhombic $LaTiO_3$. The Brillouin zone is shown in red in figure 9. The bands obtained with the truly minimal (downfolded) O $2p$ NMTO basis (red) are indistinguishable from those obtained with the full NMTO basis (black). This is explained in appendix A. The basis functions of the truly minimal set are shown in figures 5 and 6. The recent structural data [12] was used.

the A cation shrinks in relation to that of the BO_3 octahedron. However, as pointed out by Woodward [23], this does not explain why the tilt is of the $GdFeO_3$-type. This type, he found by using empirical interatomic potentials and the extended Hückel method, is unique in maximizing the O-A covalent bonding at the same time as minimizing the O-A repulsive overlap. Our LDA calculations support and detail the importance of O-A covalency for the $GdFeO_3$-type distortion:

It is well accepted that equilibrium crystal structures, such as those shown at the top of figure 1, may be computed *ab initio* with good accuracy using the LDA. In the bottom right-hand panels we therefore show the LDA densities of states (DOS) calculated for the real structures –determined experimentally though [20, 42, 43, 44]– and in the bottom left-hand panels we show the LDA DOS calculated for hypothetical, cubic structures with the same volume. Now, the energy gain associated with a structural distortion is approximately the gain in band-structure plus Madelung energy, so let us consider the trend in the former:

For $SrVO_3$ the left- and right-hand panels are identical because the real structure of $SrVO_3$ is cubic. Each Sr ion is at the corner of a cube and has 12 nearest oxygens at the face centres. Going now to cubic $CaVO_3$ the empty $3d$ band of Ca lies lower and thereby closer to the oxygen $2p$ band than the empty $4d$ band of Sr. It is therefore

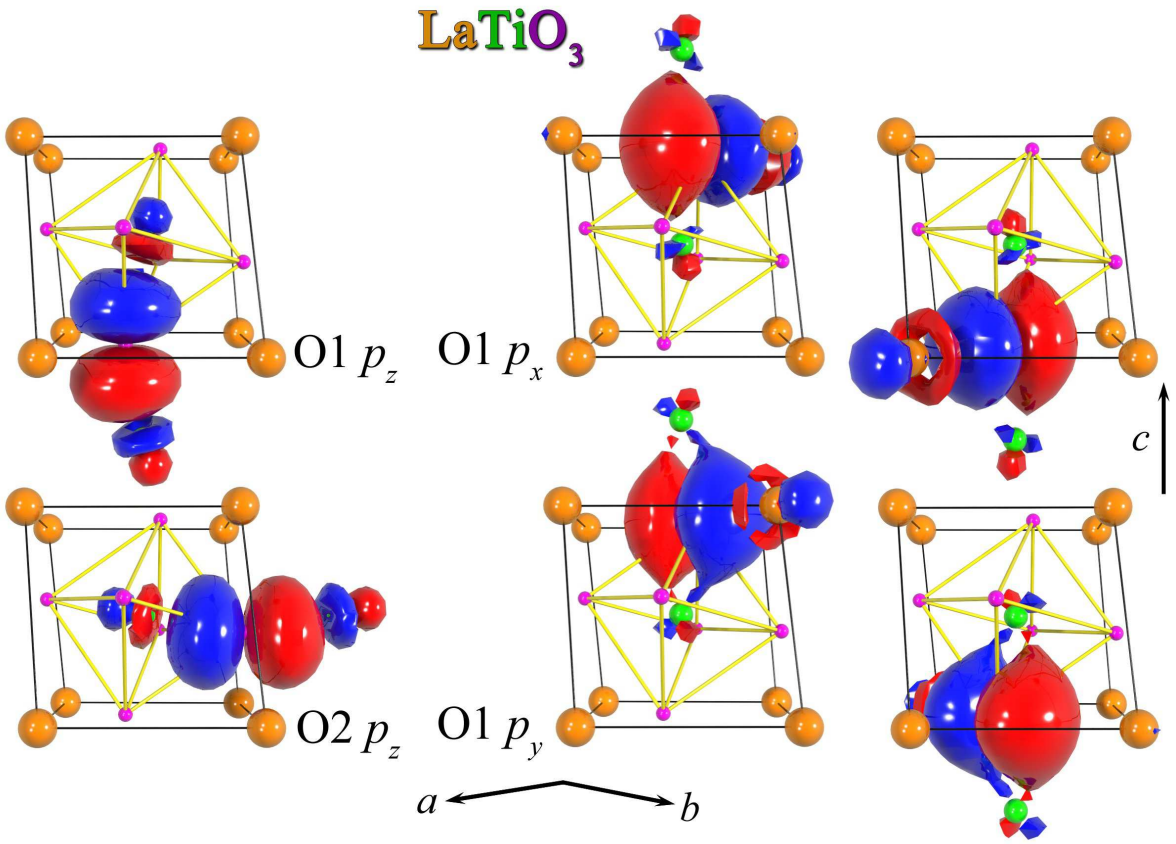

Figure 5. Basis functions of the truly minimal set of O $2p$ NMTOs calculated for $LaTiO_3$ with the structure of reference [12]. Shown are the orbital shapes (constant-amplitude surfaces) with the $\pm$ signs labelled by red and blue. O1 is in a flat face of the distorted La cube and the O2s are in the buckled faces (see caption to figure 2). In column 1 we show the orbitals perpendicular to the faces (p_z) which exhibit symmetric Ti-O-Ti σ-bonds. In column 2 we show the orbitals in the top horizontal face (O1 p_x and p_y). Although they are equivalent to those in the bottom face shown in column 3, we show both for the sake of clarity. The O1 p_x and p_y orbitals, as well as those for O2 shown in the following figure 6, exhibit weak, symmetric Ti-O-Ti π-bonds. Most importantly, however, the O1 p_x and p_y orbitals show asymmetric O-La σ-bonds. The latter, together with the O2 p_x - La σ-bonds shown in figure 6, are responsible for the $GdFeO_3$-type distortion. This O-A bonding is shown schematically in figure 7.

conceivable that a $GdFeO_3$-type distortion which pulls some of the oxygen neighbours closer to the A ion and thereby increases the covalency with those, is energetically more favourable in $CaVO_3$ than in $SrVO_3$, and this is what the figure shows: an increase of the O $2p$-Ca $3d$ gap associated with the distortion in $CaVO_3$. The Ca $3d$ character is essentially swept out of the lower part of the V $3d$ band.

When proceeding to the titanates, the A and B cations become 1st- rather than 3rd-nearest neighbours in the periodic table. The B $3d$ band therefore moves up and the A d band down with respect to the O p band. Hence, the O-B covalency decreases and the O-A covalency increases. Most importantly, the A d band becomes nearly degenerate with

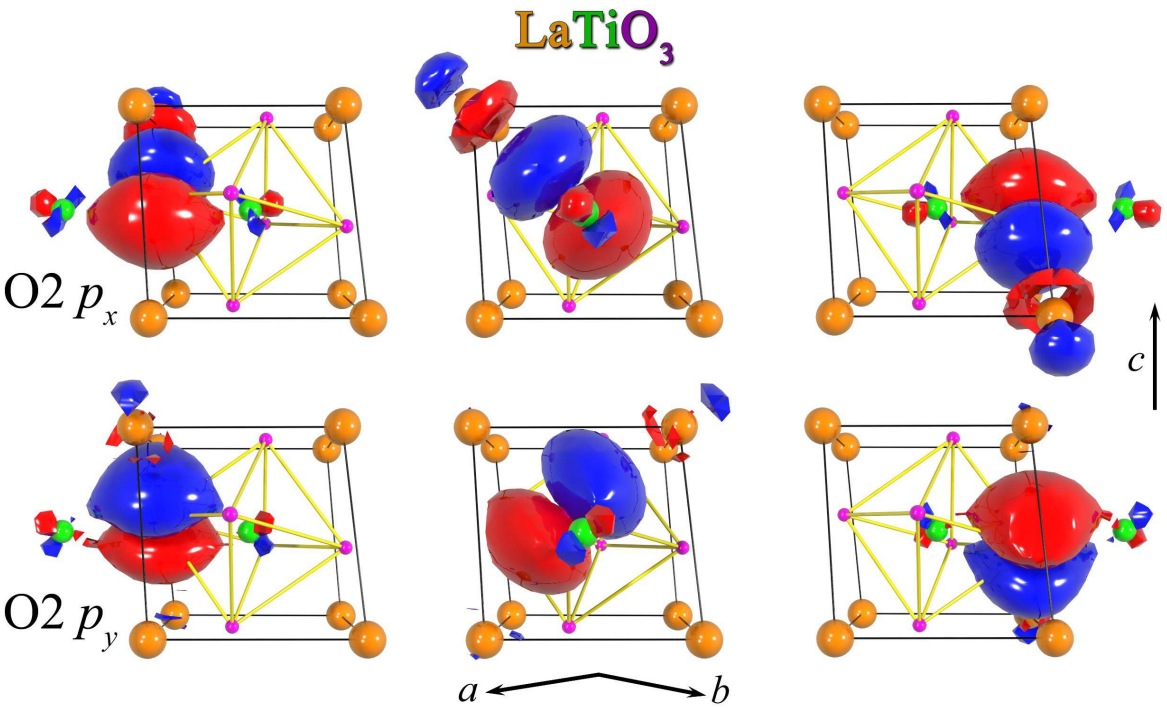

Figure 6. Same as figure 5, but for the oxygen orbitals (O2 p_x and p_y) in the buckled faces of the distorted La cube. O2 p_x is seen to bind much stronger to La than O2 p_y. The orbitals in the 1st and 3rd columns are equivalent, but for clarity we show both. Not shown are the orbitals on the rear face since they are equivalent to those in the front face shown in the 2nd column. The rear p_x orbital binds strongly to La at the bottom right corner. The O-A bonding is summarized in figure 7.

the Ti $3d$ band, and more so for Y $4d$ than for La $5d$. It is only the $GdFeO_3$-distortion which, through increase of the O $2p$-A d hybridization, pushes the A d band above the Fermi level. This, as well as the concomitant lowering of the O $2p$ band with respect to ϵ_F, can be seen in the figure.

In the series of trivalent rare-earth titanates, the $GdFeO_3$-type distortion –and the low-temperature magnetic properties– are known to change gradually from those of $LaTiO_3$ to essentially those of $YTiO_3$ [3]. This trend follows the decrease of the ionic radius and of the $5d$ level position.

2.2. Oxygen p bonds

The covalent bonds can be visualized by a set of localized Wannier functions for the *occupied* bands, *i.e.* the O $2p$ bands. Here we shall not consider the much smaller contribution from the O $2s$ bands. In figure 4 we illustrate for the case of $LaTiO_3$ that we can construct a set of O p NMTOs which span the O $2p$ bands, and no other bands. This basis set contains as many orbitals as there are occupied bands and, hence, it is what we call a *truly minimal* basis set. Its inequivalent orbitals are shown in figures 5 and 6. Each oxygen has two nearest B neighbours and four near A neighbours, and we

have chosen its three p orbitals such that one of them, call it p_z, points approximately towards the B neighbours (see caption to figure 2), and the two other orbitals, labelled p_x and p_y, point approximately towards two of the four A neighbours.

Only the *central* parts of these orbitals have respectively p_x, p_y, or p_z character, because in order to describe the hybridization of the O $2p$ band with the B and A derived bands, the orbitals of a truly minimal set must have those characters folded into their tails. In fact, *all* partial-wave characters *other* than oxygen p are folded into the O p set. Now, as is explained in appendix A, the NMTOs are localized by construction, but they are not quite orthogonal. Therefore, in order to become a set of localized Wannier functions, the truly minimal set must be symmetrically orthonormalized. The sum of the squares of these Wannier functions is the valence charge density, and the sum of their orbital energies is the band-structure energy (except for a small contribution from the B $3d$ electron). Hence, the truly minimal set of O $2p$ NMTOs shown in figures 5 and 6 visualizes the covalent bonds.

From the first column in figure 5 we see that each oxygen forms *one* strong Ti-O-Ti covalent, symmetric σ bond with its two Ti neighbours, the Ti character being $3d\,(e_g)$ with a bit of $4sp$. From the right-hand side of the figure, we see that each oxygen orbital in the horizontal, flat face of the distorted La cube (O1 p_x or p_y) forms a weak Ti-O-Ti covalent, symmetric π bond, the Ti character being predominantly $3d\,(t_{2g})$. As may be seen from figure 6, the same holds for each oxygen orbital (O2 p_x or p_y) in the vertical, buckled faces. The respective O-Ti covalent interaction pushes the anti-bonding Ti $3d\,(e_g)$-like band well above the Ti $3d\,(t_{2g})$-like band, as we saw in figure 1.

Most importantly, however, figure 5 shows that *each* of the two oxygen orbitals in the flat faces (O1 p_x or p_y) forms an O-A covalent, asymmetric σ bond with *one* of the two La neighbours towards which it points. It is clearly seen how the weight of the orbital is shifted from one towards the other La ion. Moreover, we see that the bond with O1 p_x is somewhat stronger than with O1 p_y. The La character of the O1 p_x orbital is $5d_{3x^2-1}$ with some by-mixing of $6sp$. This d character is mostly t_{2g}, because with x and y along the cubic directions, it is $d_{\frac{3}{2}(x\pm y)^2-1} = \mp\frac{\sqrt{3}}{2}d_{xy} - \frac{1}{2}d_{3z^2-1}$. Figure 6 shows that for the buckled faces of the distorted La cube, only *one* of the oxygen orbitals, O2 p_x, bonds significantly to La, and that this bonding is as strong as for O1 p_x. As a result, we obtain the schematic picture of the O-A covalent σ bonds shown in figure 7. The resulting $GdFeO_3$-type distortion shortens the two O1 bonds by respectively 17% (15%) and 11% (8%) of the average of the four O1-La distances, and it shortens the O2 bond by 16% (14%) of the average of the four O2-La distances [12]. Here the numbers in parentheses are from the older data [44]. For $CaVO_3$ the corresponding bond-length reductions are 10% and 4% for O1 and 12% for O2, while for $YTiO_3$, they are as large as 28% and 23% for O1, and 22% for O2. For $YTiO_3$ the shortest O-Y distance is, in fact, only 10% longer than the O-Ti distance.

Also indicated in figure 7 is the oxygen coordination of the A cations, which is reduced from 12-fold and cubic to 4-fold and roughly tetrahedral. The embedding of the unit in the entire structure can be understood by comparison with figure 2, where

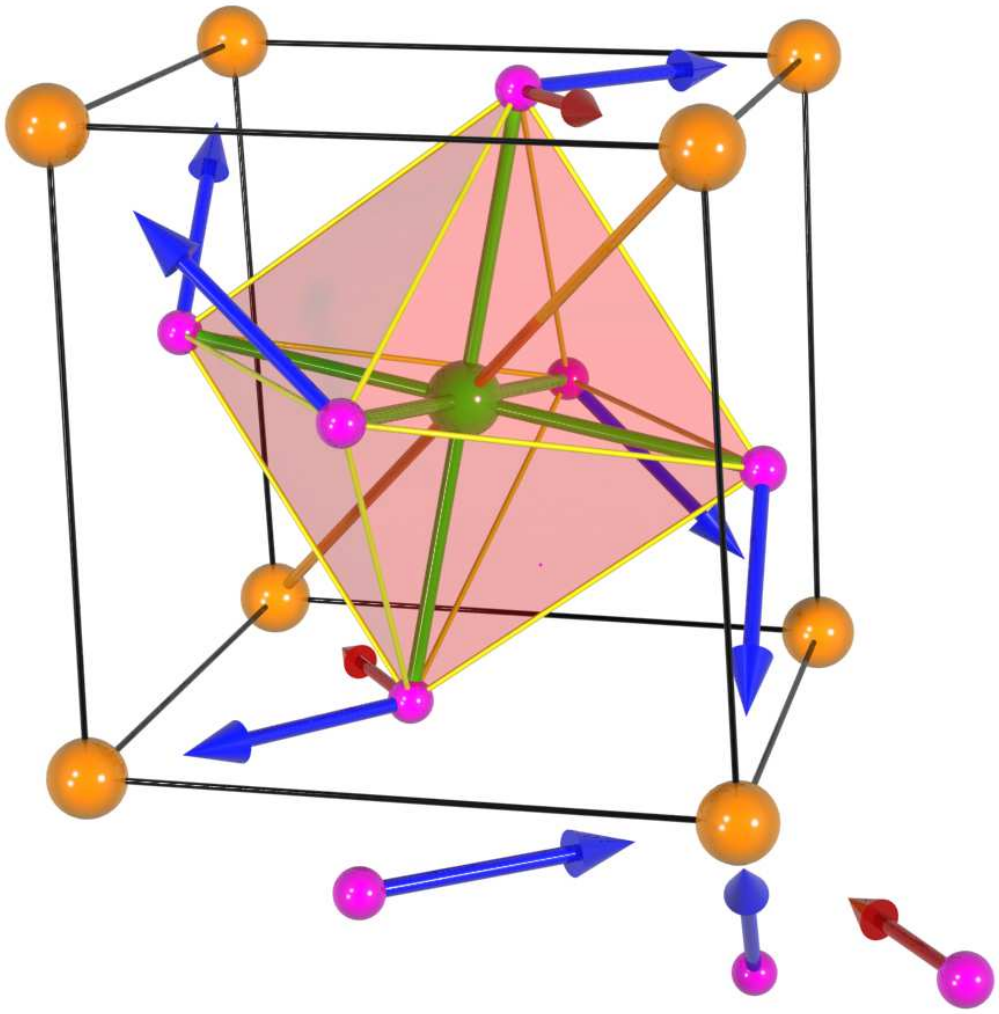

Figure 7. Schematic representation of the O-A covalent bonds shown for $LaTiO_3$ in figures 5 and 6: O1 binds to *two* while O2 binds to *one* of the four A-neighbours. One of the two O1-A bonds is relatively weak and is indicated by a short, red arrow. The resulting $GdFeO_3$-type distortion shortens the O-A bonds correspondingly. In $CaVO_3$, $LaTiO_3$, and $YTiO_3$, the shortest O1-A bond is shortened by respectively 10, 17, and 28% with respect to the average, the 2nd-shortest O1-A bond by respectively 4, 11, and 23%, and the shortest O2-A bond by respectively 12, 16, and 22%. The oxygen coordination of the A-ion is reduced from 12 to 4, with two of the near oxygens being in the horizontal, flat face of the distorted A-cube, and the two others in *one* of the vertical, buckled faces. The A-B-A diagonal (orange bar) lying in the plane of the short, red arrows is shortened by respectively 3, 7, and 9% of the average. The unit shown is the front bottom left one (subcell 1) seen in *e.g.* figure 2.

the unit is the one in the front bottom left corner.

Finally, the orange bar in figure 7 indicates that one of the four A-B-A diagonals, [111], is shortened by respectively 3, 7 (5), and 9% of the average A-B-A distance in $CaVO_3$, $LaTiO_3$, and $YTiO_3$. The two A ions closest to B are those which bond weakest to the oxygen octahedron (red arrows in the figure). The corresponding distortion of the A cube is clearly visible in figure 2, and is presumably caused by the hard-core repulsion from the three nearest oxygens (the blue arrows in figure 7). Corresponding to this shortening of the [111] diagonal in subcell 1, is a stretching of the $[11\bar{1}]$ diagonal by nearly the same amount. In $YTiO_3$, the tilt of the oxygen octahedron around the b axis, *i.e.* towards the two Y atoms along $[1\bar{1}1]$, is particularly strong (20°, see figure 2) and the corresponding A-B-A distance is shortened by 5%. None of the other three materials have such a second, short diagonal. In the distorted structure, each A ion (all equivalent) has two nearest B neighbours (two short diagonals). From the point of view of the A ion in the lower right corner of figure 7, *i.e.* the one at $\frac{1}{2}\frac{1}{2}\frac{-1}{2}$, these B neighbours are at 110 and $11\bar{1}$.

In the following we shall turn to our primary interest, the development of the *low*-energy electronic structure along the series of d^1 perovskites. We shall see that the minute A character left behind in the B $3d\,(t_{2g})$ band after most of this character has been swept away by O-A covalency and the concomitant $GdFeO_3$-distortion, is decisive.

3. t_{2g} Wannier functions and their Hamiltonian

The physical properties of the d^1 perovskites are determined by the Wannier functions of the low-energy B $3d\,(t_{2g})$ bands, such as those shown in red in figure 3, and their on-site Coulomb repulsion. This, at least, is the working hypothesis of the present paper.

In figure 8 we show the truly minimal t_{2g} NMTO basis set for the case of $LaTiO_3$. In order to generate these orbitals, it is not necessary to choose local axes oriented after the oxygen octahedron: with x, y, and z referring to the *global* axes (see caption to figure 2) and the active channels specified simply as d_{xy}, d_{yz}, and d_{xz} on each of the four B sites, each orbital automatically adjusts to its environment. In the present case, this is mainly due to the downfolding of the on-site e_g character, as is explained in appendix A. The names and signs of the orbitals in subcells 2, 3, and 4 are thus the ones shown in the *middle* row of the figure. This is the natural choice when the structure is nearly cubic.

3.1. Cubic t_{2g} bands

In the *cubic* structure, the xy, yz, and xz Wannier orbitals are *equivalent.* Moreover, they are nearly *independent* because each orbital is even around its own plane and odd around the two other cubic planes. For that reason, the on-site and the 1st-nearest-neighbour couplings between different orbitals vanish. As regards the coupling to 2nd-nearest neighbours, the yz orbital, for instance, does couple to xy orbitals at the four 101 sites and to xz orbitals at the 110 sites, but the strength is negligible (6 meV).

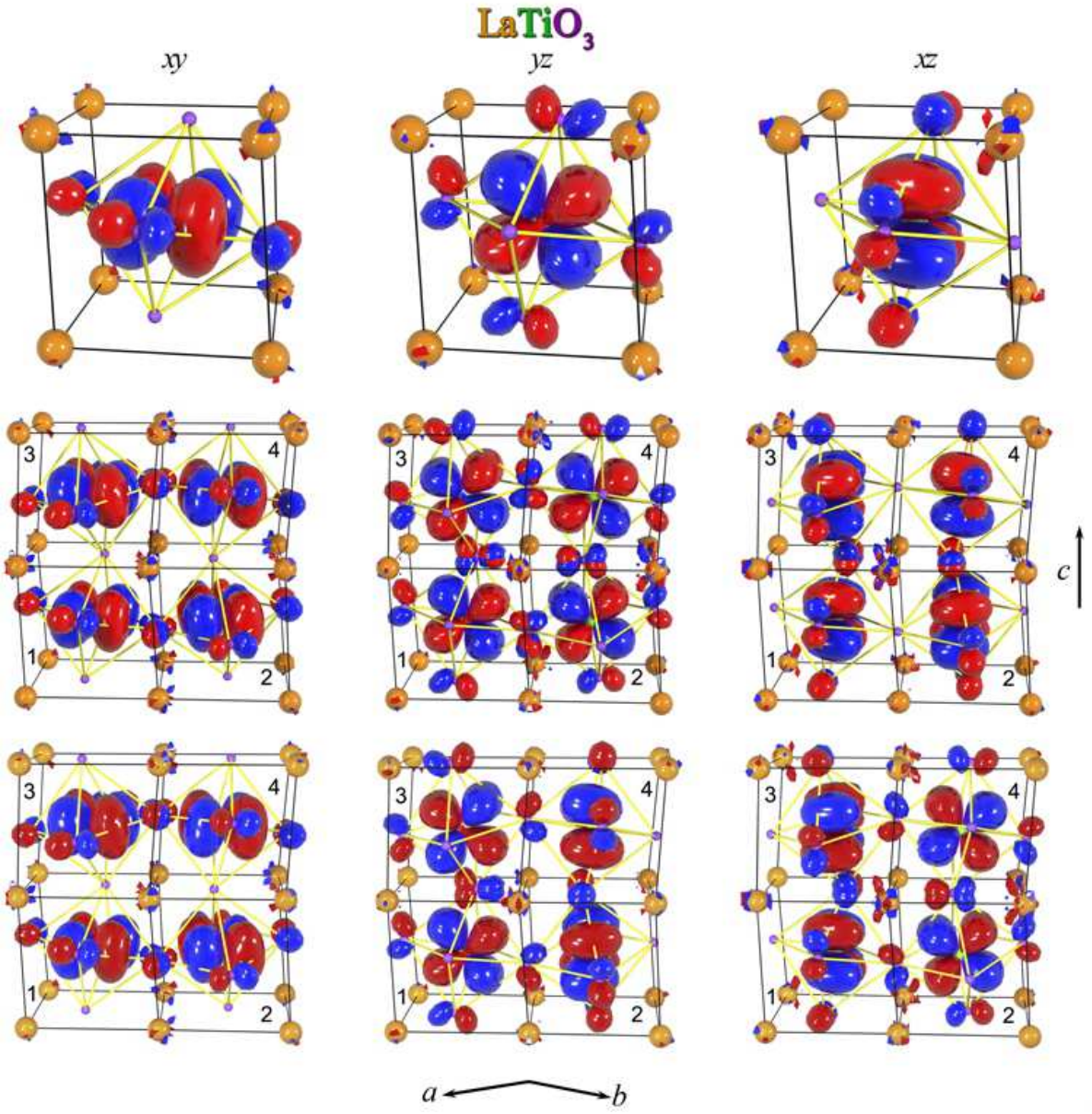

Figure 8. B t_{2g} xy, yz, and xz NMTOs for $LaTiO_3$. See also caption to figure 5. In the top row, the three different orbital shapes are in subcell 1. In the bottom row, the mirror and the glide-mirror have been used to place them also in subcells 2, 3, and 4 (see caption to figure 2). In the middle row, the orbitals have been grouped together in columns, and the signs have been chosen so as if the orbitals in subcells 2, 3, and 4 were mere translations of the ones in subcell 1. We shall use the middle-row convention for naming the xy, yz, and xz orbitals in subcells 2, 3, and 4. This convention is the natural one when the distortion from the cubic structure is small. If the structure were cubic, the three orbital shapes would be identical, and the sum over the 4 orbitals in each of the middle-row pictures would give a Bloch wave with $\mathbf{k}$=$\mathbf{0}$.

Before using the Wannier functions in figure 8, let us start simply by explaining the red t_{2g} band structure, $\varepsilon_{x_i x_j}(\mathbf{k})$, of *cubic* $SrVO_3$ in figure 3 in same way –but now

for each Bloch vector– as we discussed the gross features of the densities of states in figure 1; that is, in terms of a large basis set, the one giving rise to the black bands. In terms of Bloch waves, hybridization with oxygen states pushes t_{2g} band states *up* in energy and hybridization with A=Sr states pushes them *down.* In the cubic structure there is only one ABO_3 unit per primitive cell and the Brillouin zone (BZ) is the blue one shown in figure 9. We may use the middle row in figure 8 to illustrate the three degenerate Bloch waves: with $\mathbf{R}$ being the positions of the B atoms (cells), each cell should be decorated with a phase factor $\exp i\mathbf{k}\cdot\mathbf{R}$; *i.e.* $\exp ik_y$ in cell 2, $\exp ik_z$ in cell 3, $\exp i\left(k_y+k_z\right)$ in cell 4, etc.

At Γ ($\mathbf{k}$=$\mathbf{0}$), there is no coupling to oxygen p because each t_{2g} Bloch wave is odd around the OA planes perpendicular to the plane of the wave and the O $p\pi$ character is even. The direct $dd\pi$ coupling is seen to be antibonding and it therefore tends to increase the energy at Γ, but since Γ marks the bottom of the band, the direct coupling cannot be the dominant source of the band dispersion. Finally, we realize that at Γ all A characters vanish, except the same A $d\left(t_{2g}\right)$ character as that of the Bloch wave. Hence, $\varepsilon_{x_ix_j}\left(\mathbf{0}\right)$ is pushed down by interaction with A $d_{x_ix_j}$.

Going now from Γ to X 00π in figure 3, $\exp i\mathbf{k}\cdot\mathbf{R}$ changes sign on sites 3 and 4, whereby the yz and xz waves become even around the horizontal AO mirror plane and can couple $pd\pi$ antibonding along the z direction. This raises their band energy by $4t_{pd\pi}^2/\left(\varepsilon-\epsilon_p\right)\sim 2$ eV, minus the direct $dd\pi$ contribution, and plus the lost contribution from the bonding interaction with respectively A d_{yz} and A d_{xz}, which is now forbidden and is not substituted by any other coupling to A s or d. The xy wave becomes odd around the horizontal AO mirror plane, whereby its energy increases by merely a few tenths of an eV, due to direct $dd\delta$ hopping counteracted by the increased bonding interaction arising from the A d_{xy} character being substituted by A d_{xz} and A d_{yz}.

Proceeding then from X 00π to M $\pi0\pi$ in figure 3, the sign on sites 3 and 4 remains opposite to that on sites 1 and 2, but the sign alternates on the sheets which are perpendicular to x and not shown in figure 8. The energy of the yz band decreases by some tenths of an eV because the bonding interaction with A d_{xy} is now allowed, but this is counteracted by $dd\delta$. The energy of the xz band increases by less than 0.5 eV as the result of a further increase by $4t_{pd\pi}^2/\left(\varepsilon-\epsilon_p\right)$, and of reductions due to oxygen pp hopping, $dd\pi$ hopping, and coupling to A s. The energy of the xy band finally goes up by essentially $4t_{pd\pi}^2/\left(\varepsilon-\epsilon_p\right)$ and becomes degenerate with the yz band.

At R $\pi\pi\pi$ the sign on all 6 nearest B neighbours is reversed from that of the middle row in figure 8, and the energy of the three degenerate bands is slightly higher than that of the xz band at M $\pi0\pi$. This is because of direct $dd\delta$ hopping and because the coupling to A s is lost. Going finally from R back to Γ, the three bands stay degenerate.

If we neglect the very weak inter-orbital coupling (6 meV in $SrVO_3$), the dispersion of a cubic t_{2g} band can be written as a Fourier series:

$$\varepsilon_m\left(\mathbf{k}\right)=H_{m,m}^{LDA}\left(\mathbf{k}\right)=t_{m,m}^{000}+\sum_{xyz\neq\bar{x}\bar{y}\bar{z}}2t_{m,m}^{xyz}\,\cos\left(xk_x+yk_y+zk_z\right), \qquad (1)$$

where x, y, and z run over all integers and where we have used the inversion symmetry of

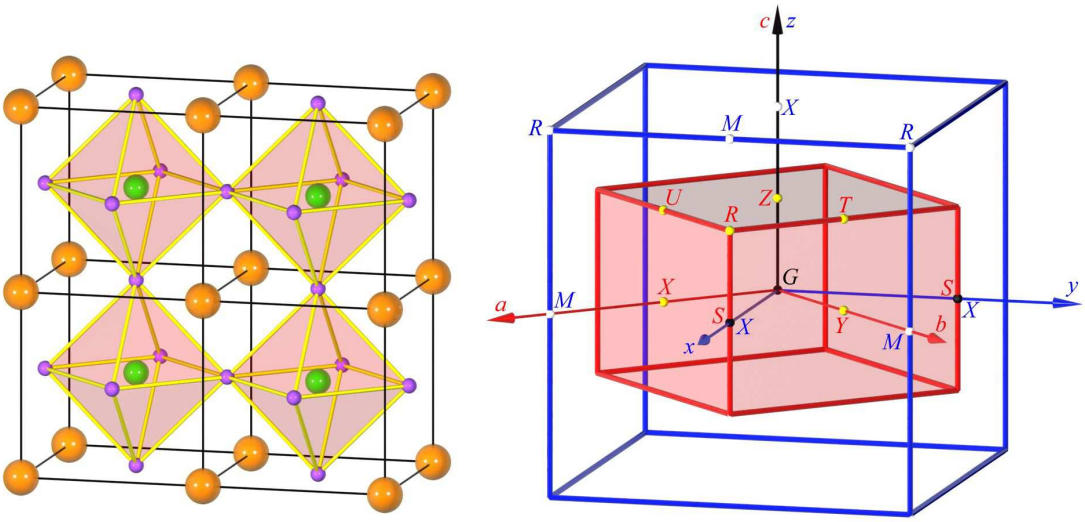

Figure 9. Primitive cells of the monoclinic, nearly cubic and the quadrupled orthorhombic *Pbnm* structures (left), as well as their respective (blue and red) Brillouin zones (right). See also figure 2. Taking the pseudo-cubic lattice constant, $|\hat{\mathbf{x}}|$, as unity, the primitive reciprocal-lattice translations in the monoclinic structure are given by: $2\pi\mathbf{G}_x = \{[1+(\alpha+\beta)/2]\,\hat{\mathbf{x}} + [(\alpha-\beta)/2]\,\hat{\mathbf{y}}\}/(1+\alpha+\beta+\alpha\beta)$, $2\pi\mathbf{G}_y = \{[(\alpha-\beta)/2]\,\hat{\mathbf{x}} + [1+(\alpha+\beta)/2]\,\hat{\mathbf{y}}\}/(1+\alpha+\beta+\alpha\beta)$, and $2\pi\mathbf{G}_z = \hat{\mathbf{z}}/(1+\gamma)$. With $\mathbf{k} \equiv k_x\mathbf{G}_x + k_y\mathbf{G}_y + k_z\mathbf{G}_z$, the $k_xk_yk_z$ coordinates of the points marked in the blue, primitive monoclinic BZ are: G(Γ) 000, X π00, M $\pi\pi$0, R $\pi\pi\pi$, and the equivalent ones. The high-symmetry points of the red, folded-in orthorhombic BZ are: G_o (Γ_o) 000, Z_o $00\frac{\pi}{2}$, X_o $\frac{-\pi}{2}\frac{\pi}{2}0$, Y_o $\frac{\pi}{2}\frac{\pi}{2}0$, S_o π00, R_o $\pi 0\frac{\pi}{2}$, U_o $\frac{-\pi}{2}\frac{\pi}{2}\frac{\pi}{2}$, T_o $\frac{\pi}{2}\frac{\pi}{2}\frac{\pi}{2}$, and the equivalent ones. The points explicitly listed are those used in figure 17.

the orbitals and the lattice to combine the complex exponentials into cosines. In table 1 we give the energy of the three degenerate t_{2g} Wannier functions, $t^{000}_{xy,xy} = t^{000}_{yz,yz} = t^{000}_{xz,xz} \equiv \epsilon_{t_{2g}} - \varepsilon_F$, and their transfer- or hopping integrals, such as the most important 1st-nearest-neighbour integrals, $t^{100}_{xy,xy} = t^{001}_{yz,yz} = t^{001}_{xz,xz} \equiv t_\pi$ and $t^{001}_{xy,xy} = t^{100}_{yz,yz} = t^{010}_{xz,xz} \equiv t_\delta$, and the most important 2nd-nearest-neighbour integral, $t^{110}_{xy,xy} = t^{011}_{yz,yz} = t^{101}_{xz,xz} \equiv t'_\sigma$. The description in terms of Wannier functions will be considered in detail in the following subsection, where we shall also explain why all the above-mentioned, most important hopping integrals are negative. Neglecting all other hopping integrals, the Fourier series (1) simplifies to:

$$\varepsilon_{x_ix_j}(\mathbf{k}) = \epsilon_{t_{2g}} + 2t_\pi(c_i + c_j) + 2t_\delta c_k + 4t'_\sigma c_i c_j, \tag{2}$$

where $x_i = x$, y, or z, and i, j, and k are all different. Moreover, $c_i \equiv \cos k_{x_i}$. In this approximation the Γ–R bandwidth is $-8t_\pi - 4t_\delta$, which for $SrVO_3$ is 2.4 eV. Hops to farther neighbours give another 0.5 eV.

Had it not been for the direct and A-mediated *effective* $dd\delta$ couplings between t_{2g} Wannier functions expressed by t_δ, the dispersion in figure 3 would have been *two dimensional*, with the bottom at Γ, top at M, and saddle-points at X. The latter would

Table 1. $H^{LDA}_{t_{2g}}$ in meV for cubic $SrVO_3$.

xyz	000	001	010	100	011	101	110	111	002	020	200
m', m											
yz, yz	625	−281	−281	−33	−96	9	9	−11	10	10	0

give rise to a logarithmic van Hove singularity in the density of states. The strong reminiscence of this 2D singularity for $SrVO_3$ is clearly seen at the bottom left-hand side of figure 1. However, as we go along the series –but stay in the cubic structure– this sharp peak is gradually washed out due to increase of the A-mediated effective $dd\delta$ coupling and, in the titanates, to A d bands overlapping the t_{2g} bands.

3.2. The (xy, yz, xz) set of Wannier orbitals in the presence of $GdFeO_3$-type distortion

Distorting now the structures to the *real* ones, the density-of-states profiles are seen to sharpen in figure 1. This is because the increased O-A covalency pushes the A d bands up above the t_{2g} band. But new structures arise, and these are caused by lifting the degeneracy between the xy, yz, and xz Bloch waves, by coupling between the waves, and by quadrupling the primitive cell. Let us now explain this –without getting into the details of the 4×3 orthorhombic bands– in terms of the (xy, yz, xz) set of Wannier functions for $LaTiO_3$ shown (before orthogonalization) in figure 8.

In the top row of this figure we see that the t_{2g} orbitals have π antibonding oxygen p character. This is the partner to the π bonding B t_{2g} character of the oxygen p orbitals in the cube faces seen in figures 5 and 6. Since those are the oxygen orbitals with which the A d orbitals interact strongly (σ interaction) and thereby cause the $GdFeO_3$-type distortion, they mix less with the B t_{2g} orbitals and the oxygen p character of the B t_{2g} orbitals in figure 8 is correspondingly weak. The oxygen character of the t_{2g} orbitals therefore decreases with increasing O-A covalency and the concomitant decrease of the shortest O-A distances (figure 7). Adding to this trend comes the reduction of oxygen character, $\propto t^2_{pd\pi}/\left(\epsilon_d - \epsilon_p\right)^2$, caused by the fact that the $3d$ level of the earlier transition-metal ion, Ti, is higher above the O $2p$ level than that of the later transition-metal ion, V. This increase of $\epsilon_d - \epsilon_p$ seen in figure 1 is partly compensated by an increase of $t_{pd\pi}$ caused by the expansion of the $3d$ orbital when going from V to Ti.

In addition to the oxygen $pd\pi$ antibonding character, the t_{2g} orbitals have some A character and, in the distorted titanates, some e_g character on neighbouring B sites where it bonds to the appropriate p lobe of a displaced oxygen. Such characters are barely seen in figure 8, but they are seen in figure 15 where a lower contour was chosen – albeit in subcell 2 and for a particular linear combination of t_{2g} orbitals.

The oxygen character is decisive for the *width* of the t_{2g} band, that is, for the overall

size of the matrix elements of the Hamiltonian between t_{2g} Wannier orbitals on different sites (hopping integrals). The A character is important for *lifting* the cubic symmetry of on- and off-site matrix elements, and the B e_g character induces on-site coupling between the orbitals. In order to demonstrate the specifics of this, we must first explain how the shapes of the Wannier orbitals are modified by the A *spd* and B e_g characters:

For *all three* t_{2g} orbitals in the top row of figure 8 (subcell 1), the red lobes attain some bonding *sp* and $d_{3z^2_{111}-1} = (d_{xy} + d_{yz} + d_{xz})/\sqrt{3}$ character on the *nearest* A neighbours, the ones at approximately $\frac{1}{2}\frac{1}{2}\frac{1}{2}$. The red lobes thereby stretch along the short A-B-A diagonal (orange bar in figure 7). This is not merely an effect of A-B covalency, but the oxygens set the stage as follows: the antibonding oxygen characters of the t_{2g} orbitals are deformed by bonding interaction with their nearest A neighbour (blue arrows in figure 7), and those A neighbours are thereby prevented from bonding to t_{2g}. As a result, the blue oxygen p lobes push the red t_{2g} lobes towards those two A ions which are *not* nearest neighbour to any oxygen, *i.e.* those along the [111] diagonal. The latter A ions are the ones free to bond with the red t_{2g} lobes, and they do this by contributing A *sp* $d_{3z^2_{111}-1}$ character. This stretching of the t_{2g} orbitals along the shortest A-B-A diagonal is less pronounced in $YTiO_3$ than in $LaTiO_3$, because in $YTiO_3$, O1 is unusually close (red arrow in figure 7) to the A ion at $\frac{1}{2}\frac{1}{2}\frac{1}{2}$ and thereby partly blocks the A-B covalency. We shall later see how this difference between the two titanates influences their physical properties.

The yz orbital is special in that its blue lobes attain bonding *sp* and d_{xy} character on the two 2nd-nearest A neighbours, the ones at $\frac{1}{2}\frac{-1}{2}\frac{1}{2}$ in subcell 1. This is because the yz orbital has no p character on those oxygens, $\frac{1}{2}00$, which have the $\frac{1}{2}\frac{-1}{2}\frac{1}{2}$ ions as their closest A neighbours, and therefore cannot prevent the blue yz lobes from hybridizing with them. At the same time, a blue yz lobe is pushed towards the ion at $\frac{1}{2}\frac{-1}{2}\frac{1}{2}$ by the red O2 p_z lobe tending to bond with *its* nearest A neighbour, the one at $\frac{1}{2}\frac{-1}{2}\frac{1}{2}$. The hybridization is with A d_{xy} because the tilt has moved the blue yz lobe towards the c direction, but the red O1 p_y lobe then repels the blue yz lobe, which finally ends up running parallel to the flat O1-A face (mirror plane). The strong displacement of O1 leaves space for the blue yz lobe to bend over and become d_{xy}-like at A $\frac{1}{2}\frac{-1}{2}\frac{1}{2}$. This effect is stronger in $YTiO_3$ than in $LaTiO_3$, where also the 2nd-shortest A-B distance is 5% shorter than the average, rather than merely 1%. As a consequence, there is more A d_{xy} character in $YTiO_3$ than in $LaTiO_3$. This difference between the two titanates will also turn out to be important for their physical properties.

The xy orbital is the one whose orientation is most influenced by the $GdFeO_3$-type distortion, simply because the axes of tilt and rotation are perpendicular to its lobe axes. The tilt moves the blue lobes towards the 2nd-nearest A ions at $\frac{1}{2}\frac{-1}{2}\frac{1}{2}$, where the xy orbital attains some bonding A *sp* d_{xy} character, but this is blocked by the attraction of the red O2 p_y lobe to its closest A neighbour, as was explained above. For small $GdFeO_3$-type distortions, *i.e.* in $CaVO_3$, this reshaping of the t_{2g} orbital by O-A covalency can be neglected, and the pure tilt of the xy orbital and its hybridization with A *sp* d_{xy} are the most important effects of the distortion.

Finally, we restate that an oxygen p lobe which points opposite to the direction of its displacement in the cube face, may attain bonding e_g character on the B neighbour. This enhances the p lobe and bends it outwards. This effect increases with the displacement of oxygen, *i.e.* with the degree of $GdFeO_3$ distortion.

3.3. Effective hopping integrals

In table 1 above, and in tables 2–5 we give the matrix elements of the LDA Hamiltonian (relatively to ε_F),

$$H^{LDA}_{\mathbf{0}m',\mathbf{R}m} \equiv \left\langle \chi^{\perp}_{\mathbf{0}\,t_{2g}\,m'} \left| \mathcal{H}^{LDA} - \varepsilon_F \right| \chi^{\perp}_{\mathbf{R}\,t_{2g}\,m} \right\rangle \equiv t^{xyz}_{m',m} \ ,$$

in a t_{2g} Wannier representation (A.3). Here, $\mathbf{R} = x\mathbf{R}_x + y\mathbf{R}_y + z\mathbf{R}_z$ is a B site (see caption to figure 2) and x, y, and z are integers. The matrix element between orbitals m' and m, both on site 000, is $t^{000}_{m',m}$, and the hopping integral from orbital m' on site 000 to orbital m on site xyz is $t^{xyz}_{m',m}$. Having the symmetry of d functions, these orbitals are *even* with respect to inversion in their own B site and, as a consequence,

$$t^{xyz}_{m',m} = t^{\bar{x}\bar{y}\bar{z}}_{m',m}. \tag{3}$$

In this set of tables, the cubic basis ($m = yz, xz, xy$) is used, with orbitals named as in the middle row of figure 8. The values of the matrix elements,

$$H^{LDA}_{\mathbf{R}'m',\mathbf{R}m} \equiv \left\langle \chi^{\perp}_{\mathbf{R}'\,t_{2g}\,m'} \left| \mathcal{H}^{LDA} - \varepsilon_F \right| \chi^{\perp}_{\mathbf{R}\,t_{2g}\,m} \right\rangle \equiv t^{\mathbf{R}',\mathbf{R}}_{m',m}$$

with $\mathbf{R}' \neq \mathbf{0}$, are given by the following rules, obtained by use of the mirror ($z \leftrightarrow -z$) and the glide-mirror ($x \leftrightarrow y$) :

$$\begin{array}{ll} t^{(0,0,1),(x,y,z+1)}_{m',m} = t^{xy\bar{z}}_{m'(z\to -z),m(z\to -z)} & t^{(0,1,1),(x,y+1,z+1)}_{m',m} = t^{yx\bar{z}}_{m'(x\leftrightarrow y,z\to -z),m(x\leftrightarrow y,\ z\to -z)} \\ t^{(0,0,0),(x,y,z)}_{m',m} \equiv t^{xyz}_{m',m} & t^{(0,1,0),(x,y+1,z)}_{m',m} = t^{yxz}_{m'(x\leftrightarrow y),\ m(x\leftrightarrow y)} \end{array} \tag{4}$$

Before discussing these results, we stress that our downfolding to t_{2g}Wannier functions and evaluation of the Hamiltonian matrix is numerically exact. That is, our Wannier functions span the Kohn-Sham t_{2g} eigenfunctions exactly. Specifically, *all* partial waves other than B t_{2g} are downfolded, and their dependence on energy over the range of the t_{2g} band is properly represented. This is explained in appendix A and is illustrated in figures 3 and 10. The downfolding procedure used in model calculations such as [25, 29] is different, and not exact in the above-mentioned sense. In model calculations, only orbitals such as O $2p$, and recently A $5d$, expected to be relevant are downfolded, and their hopping integrals are assumed to follow the Slater-Koster rules. The latter may be a serious approximation, because, *e.g.*, the O p orbitals have A and B s and p tails unless *those* orbitals are also being downfolded explicitly. Moreover, model calculations use Löwdin downfolding with $\varepsilon \equiv \epsilon_{t_{2g}}$ (see equation (A.5)). In the NMTO scheme, this corresponds to taking $N = 0$, that is, to using merely a single energy point. Once the Coulomb correlations are taken into account, not all the hopping integrals we tabulate may be relevant, of course, but the dominant ones are, and their values matter.

We now discuss our results and start by considering various contributions to a dominant t_{2g} hopping integral, namely the effective, 1st-nearest-neighbour $dd\pi$ hopping integral t_π. A particularly important example will turn out to be $t^{001}_{yz,yz}$. This is the matrix element of the LDA Hamiltonian between the yz Wannier orbital in subcell 1 and the similar orbital in subcell 3, defined as in the middle row of figure 8. Its value is seen to be *negative* (bonding), and to take the values $-281\,$meV in cubic $SrVO_3$, $-240\,$meV in $CaVO_3$, $-193\,$meV in $LaTiO_3$, and a mere $-65\,$meV in $YTiO_3$. This hopping integral between Wannier orbitals may be interpreted in terms of the energies of, and the hopping integrals between the simpler orbitals of a large basis –like the one giving rise to the black bands in figure 3 and like the ones discussed in for instance references [25, 29, 45]– containing O p, the B d and A s and A d orbitals, all assumed to be orthonormal and to have interactions between 1st-nearest neighbours only. If we perform Löwdin downfolding (A.5) of the Hamiltonian in the large basis and use the middle row of figure 8 to keep track of the geometry and the signs, we obtain the following kind of result:

$$\begin{aligned} t_\pi: \quad t^{001}_{yz,yz} \;&\sim\; t_{dd\pi} - \frac{t^2_{pd\pi}}{\varepsilon-\epsilon_p} - \frac{4t^2_{Byz,As}}{\varepsilon-\epsilon_{As}} + \frac{4t^2_{Byz,Ayz}}{\varepsilon-\epsilon_{Ad}} + \frac{4t^2_{Byz,Axz}}{\varepsilon-\epsilon_{Ad}} - \frac{4t^2_{Byz,Axy}}{\varepsilon-\epsilon_{Ad}} \\ &= t_{dd\pi} - \frac{t^2_{pd\pi}}{\varepsilon-\epsilon_p} + \frac{4t^2_{Byz,As}}{\epsilon_{As}-\varepsilon} - \frac{4t^2_{Byz,Ayz}}{\epsilon_{Ad}-\varepsilon} - \frac{4t^2_{Byz,Axz}}{\epsilon_{Ad}-\varepsilon} + \frac{4t^2_{Byz,Axy}}{\epsilon_{Ad}-\varepsilon}. \end{aligned} \tag{5}$$

In the second line all signs are *explicit* because the *direct* hopping integral $t_{dd\pi}$ is *positive* (anti-bonding), and $\epsilon_p < \varepsilon < \epsilon_{As} \sim \epsilon_{Ad}$ when ε is in the t_{2g} band. The dominant term is the second one, the $pd\pi$ hopping via oxygen. This term is *bonding* (negative) and is *weakened* by the direct $dd\pi$ term, as well as by hops via A orbitals which are *even* with respect to the mirror plane between the two yz orbitals. The oxygen-mediated $pd\pi$ hopping is *strengthened* by hops via A orbitals which are *odd* with respect to the mirror plane.

That the first two terms in equation (5) have opposite signs, and that the second term dominates, should warn against interpreting hopping integrals between Wannier orbitals as overlap integrals. Moreover, characters barely visible in figures like 8 and 1, can contribute significantly to hopping if their energy is high, because the contribution to a hopping integral by a character of magnitude $t^2_{BA}/\left(\epsilon_A-\varepsilon\right)^2$ is $t^2_{BA}/\left(\epsilon_A-\varepsilon\right)$, that is, $\epsilon_A-\varepsilon$ times larger.

Now, the contributions from the four nearest A neighbours to an A term in expression (5) are identical only if the structure is cubic. In this case, actually, the two last terms in equation (5) cancel. Moreover, only if the structure is cubic do hopping integrals like $t_{dd\pi}$ and $t_{pd\pi}$ have their full value. Otherwise, they are reduced due to misalignment.

In $SrVO_3$ the contribution from hops via A ions is small, as evidenced in figure 1 by the weak Sr d character in the V t_{2g} band. But in the titanates, the t_{2g} band has almost as much A d as O p character. This is not so evident from the appearance of a single t_{2g} orbital in figure 8, because for a B t_{2g} orbital, B:A=1:8 rather than 1:1, as in the formula unit, ABO_3. Similarly, for a B t_{2g} orbital, B:O=1:4 rather than 1:3. In the

Table 2. $H^{LDA}_{t_{2g}}$ in meV for $CaVO_3$ [43].

xyz	000	001	010	100	011	$01\bar{1}$	101	$10\bar{1}$	110	$1\bar{1}0$	111	$11\bar{1}$	$\bar{1}11$	$1\bar{1}1$
m', m														
yz, yz	620	−240	−223	−17	−91	−90	6	10	2	10	−8	−8	−3	−3
xz, xz	612	−249	−17	−223	10	6	−90	−91	3	3	−2	−2	−7	−7
xy, xy	542	−23	−231	−231	6	7	7	6	−98	−85	−2	−2	−3	−3
yz, xz	4	−21	45	45	6	22	22	6	8	−2	−1	0	0	0
xz, yz	4	−21	−33	−33	−20	−1	−1	−20	8	−2	0	−1	0	0
yz, xy	−17	−36	−17	−25	−2	13	8	−4	−17	5	−5	−4	−2	−5
xy, yz	−17	36	−34	33	11	−5	0	−11	−17	5	4	5	5	2
xz, xy	−4	25	33	−34	11	0	5	−11	15	−1	8	0	4	2
xy, xz	−4	−25	−25	−17	4	−8	−13	2	15	−1	0	−8	−2	−4

Table 3. $H^{LDA}_{t_{2g}}$ in meV for $LaTiO_3$ using the older data [44].

xyz	000	001	010	100	011	$01\bar{1}$	101	$10\bar{1}$	110	$1\bar{1}0$	111	$11\bar{1}$	$\bar{1}11$	$1\bar{1}1$
m', m														
yz, yz	474	−202	−195	−8	−57	−67	−8	18	4	−3	−9	−9	2	2
xz, xz	543	−221	−8	−195	18	−8	−67	−57	−10	14	−1	−1	−7	−7
xy, xy	525	−30	−197	−197	−3	13	13	−3	−60	−56	3	3	4	4
yz, xz	−21	−36	77	77	20	16	16	20	−2	8	−6	11	−10	−11
xz, yz	−21	−36	−38	−38	−24	−13	−13	−24	−2	8	11	−6	−11	−10
yz, xy	−78	−58	−27	−43	19	11	−3	4	−22	−3	0	−6	−21	4
xy, yz	−78	58	−49	72	−14	10	−12	−1	−22	−3	6	0	−4	21
xz, xy	−60	54	72	−49	1	12	−10	14	12	6	22	−6	11	0
xy, xz	−60	−54	−43	−27	−4	3	−11	−19	12	6	6	−22	0	−11

heavily distorted $YTiO_3$, the hopping integral $t_{Byz,Axy}$ to the 2nd-nearest Y, the one at position $\frac{1}{2}\frac{-1}{2}\frac{1}{2}$ in subcell 1, is large, and that is the main reason for the *anomalously small value of* $t^{001}_{yz,yz}$ *in* $YTiO_3$. The values of the five other t_π integrals, $t^{001}_{xz,xz}$, $t^{010}_{yz,yz} = t^{100}_{xz,xz}$, and $t^{100}_{xy} = t^{010}_{xy}$, are normal and approximately −170 meV in this material.

When estimating the value of $t^{010}_{yz,yz}$ it should be remembered that, with the notation of the middle row of figure 8, the yz orbital in subcell 2 has the shape of the xz orbital in subcell 1; this is the reason why $t^{010}_{yz,yz}$ does not have an abnormal A d_{xy} contribution, and also the reason why $t^{010}_{yz,yz} = t^{100}_{xz,xz}$.

Table 4. $H^{LDA}_{t_{2g}}$ in meV for $LaTiO_3$ [12].*

xyz	000	001	010	100	011	$01\bar{1}$	101	$10\bar{1}$	110	$1\bar{1}0$	111	$11\bar{1}$	$\bar{1}11$	$1\bar{1}1$
m', m														
yz, yz	445	−193	−185	1	−46	−49	−6	21	−1	−3	−6	−6	0	0
xz, xz	530	−208	1	−185	21	−6	−49	−46	−17	2	5	5	−1	−1
xy, xy	486	−22	−183	−183	2	8	8	2	−47	−46	5	5	0	0
yz, xz	−42	−42	75	75	21	20	20	21	−2	7	−2	7	−6	−7
xz, yz	−42	−42	−43	−43	−21	−4	−4	−21	−2	7	7	−2	−7	−6
yz, xy	−89	−59	−34	−33	17	11	−2	1	−23	−2	−2	−8	−12	2
xy, yz	−89	59	−54	73	−14	10	−13	−5	−23	−2	8	2	−2	12
xz, xy	−42	52	73	−54	5	13	−10	14	9	11	19	−3	11	0
xy, xz	−42	−52	−33	−34	−1	2	−11	−17	9	11	3	−19	0	−11

* We used their room-temperature data. For calculation of exchange constants, we also used the 8 K data for $LaTiO_3$. The result is shown in table 7.

Table 5. $H^{LDA}_{t_{2g}}$ in meV for $YTiO_3$ [20].

xyz	000	001	010	100	011	$01\bar{1}$	101	$10\bar{1}$	110	$1\bar{1}0$	111	$11\bar{1}$	$\bar{1}11$	$1\bar{1}1$
m', m														
yz, yz	375	−65	−184	28	−34	−26	−7	18	14	14	−3	−3	−13	−13
xz, xz	605	−178	28	−184	18	−7	−26	−34	−5	−39	8	8	11	11
xy, xy	417	−8	−162	−162	9	−1	−1	9	−50	8	14	14	0	0
yz, xz	43	−63	70	70	11	34	34	11	19	13	−2	1	2	−9
xz, yz	43	−63	−41	−41	−19	1	1	−19	19	13	1	−2	−9	2
yz, xy	−103	−64	−54	−22	15	0	−7	2	−18	10	9	−10	15	1
xy, yz	−103	64	−64	65	−13	7	−23	−12	−18	10	10	−9	−1	−15
xz, xy	−17	83	65	−64	12	23	−7	13	16	16	24	−10	9	4
xy, xz	−17	−83	−22	−54	−2	7	0	−15	16	16	10	−24	−4	−9

The *average* of the t_π integrals in the tables decreases by a surprisingly constant ratio of 22% for every step we proceed along the series $SrVO_3$–$CaVO_3$–$LaTiO_3$–$YTiO_3$. This holds for the recent $LaTiO_3$ data [12], while the older data [44] yield a 16% drop from $CaVO_3$ and a 29% drop to $YTiO_3$.

When deriving expression (5) from equation (A.5) in configuration-space representation we have used low-order perturbation theory and have not properly inverted $\langle P\,|\varepsilon - \mathcal{H}|\,P\rangle$. This means that the reduction of oxygen character in the B t_{2g} Wannier

orbitals due to O-A covalency, and also the direct oxygen *pp* hopping, are not included in expression (5). But effectively, they both reduce the magnitude of all terms, except the first. Moreover, higher-order hopping processes such as B-O-A-B and B-O-A-O-B are neglected. Finally, the enhancement and outward bending of a *p* lobe on a displaced oxygen due to acquisition of bonding e_g character on the B neighbour is also neglected, but it effectively increases $t_{pd\pi}$ towards that B neighbour.

The second largest intra-orbital hopping integral is the effective 2nd-nearest-neighbour $dd\sigma$ integral, t'_σ. Like t_π in (5), it is *bonding* (negative), but smaller because the distance is longer and because there is no oxygen-mediated hopping, except in case of the heavily distorted $YTiO_3$. The typical integrals $t^{110}_{xy,xy}$ and $t^{1\bar{1}0}_{xy,xy}$ are both −96 meV in cubic $SrVO_3$, −98 and −85 meV in $CaVO_3$, −47 and −46 meV in $LaTiO_3$, and −50 and +8 meV in $YTiO_3$. From the middle left part of figure 8, we gather that the integral $t^{110}_{xy,xy}$ $\left(t^{1\bar{1}0}_{xy,xy}\right)$ from subcell 1 to the same subcell translated by **b** (**a**) has contributions from direct $dd\sigma$ like hopping –which is now bonding and therefore strengthening,– from A mediated hopping, and from $dp\pi$-*pp*-$pd\pi$ hops. For the two former, we get:

$$t'_\sigma: \quad t^{110}_{xy,xy}\left(t^{1\bar{1}0}_{xy,xy}\right) \sim t_{dd\sigma} + \frac{2t^2_{Bxy,As}}{\varepsilon-\epsilon_{As}} - \frac{2t^2_{Bxy,Ayz}}{\varepsilon-\epsilon_{Ad}} - \frac{2t^2_{Bxy,Axz}}{\varepsilon-\epsilon_{Ad}} + \frac{2t^2_{Bxy,Axy}}{\varepsilon-\epsilon_{Ad}}$$
$$= -|t_{dd\sigma}| - \frac{2t^2_{Bxy,As}}{\epsilon_{As}-\varepsilon} + \frac{2t^2_{Bxy,Ayz}}{\epsilon_{Ad}-\varepsilon} + \frac{2t^2_{Bxy,Axz}}{\epsilon_{Ad}-\varepsilon} - \frac{2t^2_{Bxy,Axy}}{\epsilon_{Ad}-\varepsilon}. \qquad (6)$$

For $t^{110}_{xy,xy}$, the two important A ions are $\frac{1}{2}\frac{1}{2}\frac{\pm1}{2}$ when seen from subcell 1, and $\frac{-1}{2}\frac{-1}{2}\frac{\pm1}{2}$ when seen from **b**. For $t^{1\bar{1}0}_{xy,xy}$, the two important A-ions are $\frac{1}{2}\frac{-1}{2}\frac{\pm1}{2}$ and $\frac{-1}{2}\frac{1}{2}\frac{\pm1}{2}$ as seen from respectively the origin and **a**. Keeping in mind the A characters of the *xy* orbital, we realize that although the intermediate A ions are different in cases **b** and **a**, strong A d_{xy} or $d_{yx/xz}$ character does not exist on the *same* A ion; hence, A *d* mediated coupling is weak in all cases. The two first terms in expression (6) seem to dominate, except in $YTiO_3$ where the rotation of the *xy* orbital and the deformation of its *d* and *p* lobes are so strong that there is hopping, t_{pd}, from the red p_y lobe on O2 to the blue *xy* lobe translated by **a**. This gives a *positive* term, $t_{pd\pi}t_{pd}/(\varepsilon-\epsilon_p)$, which diminishes $t^{1\bar{1}0}_{xy,xy}$. Due to the different deformation of the *xy* lobe, no such term exists for $t^{110}_{xy,xy}$.

The effective 1st-nearest-neighbour $dd\delta$-hopping, t_δ, *e.g.* $t^{100}_{yz,yz}$, is an order of magnitude smaller than t_π. It consists of the direct term $-|t_{dd\delta}|$, plus A mediated contributions. It is negative for $SrVO_3$, changes sign near $LaTiO_3$, and is positive for $YTiO_3$.

If the semi-quantitative expressions (5) and (6) for the effective hopping integrals are inserted in equation (1) for the dispersion of a cubic t_{2g} band, the results of the discussion at the beginning of this section will of course be reproduced.

We may define the root-mean-square value, t_{rms}, of the hopping integrals by $\sum t^2 \equiv 12\,(t_{rms})^2$, where the sum runs over all neighbours and all three orbitals, and where 12 is the number of orbitals times the number of strong (t_π) hopping integrals in the cubic structure. These rms values are listed in table 6 and are seen to decrease with 19% from $SrVO_3$ to $CaVO_3$, with 15% from $CaVO_3$ to $LaTiO_3$ (using the recent data [12]), and by 11% from $LaTiO_3$ to $YTiO_3$. Even though the hopping integrals of

type t_δ and t'_σ, which decrease rapidly through the series, are included in the t^2 sum, the 19–15–11% decrease of t_{rms} is significantly smaller than the 22–22–22% decrease of the average t_π. The reason is that the hopping *between* orbitals increases; without including inter-orbital hopping in the t^2-sum, t_{rms} would be 11% smaller in $LaTiO_3$ ([12]) and 19% smaller in $YTiO_3$.

Table 6. Rms values of the hopping integrals in meV

	$SrVO_3$[42]	$CaVO_3$[43]	$LaTiO_3$[44]	$LaTiO_3$[12]	$YTiO_3$[20]
t_{rms}	298	250	228	217	196

3.4. Effective on-site matrix elements

The Hamiltonian matrix elements most influenced by the lowering of the symmetry in the distorted perovskites are not the hopping integrals, but the *on-site* elements. The change of a hopping integral, however, usually perturbs the LDA bandstructure more than the same change of an on-site element, because the perturbation via the former is multiplied by the number of neighbours reached by that kind of hop. On the other hand, Coulomb correlations will effectively enhance the on-site elements and reduce the hopping integrals.

As seen in table 2 for $CaVO_3$, the energy of the xy orbital is 75 meV below that of the nearly degenerate yx and xz orbitals. One reason is that, for weak $GdFeO_3$-distortion, the xy orbital is the one whose orientation is most optimized with respect to the A anions, specifically the two along $[1\bar{1}1]$. The *electrostatic field* from these positive ions lowers the energy of orbitals pointing towards them. And so does the *ligand field* caused by hybridization with A orbitals, because for a *diagonal* matrix element, all interactions with characters of higher energy are bonding and push the energy of the Wannier orbital down. Conversely, all interactions with characters of lower energy are antibonding and push the energy up. As mentioned in connection with equation (5), $\epsilon_A > \varepsilon > \epsilon_p$. An additional reason for the energy of the xy orbital being the lowest is, therefore, that it has the least antibonding oxygen character. This comes about because the xy orbital interacts with four O2 ions, while each of the yz and xz orbitals interact with two O1 ions and two O2 ions. In addition, since Ca bonds more to O2 than to O1 (the distance is 2% shorter), less O2 character is left for the V xy orbital. This is a pure ligand-field effect, since from oxygen there is no electrostatic effect due to the lack of JT distortion in $CaVO_3$.

In the *titanates*, the energy of the yz orbital at sites 000 and 001 is ∼40 meV below that of the xy orbital. This is so because the orientation of the yz orbital towards the 1st- and 2nd-nearest A ions, those along the [111] and $[1\bar{1}1]$ diagonals, respectively,

Table 7. $H^{LDA}_{t_{2g}}$ in meV for $LaTiO_3$.

	$LaTiO_3$ at 8K [12]				$YTiO_3$ without JT				$YTiO_3$ at 15.9 GPa [9]			
xyz	000	001	010	100	000	001	010	100	000	001	010	100
m', m												
yz, yz	465	−195	−185	3	420	−68	−168	21	471	−41	−211	41
xz, xz	540	−208	3	−185	540	−148	21	−168	638	−184	41	−211
xy, xy	500	−21	−185	−185	457	−7	−207	−207	566	−10	−167	−167
yz, xz	−52	−45	76	76	36	−89	53	53	94	−79	73	73
xz, yz	−52	−45	−40	−40	36	−89	5	5	94	−79	−35	−35
yz, xy	−93	−61	−36	−32	−96	−66	−40	−57	−129	−82	−61	−13
xy, yz	−93	61	−56	73	−96	66	−46	95	−129	82	−75	58
xz, xy	−51	50	73	−56	−50	82	95	−46	−23	91	58	−75
xy, xz	−51	−50	−32	−36	−50	−82	−57	−40	−23	−91	−13	−61

exploits both the electrostatic and the ligand fields. An additional ligand-field effect is that, in the titanates the bonding of the A ion to O1 is stronger than to O2. Therefore, less antibonding O1 character is available for the Ti yz and xz Wannier functions. This can actually be seen in the top row of figure 8. Finally, the B neighbour e_g character which binds to the red back lobe of the O1 p_y orbital –the one which is displaced most along its own direction– also contributes to lower the energy of the yz Wannier orbital. The orbital with the highest energy at sites 000 and 001 is xz. In $LaTiO_3$, its energy is 85 meV above that of the yz orbital, and in $YTiO_3$, it is as much as 230 meV above. The main reason is that the xz orbital is the one of the three which is least favourably oriented with respect to the A ions, particularly in $YTiO_3$. In addition, the xz orbital has little B e_g character because its oxygen p lobes are not directed towards the face centres. A final reason why, particularly in $YTiO_3$, the energy of the xz orbital is very far above that of the yz orbital is the JT distortion: the distance to Ti 000 of the oxygens along z and x is 3% shorter than the distance along y, and the $pd\pi$ character of the t_{2g} functions is antibonding at the same time as the electrostatic field from the oxygen ions repel the near t_{2g} lobes.

There is a strong on-site coupling *between* the two *lowest* orbitals, xy and yz, in the titanates. It is −89 meV in $LaTiO_3$ and −103 meV in $YTiO_3$. This is due to the deformations of the xy and yz orbitals towards the 1st and 2nd-nearest A ions, those along [111] and $[1\bar{1}1]$. With the signs chosen for the two orbitals, the lobes have the same sign when they point towards a near A ion, and the opposite sign when they point towards a far A ion. For this reason, both electrostatics and hybridization with all A characters enforce each other to make this on-site inter-orbital interaction strong and negative.

In all cases considered, the electrostatic and ligand-field effects work in the same direction. In the following, we shall therefore refer to anisotropy of the on-site Hamiltonian matrix for the t_{2g} Wannier functions as a *crystal-field effect,* regardless of whether its origin is more electrostatic or covalent.

3.5. Influence of the Jahn-Teller distortion in $YTiO_3$

Although it is now generally recognized that the $GdFeO_3$-type distortion sets up a surprisingly large crystal field in the titanates, it is not agreed upon to what extent the JT distortion is important for the physical properties of $YTiO_3$ [21, 24, 29]. In table 7, we have included $H^{LDA}_{t_{2g}}$ calculated for a hypothetical structure of $YTiO_3$ in which the octahedra are perfect, i.e., they lack the 3% JT-elongation of the Ti-O2 bonds in the $y(x)$ direction in subcells 1 and 3 (2 and 4), and the orthorhombic lattice constants are as in the real structure [20]. As expected, the energy of the xz orbital at site 000 is lowered, but remains 120 meV above that of the yz orbital at the same site. But the on-site *couplings* have not decreased, and the coupling between the xz and xy orbitals has even increased. Undoing the JT-distortion also influences the hopping integrals, but that does not make them more cubic: t_π decreases between xz orbitals and increases between xy orbitals. With other plausible hypothetical structures without JT distortion, we obtained similar results.

Recent high-pressure measurements [9] have shown that the 3% JT distortion essentially disappears in the pressure region between 9 and 14 GPa. At the same time, the Y ions move even further away from their cubic positions. At 16 GPa, the Ti-O2 distances in the x and y directions have become nearly equal, with the Ti-O1 distance being just 1% smaller. Moreover the $GdFeO_3$-type tilt has increased from $\sim$20 to 21°, while the rotation is unchanged. The on-site Hamiltonian and nearest-neighbour hopping integrals calculated for this structure are included in table 7. We see that the ordering of the orbital energies is the *same* as for the JT distorted and undistorted structures at normal pressure, and that the energy of the xz orbital is "merely" 167 meV above that of the yz orbital, while that of the xy orbital is 95 meV above. These results are similar to the ones obtained for the hypothetical 0 GPa structure without JT distortion, and so is the result that the on-site coupling between the yz and xy orbitals increases upon removal of the JT distortion and readjustment of the Y positions.

In conclusion, the JT distortion influences the crystal field in $YTiO_3$, but is not its source. We shall return to this subject at the end of section 3.6, as well as in sections 3.7, 5.4, and 6.

3.6. Influence of $GdFeO_3$-type and JT distortions on the t_{2g} bandstructures

In the preceding subsections, we have clarified how the on-site and hopping matrix elements of the LDA Hamiltonian develop along the series. Now we need to understand how the $GdFeO_3$-type distortion perturbs the spatial coherence of the simple, cubic Bloch waves.

Table 8. t_{2g} edge-to-edge $\left(W_{t_{2g}}\right)$ and rms (W) bandwidths in eV.

	$SrVO_3$[42]	$CaVO_3$[43]	$LaTiO_3$[44]	$LaTiO_3$[12]	$YTiO_3$[20]
$W_{t_{2g}}$	2.85	2.45	2.09	1.92	2.05
W	2.85	2.39	2.18	2.08	1.87

The LDA bandstructures in the region of the t_{2g} bands are shown in figure 10 for all four materials. Like in figure 3, the red bands, $\varepsilon_i(\mathbf{k})$, are obtained from the t_{2g} Wannier functions, *e.g.* by forming Bloch sums (see equation (A.6)) of the Wannier orbitals and diagonalizing the Bloch transformed Hamiltonian,

$$H^{LDA}_{\mathbf{R}'m',\mathbf{R}m}(\mathbf{k}) \equiv \sum_{\mathbf{T}} t^{\mathbf{R}',\mathbf{R}+\mathbf{T}}_{m',m}\, e^{i\mathbf{k}\cdot(\mathbf{T}+\mathbf{R}-\mathbf{R}')}. \tag{7}$$

We thus obtain the eigenvalues, $\varepsilon_i(\mathbf{k})$, and eigenvectors, $\mathbf{u}_i(\mathbf{k})$. Since the orthorhombic structure has four (equivalent) subcells per translational cell, there are 4×3=12 orthorhombic t_{2g} bands. In equation (7), $\mathbf{T}$ are the orthorhombic translations, and $\mathbf{R}$ and $\mathbf{R}'$ run over the four B sites, 000, 010, 001, and 011. The structure is specified in the caption to figure 2. The Hamiltonian is a periodic function of $\mathbf{k}$ in the lattice reciprocal to the orthorhombic lattice. The corresponding BZ is shown in red in figure 9, whose caption specifies the reciprocal-space structure. The 12 bands are doubly degenerate on the faces of the orthorhombic BZ due to the presence of the mirror and the glide mirror in the space group.

As we proceed along the series, the t_{2g} edge-to-edge *bandwidth*, $W_{t_{2g}}$, is clearly seen to decrease. It is tabulated in the top row of table 8. In the second row, we give an rms bandwidth, W, which we define to be proportional to t_{rms} (table 6) with the prefactor chosen such that $W = W_{t_{2g}}$ in case of cubic $SrVO_3$, i.e.: $W \equiv \left(W_{t_{2g}}/t_{rms}\right)_{SrVO_3} \times t_{rms}$. We see that the decrease of the edge-to-edge bandwidth does *not* follow the trend of t_{rms}. So, clearly, band *shapes* change along the series.

In view of the extreme simplicity of the cubic bandstructure of $SrVO_3$ (subsection 3.1), the orthorhombic ones are bewilderingly complicated. They do not immediately tell us what the progressing $GdFeO_3$-type distortion actually does. Simple theories have assumed that all hopping integrals scale uniformly with the bandwidth, *i.e.*, that the bandstructures of all four materials look the same; clearly, they do not.

The next simplest case is that of a pure, cooperative JT distortion, *e.g.* the one in which the energy of the yz orbital on site 000 is Δ lower than that of the xz orbital on the same site. The glide mirror, which exchanges yz and xz on the nearest neighbours in the x and y directions, will then make a yz/xz orbital feel a spatially alternating potential, $\mp\frac{1}{2}\Delta \exp i\pi(x+y) = \mp\frac{1}{2}\Delta \exp[i(\pi,\pi,0)\cdot\mathbf{R}]$. This makes the cubic $\varepsilon_{yz}(\mathbf{k})$ and $\varepsilon_{yz}(\mathbf{k}-\pi\pi 0)$ bands split by Δ at the surface in $\mathbf{k}$ space where they would have crossed had there been no JT distortion. The same holds for the xz band. In this

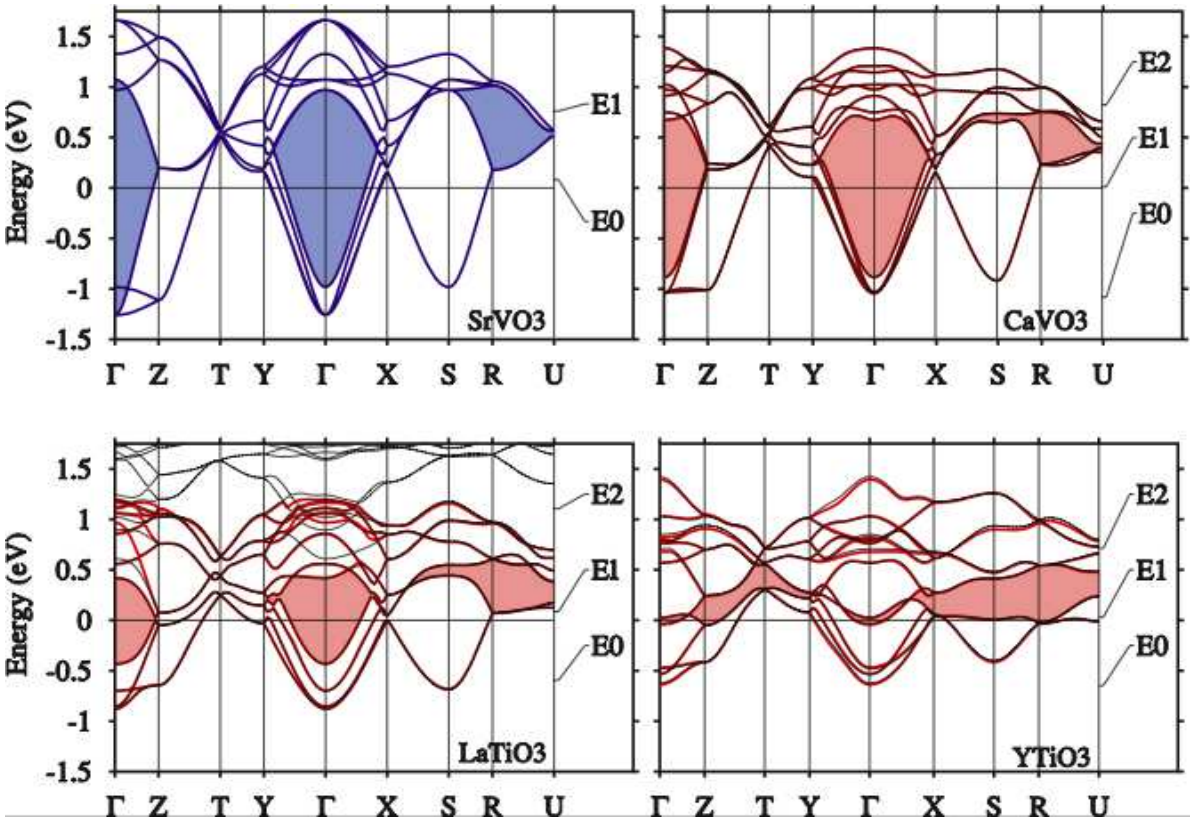

Figure 10. Low-energy LDA bandstructures of $SrVO_3$, $CaVO_3$, $LaTiO_3$, and $YTiO_3$. The cubic bands for $SrVO_3$ (figure 3) have been folded into the orthorhombic BZ (figure 9). The black bands were obtained with a large NMTO basis, while the coloured ones were obtained with the truly-minimal B $d\,(t_{2g})$ basis. The two are indistinguishable, except for $LaTiO_3$ where the bottom of the La $5d$-band overlaps the top of the Ti t_{2g}-band because the older structural data [44] was used here. With the recent, slightly more distorted structure [12], O-A covalency removes this overlap as discussed in section 2 and figure 1, and as shown in figures 4, 12, and 17. In order to emphasize the development of the bandstructure along the series, the gap between the lower 1/3 and the upper 2/3 of the bands has been shaded.

case, the xy band is unaffected, and there is no need for folding the bands along the z direction, *i.e.* by the reciprocal lattice vectors 00π and $\pi\pi\pi$.

For the t^1_{2g} materials, however, the dominant crystal-field splitting, $\Delta = t^{000}_{yz,yz} - t^{000}_{xz,xz}$, is at most a tenth of the bandwidth, and yet, individual bands are seen to shift by up to half the bandwidth when we proceed along the series in figure 10. The following shifts (splittings) are large and important, because they move bands which are near the Fermi level: the 4th band at Γ_o moves up, and in $YTiO_3$ it almost empties. At the same time, the 5th band at Γ_o and the degenerate 3rd and 4th bands at S_o move down, so that in the Stoner model for ferromagnetism in $YTiO_3$ they become occupied (see also figure 18). This downward shift of the 3rd and 4th bands near S_o is the cause for the gradual development of a *pseudo-gap* between the lower 1/3 and the upper 2/3 of the t_{2g} band. In comparison, the Δ-gapping of the yz and xz bands along the lines Y_oT_o

and $\mathrm{X}_o\mathrm{U}_o$ $\frac{\pm\pi}{2}\frac{\pi}{2}k_z$ is less spectacular.

Coulomb correlations will of course change all of this, but in a fairly simple way, at least in the DMFT as we shall see in section 5.3: the one-electron excitations can be described as the LDA Hamiltonian plus a self-energy, which in the single-site DMFT is simply an energy-dependent, complex on-site matrix, $\Sigma_{mm'}(\omega)$. It is therefore important to understand the LDA bandstructure and, even better, to have an analytical model of it, to which a given $\Sigma_{mm'}(\omega)$ can be added or even determined, say, by a model DMFT calculation. Such an analytical model should for instance be useful for understanding why recent de Haas–van Alphen (dHvA) measurements for $CaVO_3$ gave a Fermi surface more cubic than the orthorhombic one obtained from the LDA [46].

An analytical bandstructure model may be obtained by transforming from the mixed $(\mathbf{k},\mathbf{R})$ representation (7), where $\mathbf{R}$ are the four sites in the orthorhombic cell, to a pure wave-vector $\mathbf{k}-\mathbf{Q}$ representation, where $\mathbf{Q}$ are the four smallest, inequivalent vectors,

$$\mathbf{Q} = 000,\ \pi\pi 0,\ 00\pi,\ \text{and}\ \pi\pi\pi, \tag{8}$$

of the orthorhombic reciprocal lattice ($\mathbf{Q}\cdot\mathbf{T} = 2\pi\times$integer). In figure 9, these are the blue points Γ, M_{xy}, X_z, and R of high symmetry in the cubic (actually primitive monoclinic) BZ. The transformed Bloch-waves are:

$$\begin{aligned}\frac{1}{\sqrt{4}}\sum_{\mathbf{R}}^{4}|\mathbf{R},m,\mathbf{k}\rangle\, e^{-i\mathbf{Q}\cdot\mathbf{R}} &= \sum_{\mathbf{R}}^{4}\frac{1}{\sqrt{4L_o}}\sum_{\mathbf{T}}^{o}|\mathbf{R},m\rangle\, e^{i(\mathbf{k}-\mathbf{Q})\cdot(\mathbf{R}+\mathbf{T})}\\ &= \frac{1}{\sqrt{L_c}}\sum_{\mathbf{R}}^{c}|\mathbf{R},m\rangle\, e^{i(\mathbf{k}-\mathbf{Q})\cdot\mathbf{R}} = |m,\mathbf{k}-\mathbf{Q}\rangle\,,\end{aligned} \tag{9}$$

where, in the first expressions, $\mathbf{R}$ runs over the 4 sites and, in the last expression, over all ($L_c\to\infty$) translations of the cubic lattice. $\mathbf{T}$ runs over all (L_o) translations of the orthorhombic lattice (see figure 2). $|\mathbf{R},m\rangle$ denotes a yz, xz, or xy Wannier orbital with the convention of the middle row in figure 8, so that the energy and shape of the m orbital depends on which of the four types of sites it is centred on. In the $\mathbf{Q}$ representation, the expression for the Hamiltonian matrix becomes:

$$\langle m',\mathbf{k}-\mathbf{Q}'\,|\mathcal{H}|\,m,\mathbf{k}-\mathbf{Q}\rangle = \sum_{\mathbf{R}}^{c} t_{m',m}^{\mathbf{Q}'-\mathbf{Q},\mathbf{R}}\, e^{i(\mathbf{k}-\mathbf{Q})\cdot\mathbf{R}}, \tag{10}$$

with

$$t_{m',m}^{\mathbf{Q},\mathbf{R}} \equiv \frac{1}{4}\sum_{\mathbf{R}'}^{4} t_{m',m}^{\mathbf{R}',\mathbf{R}'+\mathbf{R}}\, e^{i\mathbf{Q}\cdot\mathbf{R}'},$$

and where for simplicity of notation we have dropped the superscript LDA on $\mathcal{H}$. Note that the difference between any of the four $\mathbf{Q}$ vectors also belongs to set (8). If $t_{m',m}^{\mathbf{R}',\mathbf{R}'+\mathbf{R}}$ were independent of $\mathbf{R}'$, as would be the case if the energy and shape of each m orbital were independent of its position, we would have: $t_{m',m}^{\mathbf{Q},\mathbf{R}} = \delta_{\mathbf{Q},\mathbf{0}}\, t_{m',m}^{\mathbf{R}}$, and the Hamiltonian would have cubic translational symmetry. But the $GdFeO_3$-type distortion of the on-site energies and shapes of the Wannier orbitals introduces coupling between the four

orthorhombic subdivisions of the cubic BZ. Each subdivision is denoted by a specific $\mathbf{Q}$ vector in the set (8), or one of their equivalents.

We must now calculate $t^{\mathbf{Q},\mathbf{R}}_{m',m}$ using the unitary matrix,

$$\frac{1}{\sqrt{4}}e^{i\mathbf{Q}\cdot\mathbf{R}} = \frac{1}{\sqrt{4}} \times \begin{array}{|cc|cccc|} \hline \mathbf{Q} & \mathbf{R} & 000 & 010 & 001 & 011 \\ 000 & & 1 & 1 & 1 & 1 \\ \pi\pi 0 & & 1 & -1 & 1 & -1 \\ 00\pi & & 1 & 1 & -1 & -1 \\ \pi\pi\pi & & 1 & -1 & -1 & 1 \\ \hline \end{array},$$

and the space group ($Pbnm$) and orbital symmetries expressed by equations (4) and (3). In order to obtain simple, explicit expressions, let us limit the lattice sum in (10) to include merely the on-site, the six 1st-nearest, and the six t'_σ-type 2nd-nearest-neighbour hoppings. For the latter, we neglect the tiny differences between the three numbers, $t^{011}_{yz,yz} = t^{10\bar{1}}_{xz,xz}$, $t^{101}_{xz,xz} = t^{01\bar{1}}_{yz,yz}$ and $\frac{1}{2}\left(t^{1\bar{1}0}_{xy,xy} + t^{110}_{xy,xy}\right)$. The $\mathbf{Q}'\mathbf{Q}$ matrix element of the Hamiltonian can then be expressed as:

$$\begin{aligned}\langle \mathbf{k}-\mathbf{Q}' \left|\mathcal{H}\right| \mathbf{k}-\mathbf{Q}\rangle = {} & t^{\mathbf{Q}'-\mathbf{Q},000} + 2t^{\mathbf{Q}'-\mathbf{Q},001}c_z + 2t^{\mathbf{Q}'-\mathbf{Q},010}c_y + 2t^{\mathbf{Q}'-\mathbf{Q},100}c_x \\ & + 4t^{\mathbf{Q}'-\mathbf{Q},110}c_xc_y + 4t^{\mathbf{Q}'-\mathbf{Q},101}c_xc_z + 4t^{\mathbf{Q}'-\mathbf{Q},011}c_yc_z + 4\tilde{t}^{\mathbf{Q}'-\mathbf{Q},110}s_xs_y, \end{aligned} \quad (11)$$

where $c_x \equiv \cos(k_x - Q_x)$ and $s_x \equiv \sin(k_x - Q_x)$, etc. In order to specify the $t^{\mathbf{Q},\mathbf{R}}$ matrices in orbital space, it will finally prove convenient to define the following unit, symmetric, and anti-symmetric matrices:

$$E^{yz} \equiv \begin{array}{|c|ccc|} \hline & yz & xz & xy \\ yz & 1 & 0 & 0 \\ xz & 0 & 0 & 0 \\ xy & 0 & 0 & 0 \\ \hline \end{array}, \qquad S^{yz,xz} \equiv \begin{array}{|c|ccc|} \hline & yz & xz & xy \\ yz & 0 & 1 & 0 \\ xz & 1 & 0 & 0 \\ xy & 0 & 0 & 0 \\ \hline \end{array},$$

$$A^{yz,xz} \equiv A^{xz,yz} \equiv \begin{array}{|c|ccc|} \hline & yz & xz & xy \\ yz & 0 & 1 & 0 \\ xz & -1 & 0 & 0 \\ xy & 0 & 0 & 0 \\ \hline \end{array}, \text{ etc.} \quad (12)$$

Note that the A matrices are defined to have 1 or 0 in their upper triangle, and -1 or 0 in their lower triangle.

The $\mathbf{Q} = \mathbf{Q}' = \mathbf{0}$ element, $\langle \mathbf{k} \left|\mathcal{H}\right| \mathbf{k}\rangle$, is a "cubically" averaged 3×3 Hamiltonian. This is a generalization of the non-interacting cubic bands given by (2). Its on-site and 001-hopping matrices are given by:

$$t^{\mathbf{Q}=000,\mathbf{R}=00z} = \left\langle t^{00z}_{\llcorner z,\llcorner z} \right\rangle (E^{yz} + E^{xz}) + t^{00z}_{xy,xy}E^{xy} + t^{00z}_{yz,xz}S^{yz,xz}, \quad (13)$$

if z takes respectively the value 0 and 1. Here, the coefficients are linear combinations of the basic Hamiltonian matrix elements given in tables 1-5. For instance is

$$\left\langle t^{00z}_{\llcorner z,\llcorner z} \right\rangle \equiv \frac{1}{2}\left(t^{00z}_{yz,yz} + t^{00z}_{xz,xz}\right)$$

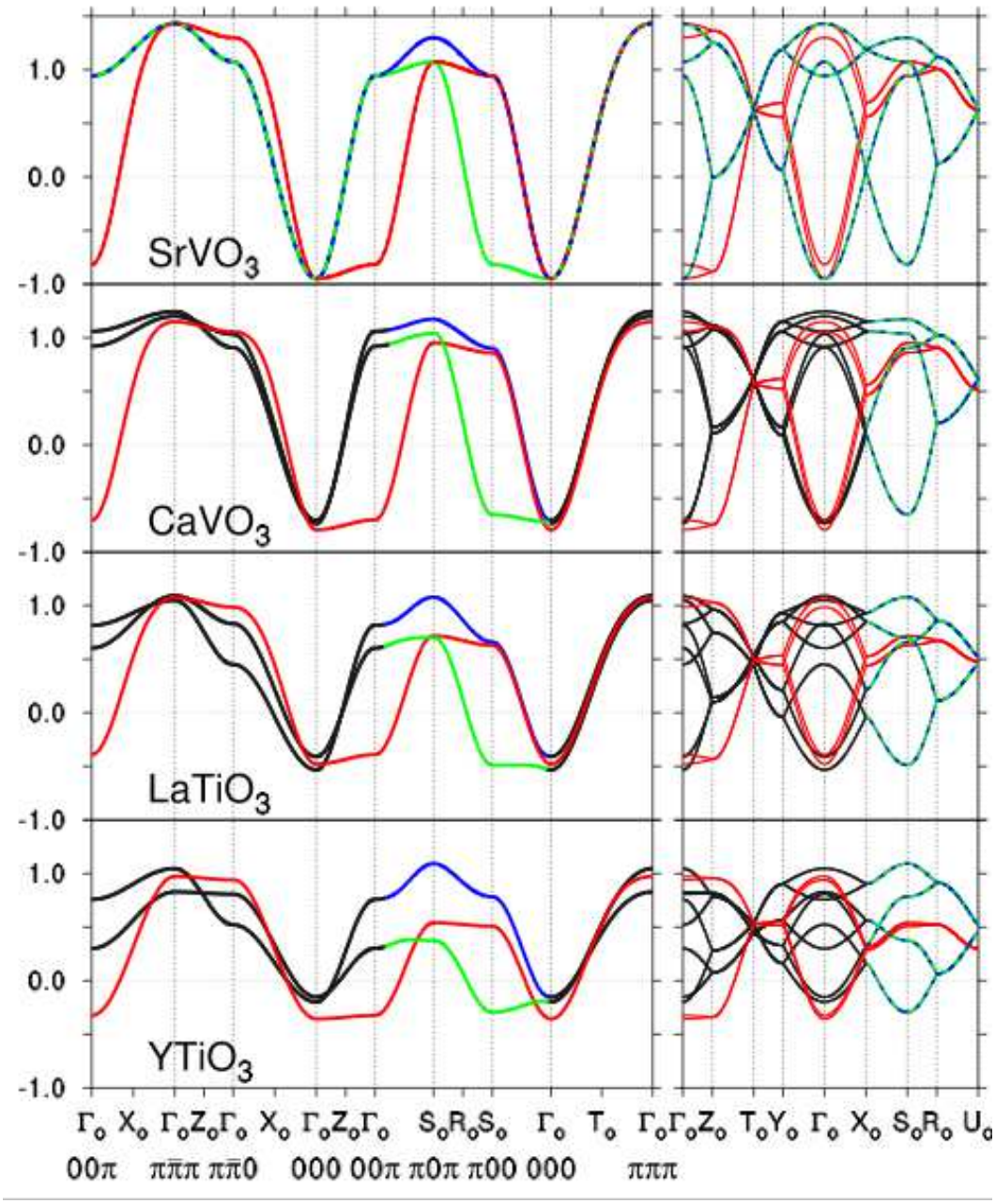

Figure 11. Cubically averaged ($\mathbf{Q} = \mathbf{0}$) t_{2g} LDA bandstructures in eV, in the primitive monoclinic BZ (left), and folded into the orthorhombic BZ (right). The letters above the $k_xk_yk_z$ coordinates denote the orthorhombic high-symmetry points (red in figure 9), $\mathbf{k} + \mathbf{Q}$, into which the corresponding cubic point is folded on the right-hand side. Bands with predominant xy, yz, and zx character are respectively red, green, and blue. Black bands are of strongly mixed yz and zx character. The definitions of characters are those of the middle row in figure 8. The bands were obtained with the parameters for $\mathbf{Q}$=000 in table 9. In order to obtain the bandstructures in figure 10, albeit in the 2nd-nearest neighbour approximation, the folded-in bands should be coupled using the matrix elements (14)–(16).

Table 9. Coefficients of the on-site energies and hopping integrals $t^{\mathbf{Q},\mathbf{R}}$ in meV (see equations (11)–(16))

R		000				001				010/100				
		Sr	Ca	La	Y	Sr	Ca	La	Y		Sr	Ca	La	Y
Q														
000	$\langle t_{\llcorner z,\llcorner z}\rangle$	625	616	488	490	−281	−245	−201	−122	$t_{\shortparallel z,\shortparallel z}$	−281	−223	−185	−184
	$t_{xy,xy}$	625	542	486	417	−33	−23	−22	−8	$t_{xy,xy}$	−281	−231	−183	−162
										$t_{\llcorner z,\llcorner z}$	−33	−17	1	28
	$t_{yz,xz}$	0	4	−42	43	0	−21	−42	−63	$\langle t_{\shortparallel z,\llcorner z}\rangle$	0	6	16	15
$\pi\pi 0$	$t_{yz,yz}$–$t_{xz,xz}$	0	8	−85	−230	0	9	15	113	$t_{yz,xz}$–$t_{xz,yz}$	0	78	118	111
00π	$t_{yz,xy}$+$t_{xz,xy}$	0	−21	−131	−120	0	−11	−7	19	$t_{\shortparallel z,xy}$+$t_{xy,\shortparallel z}$	0	−51	−88	−118
										$t_{\llcorner z,xy}$+$t_{xy,\llcorner z}$	0	8	40	43
$\pi\pi\pi$	$t_{yz,xy}$–$t_{xz,xy}$	0	−13	−47	−86	0	−61	−111	−147	$t^{010}_{yz,xy}$–$t^{010}_{xy,yz}$	0	17	20	10
										$t^{010}_{xz,xy}$–$t^{010}_{xy,xz}$	0	58	106	87

R		110/011/101			
		Sr	Ca	La	Y
Q					
000	t'_σ	−96	−91	−47	−27
	s'_σ	0	7	1	29

the on-site energy or 001 t_π hopping integral, averaged over the yz and xz orbitals. The matrices for hopping parallel to the mirror plane ($\mathbf{R} = 010$ or 100) have the very similar form:

$$t^{\mathbf{Q}=000,\mathbf{R}=010/100} = t_{\shortparallel z,\shortparallel z} E^{\shortparallel z} + t_{\llcorner z,\llcorner z} E^{\llcorner z} + t_{xy,xy} E^{xy} + \langle t_{\shortparallel z,\llcorner z}\rangle\, S^{\shortparallel z,\llcorner z},$$

where $\shortparallel$ and $\llcorner$, respectively, denote the directions parallel and perpendicular to the direction of the hop, *i.e.*, for $\mathbf{R} = 010$, $\shortparallel = y$ and $\llcorner = x$, whereas for $\mathbf{R} = 100$, $\shortparallel = x$ and $\llcorner = y$. So the first three terms are the t_π or t_δ hoppings in the plane, and the last term is the average of the hopping *between* the yz and xz orbitals along 010, or 100:

$$\langle t_{\shortparallel z,\llcorner z}\rangle \equiv \frac{1}{2}\left(t_{\shortparallel z,\llcorner z} + t_{\llcorner z,\shortparallel z}\right) = \frac{1}{2}\left(t^{010}_{yz,xz} + t^{010}_{xz,yz}\right) = \frac{1}{2}\left(t^{100}_{xz,yz} + t^{100}_{yz,xz}\right).$$

Remember that $t^{100}_{yz,xz} = t^{010}_{yz,xz} \neq t^{010}_{xz,yz} = t^{100}_{xz,yz}$. The hopping to the 2nd-nearest neighbours will be *diagonal* in both orbital and $\mathbf{Q}$ spaces:

$$t^{\mathbf{Q},110} = \delta_{\mathbf{Q},\mathbf{0}}\, t'_\sigma\, E^{xy}, \quad t^{\mathbf{Q},101} = \delta_{\mathbf{Q},\mathbf{0}}\, t'_\sigma\, E^{xz}, \quad t^{\mathbf{Q},011} = \delta_{\mathbf{Q},\mathbf{0}}\, t'_\sigma\, E^{yz}, \quad \tilde{t}^{\mathbf{Q},110} = \delta_{\mathbf{Q},\mathbf{0}}\, s'_\sigma\, E^{xy},$$

as a consequence of the approximation made above. Here,

$$t'_\sigma = \frac{1}{6}\left[t^{1\bar{1}0}_{xy,xy} + t^{110}_{xy,xy} + 2\left(t^{011}_{yz,yz} + t^{101}_{xz,xz}\right)\right], \text{ and } s'_\sigma = \frac{1}{2}\left(t^{1\bar{1}0}_{xy,xy} - t^{110}_{xy,xy}\right).$$

Note that in these expressions, and in (14)–(16) below, the $t^{\mathbf{Q},\mathbf{R}}$, E, S, and A matrices in orbital space are the *only* such matrices; the prefactors, such as $t^{001}_{xy,xz}$, are parameters and their subscripts do not label elements of 3×3 matrices.

The values of these parameters are displayed in table 9, whose top four rows, denoted $\mathbf{Q}$=000, determine the cubically averaged bands. We see that in $SrVO_3$ and $LaTiO_3$ the average (on-site) energy of the xy band is the same as the common, average energy of the yz and xz bands, whereas in $CaVO_3$ and $YTiO_3$, it is ∼75 meV lower. The values of the hopping integrals confirm that the cubically averaged bands narrow along the series (due to misalignment and increased theft of oxygen character), and that the hopping in the z direction is anomalously small in $YTiO_3$, which therefore has the most anisotropic t_{2g} band. The reason for that is the smallness of $t^{001}_{yz,yz}$ due to hybridization with Y $4d_{xy}$, as was discussed in connection with equation (5).

The cubically averaged bandstructures are shown in figure 11. We clearly see how these bands develop from the cubic, non-interacting, nearly two-dimensional xy, yz, and xz bands of $SrVO_3$ into three distorted, monoclinic bands in which nearly degenerate yz and xz levels split by $\pm\left[t^{000}_{yz,xz} + 2t^{001}_{yz,xz}\cos k_z + 2\left\langle t_{\shortparallel z,\llcorner z}\right\rangle(\cos k_x + \cos k_y)\right]$. The xy band (red) stays pure and nearly two-dimensional. For $YTiO_3$, the weak k_z dispersion of the yz band (green) is clearly seen in the (010) plane where there is no mixing with xz. The xz band (blue) will have the same behaviour in the (100) plane in this cubically averaged bandstructure. The letters Γ_o, T_o, S_o, R_o, Z_o, and X_o on the abscissa refer to the orthorhombic high-symmetry points, $\mathbf{k}+\mathbf{Q}$ (red in figure 9), into which the monoclinic $\mathbf{k}$ points (blue in figure 9) should be folded prior to $\mathbf{Q}$-coupling. The folded-in bands are shown on the right-hand side, and comparison with the real t_{2g} bands in figure 10 reveals that, in fact, the cubically averaged bandstructures go "halfway" towards the real bandstructures.

The *hybridization* between two cubically averaged bandstructures displaced in $\mathbf{k}$ space by the orthorhombic reciprocal lattice vector $\mathbf{Q}$=$\pi\pi$0 is given by the matrix (11) with:

$$\begin{aligned} 2t^{\mathbf{Q}=\pi\pi0,\mathbf{R}=00z} &= \left(t^{00z}_{yz,yz} - t^{00z}_{xz,xz}\right)\left(E^{yz} - E^{xz}\right) \\ 2t^{\mathbf{Q}=\pi\pi0,\mathbf{R}=010/100} &= \left(t_{yz,xz} - t_{xz,yz}\right)A^{yz,xz}, \end{aligned} \tag{14}$$

and is seen to express the asymmetry between the yz and xz orbitals, as well as the coupling between them. Here, the top line provides the Δ splitting by $\left(t^{000}_{yz,yz} - t^{000}_{xz,xz}\right) + 2\left(t^{001}_{yz,yz} - t^{001}_{xz,xz}\right)c_z$ of the $\varepsilon_{yz}(\mathbf{k})$ and $\varepsilon_{yz}(\mathbf{k}-\pi\pi0)$ bands at their crossings. The same holds for the splitting of the $\varepsilon_{xz}(\mathbf{k})$ and $\varepsilon_{xz}(\mathbf{k}-\pi\pi0)$ bands. Note that since $t^{00z}_{yz,yz} - t^{00z}_{xz,xz}$ is a parameter, it should *not* be substituted by $t^{00z}_{xz,xz} - t^{00z}_{yz,yz}$ when describing the xz band, because that change of sign is accounted for as a prefactor to E^{xz}. Note also that $t^{010}_{yz,xz} - t^{010}_{xz,yz} = t^{100}_{yz,xz} - t^{100}_{xz,yz}$ because $t^{010}_{yz,xz} = t^{100}_{yz,xz} \neq t^{100}_{xz,yz} = t^{010}_{xz,yz}$.

Similarly, the hybridization between two cubically averaged bandstructures

displaced by $\mathbf{Q}{=}00\pi$ is specified by:

$$\begin{aligned} 2t^{\mathbf{Q}=00\pi,\mathbf{R}=000} &= \left(t^{000}_{yz,xy}+t^{000}_{xz,xy}\right)\left(S^{yz,xy}+S^{xz,xy}\right) \\ 2t^{\mathbf{Q}=00\pi,\mathbf{R}=001} &= \left(t^{001}_{yz,xy}+t^{001}_{xz,xy}\right)\left(A^{yz,xy}+A^{xz,xy}\right) \\ 2t^{\mathbf{Q}=00\pi,\mathbf{R}=010/100} &= \left(t_{\shortparallel z,xy}+t_{xy,\shortparallel z}\right)S^{\shortparallel z,xy}+\left(t_{\llcorner z,xy}+t_{xy,\llcorner z}\right)S^{\llcorner z,xy}, \end{aligned} \tag{15}$$

and is seen to express the average of the coupling from the xy orbital to the yz and xz orbitals. As above, $\shortparallel$ and $\llcorner$ denote the direction parallel and perpendicular to the direction of the hop, *i.e.*, for $\mathbf{R}=010$, $\shortparallel = y$ and $\llcorner = x$, whereas for $\mathbf{R}=100$, $\shortparallel = x$ and $\llcorner = y$. Note that $t^{001}_{iz,xy}=-t^{001}_{xy,iz}$, that $t^{010}_{yz,xy}=t^{100}_{xy,xz}\neq t^{100}_{xz,xy}=t^{010}_{xy,yz}$, and that $t^{010}_{xz,xy}=t^{100}_{xy,yz}\neq t^{100}_{yz,xy}=t^{010}_{xy,xz}$.

Finally, two cubic bands displaced by $\mathbf{Q}{=}\pi\pi\pi$ hybridize by means of a matrix (11) specified by:

$$\begin{aligned} 2t^{\mathbf{Q}=\pi\pi\pi,\mathbf{R}=000} &= \left(t^{000}_{yz,xy}-t^{000}_{xz,xy}\right)\left(S^{yz,xy}-S^{xz,xy}\right) \\ 2t^{\mathbf{Q}=\pi\pi\pi,\mathbf{R}=001} &= \left(t^{001}_{yz,xy}-t^{001}_{xz,xy}\right)\left(A^{yz,xy}-A^{xz,xy}\right) \\ 2t^{\mathbf{Q}=\pi\pi\pi,\mathbf{R}=010} &= \left(t^{010}_{yz,xy}-t^{010}_{xy,yz}\right)A^{yz,xy}+\left(t^{010}_{xz,xy}-t^{010}_{xy,xz}\right)A^{xz,xy} \\ 2t^{\mathbf{Q}=\pi\pi\pi,\mathbf{R}=100} &= -\left(t^{010}_{xz,xy}-t^{010}_{xy,xz}\right)A^{yz,xy}-\left(t^{010}_{yz,xy}-t^{010}_{xy,yz}\right)A^{xz,xy} \\ &= \left(t^{100}_{yz,xy}-t^{100}_{xy,yz}\right)A^{yz,xy}+\left(t^{100}_{xz,xy}-t^{100}_{xy,xz}\right)A^{xz,xy} \end{aligned} \tag{16}$$

This matrix expresses the difference between the couplings from xy to yz and to xz. We emphasize that there is no $\mathbf{Q}$ coupling between xy bands.

The values of the coefficients given in table 9 exhibit the general trend that the non-cubic perturbations increase along the series. We also see that *details* differ: which ones of the many non-cubic couplings dominate depends on the material. Moreover, the on-site, $\mathbf{k}$-averaged splittings, $t^{000}_{yz,yz}-t^{000}_{xz,xz}$, and inter-orbital couplings, $t^{000}_{yz,xy}\pm t^{000}_{xz,xy}$, are not much larger than their modulations given by the corresponding hopping integrals. This is very different from the situation in materials with strong JT distortions, where $\mathbf{Q}$ coupling due to on-site terms dominate. So according to the present conventional description of the t_{2g} perovskites in terms of $\mathbf{Q}$ couplings, the distortion from the cubically averaged to the real bandstructure is the sum of several terms with varying signs.

As a most important example, let us discuss the *pseudo-gap.* More specifically, let us estimate the levels at S_o $\pi 00$ with intermediate energy by using expressions (11)–(16), table 9, and figure 11:

The relevant cubically averaged yz levels are those at $\mathbf{k}-\mathbf{Q}=\pi 00-00\pi=\pi 0\bar{\pi}$ and $\pi 00-\pi\pi 0=0\bar{\pi}0$. Their energies are:

$$\begin{aligned} &\varepsilon_{yz}(\pi 0\pi)\ /\ \varepsilon_{yz}(0\pi 0)=\left\langle t^{000}_{\llcorner z,\llcorner z}\right\rangle-4t'_\sigma\mp 2\left(\left\langle t^{001}_{\llcorner z,\llcorner z}\right\rangle-t_{\shortparallel z,\shortparallel z}+t_{\llcorner z,\llcorner z}\right) \\ &=\begin{pmatrix} 1009 & 980 & 676 & 598\end{pmatrix}\mp\begin{pmatrix} -66 & -58 & -30 & 180\end{pmatrix} \\ &=\begin{pmatrix} 1075 & 1038 & 706 & 418\end{pmatrix}\Big/\begin{pmatrix} 943 & 922 & 646 & 778\end{pmatrix}\ \text{meV} \end{aligned}$$

for $SrVO_3$ through $YTiO_3$. Note that in $YTiO_3$, the $\varepsilon_{yz}(\pi 0\pi)$ energy is anomalously low, as is also seen in figure 11. This is one reason for the pronounced pseudo-gap in that

material. The yz levels are separated by $\mathbf{Q}' - \mathbf{Q}{=}\pi\pi\bar{\pi}$ and, according to (16), or table 9, do therefore not couple. Degenerate with these yz levels are the cubically averaged xz levels,

$$\varepsilon_{xz}\left(0\pi\pi\right)/\varepsilon_{xz}\left(\pi 00\right) = \varepsilon_{yz}\left(\pi 0\pi\right)/\varepsilon_{yz}\left(0\pi 0\right),$$

at $\mathbf{k}-\mathbf{Q} = \pi 00 - \pi\pi\pi = 0\bar{\pi}\bar{\pi}$ and $\pi 00 - 000 = \pi 00$. Also these xz levels are separated by $\pi\pi\pi$, and do therefore not couple with each other. The yz level at $\pi 0\bar{\pi}$ and the xz level at $0\bar{\pi}\bar{\pi}$ are separated by $\pi\pi 0$ and therefore couple via a matrix element obtained from equation (14), which is seen to vanish, however, because $c_x + c_y = 0$. The same holds for the yz level at $0\bar{\pi}0$ and the xz level at $\pi 00$. Finally, the yz level at $\pi 0\bar{\pi}$ and the xz level at $\pi 00$ are separated by 00π so that, according to (15) or table 9, they do not couple. In conclusion, the four yz and xz states at S_o with intermediate energy can only couple via xy states, which we consider next:

When folded into S_o, all four cubically averaged xy bands (the red ones in figure 11) are nearly degenerate. One pair of degenerate levels come from $\mathbf{k} - \mathbf{Q}' = \pi 00 - 00\pi = \pi 0\bar{\pi}$ and $\pi 00 - \pi\pi\pi = 0\bar{\pi}\bar{\pi}$, and the other from $\mathbf{k} - \mathbf{Q}' = \pi 00 - 000 = \pi 00$ and $\pi 00 - \pi\pi 0 = 0\bar{\pi}0$. As for the yz and xz levels, the two xy energies are those of $\pi 0\pi$ and $\pi 00$ points, specifically:

$$\begin{aligned}
\left[\varepsilon_{xy}\left(\pi 0\pi\right){=}\varepsilon_{xy}\left(0\pi\pi\right)\right] \;/\; \left[\varepsilon_{xy}\left(\pi 00\right){=}\varepsilon_{xy}\left(0\pi 0\right)\right] &= t^{000}_{xy,xy} - 4t'_\sigma \mp 2t^{001}_{xy,xy} \\
&= \begin{pmatrix} 1009 & 906 & 674 & 525 \end{pmatrix} \mp \begin{pmatrix} -66 & -46 & -44 & -16 \end{pmatrix} \\
&= \begin{pmatrix} 1075 & 952 & 718 & 541 \end{pmatrix} \Big/ \begin{pmatrix} 943 & 860 & 630 & 509 \end{pmatrix} \text{ meV}.
\end{aligned}$$

Since there is no $\mathbf{Q}$-coupling between xy bands, we now only have to couple xy to yz and xz.

The yz level at $\pi 0\bar{\pi}$ couples to the lowest, degenerate xy level, that is the level at $\pi 00$ and $0\bar{\pi}0$, because for those, $\mathbf{Q}' - \mathbf{Q} = \pi 0\bar{\pi} - \pi 00 = 00\bar{\pi}$ and $\pi 0\bar{\pi} - 0\bar{\pi}0 = \pi\pi\bar{\pi}$, respectively. It does, however, not couple to the xy level at $\pi 0\pi$, because for those states, $\mathbf{Q}' - \mathbf{Q} = \pi 0\bar{\pi} - \pi 0\bar{\pi} = 000$ and $\pi 0\bar{\pi} - 0\bar{\pi}\bar{\pi} = \pi\pi 0$. Similarly, the xz level at $0\bar{\pi}\bar{\pi}$, which is degenerate with the yz level at $\bar{\pi}0\bar{\pi}$, also couples to the xy level at $\pi 00$ and $0\bar{\pi}0$, because, here, $\mathbf{Q}' - \mathbf{Q} = 0\bar{\pi}\bar{\pi} - \pi 00 = \bar{\pi}\bar{\pi}\bar{\pi}$ and $0\bar{\pi}\bar{\pi} - 0\bar{\pi}0 = 00\bar{\pi}$. As for the yz level, the xz level does not couple to the xy level at $0\pi\pi$.

The yz level at $0\bar{\pi}0$, which is lower than the one at $\pi 0\bar{\pi}$, except in $YTiO_3$, couples to the highest, degenerate xy level, the one at $\pi 0\bar{\pi}$ and $0\bar{\pi}\bar{\pi}$, because for those, $\mathbf{Q}' - \mathbf{Q} = 0\bar{\pi}0 - \pi 0\bar{\pi} = \bar{\pi}\bar{\pi}\pi$ and $0\bar{\pi}0 - 0\bar{\pi}\bar{\pi} = 00\pi$. It does not couple to the xy level at $0\bar{\pi}0$. Similarly, the xz level at $\pi 00$ couples to the xy level at $\pi 0\bar{\pi}$ and $0\bar{\pi}\bar{\pi}$, because $\mathbf{Q}' - \mathbf{Q} = \pi 00 - \pi 0\bar{\pi} = 00\pi$ and $\pi 00 - 0\bar{\pi}\bar{\pi} = \pi\pi\pi$. Again, there is no coupling between xz and xy levels at $\pi 00$.

All couplings relevant for the pseudo-gap at S_o thus have $\mathbf{Q}' - \mathbf{Q} = 00\pi$ and $\pi\pi\pi$, and are therefore described by the five hopping parameters listed in the corresponding rows of table 9. We emphasize that the dominant crystal-field coupling, caused by $t^{000}_{yz,yz} - t^{000}_{xz,xz}$, has $\mathbf{Q}' - \mathbf{Q} = \pi\pi 0$, and is therefore not relevant for the pseudo-gap at S_o.

For the couplings via $\mathbf{Q}' - \mathbf{Q} = 00\pi$, we find from equations (11) and (15):

$$\begin{aligned}\langle xy, \pi 00 \,|\mathcal{H}|\, \pi 0\pi, yz\rangle &= \langle xy, 0\pi 0 \,|\mathcal{H}|\, 0\pi\pi, xz\rangle \\ &= \frac{1}{2}\left(t^{000}_{yz,xy} + t^{000}_{xz,xy}\right) + \left(t^{001}_{yz,xy} + t^{001}_{xz,xy}\right) + \left(t_{\shortparallel z,xy} + t_{xy,\shortparallel z}\right) - \left(t_{\llcorner z,xy} + t_{xy,\llcorner z}\right) \\ &= \frac{1}{2}\Big(-21\ -131\ -120\Big) + \Big(-11\ -7\ 19\Big) + \Big(-51\ -88\ -118\Big) - \Big(8\ 40\ 43\Big) \\ &= \Big(-81\ -201\ -202\Big)\ \text{meV},\end{aligned}$$

for $CaVO_3$ through $YTiO_3$. These couplings are numerically large for the titanates because terms add up. The other 00π couplings are:

$$\begin{aligned}\langle xy, 0\pi\pi \,|\mathcal{H}|\, 0\pi 0, yz\rangle &= \langle xy, \pi 0\pi \,|\mathcal{H}|\, \pi 00, xz\rangle \\ &= \frac{1}{2}\left(t^{000}_{yz,xy} + t^{000}_{xz,xy}\right) - \left(t^{001}_{yz,xy} + t^{001}_{xz,xy}\right) - \left(t_{\shortparallel z,xy} + t_{xy,\shortparallel z}\right) + \left(t_{\llcorner z,xy} + t_{xy,\llcorner z}\right) \\ &= \frac{1}{2}\Big(-21\ -131\ -120\Big) - \Big(-11\ -7\ 19\Big) - \Big(-51\ -88\ -118\Big) + \Big(8\ 40\ 43\Big) \\ &= \Big(60\ 70\ 82\Big)\ \text{meV},\end{aligned}$$

which are small for the titanates due to cancellation of terms. For the couplings via $\mathbf{Q}' - \mathbf{Q} = \pi\pi\pi$ we find from expressions (16):

$$\begin{aligned}\langle xy, 0\pi 0 \,|\mathcal{H}|\, \pi 0\pi, yz\rangle &= -\langle xy, \pi 00 \,|\mathcal{H}|\, 0\pi\pi, xz\rangle \\ &= \frac{1}{2}\left(t^{000}_{yz,xy} - t^{000}_{xz,xy}\right) + \left(t^{001}_{yz,xy} - t^{001}_{xz,xy}\right) - \left(t^{010}_{yz,xy} - t^{010}_{xy,yz}\right) - \left(t^{010}_{xz,xy} - t^{010}_{xy,xz}\right) \\ &= \frac{1}{2}\Big(-13\ -47\ -86\Big) + \Big(-61\ -111\ -147\Big) - \Big(17\ 20\ 10\Big) - \Big(58\ 106\ 87\Big) \\ &= \Big(-143\ -261\ -287\Big)\ \text{meV},\end{aligned}$$

which are large for all three materials, and

$$\begin{aligned}\langle xy, \pi 0\pi \,|\mathcal{H}|\, 0\pi 0, yz\rangle &= -\langle xy, 0\pi\pi \,|\mathcal{H}|\, \pi 00, xz\rangle \\ &= \frac{1}{2}\left(t^{000}_{yz,xy} - t^{000}_{xz,xy}\right) - \left(t^{001}_{yz,xy} - t^{001}_{xz,xy}\right) + \left(t^{010}_{yz,xy} - t^{010}_{xy,yz}\right) + \left(t^{010}_{xz,xy} - t^{010}_{xy,xz}\right) \\ &= \frac{1}{2}\Big(-13\ -47\ -86\Big) - \Big(-61\ -111\ -147\Big) + \Big(17\ 20\ 10\Big) + \Big(58\ 106\ 87\Big) \\ &= \Big(130\ 214\ 201\Big)\ \text{meV},\end{aligned}$$

which are large as well.

Finally, we can form the matrix $\langle \pi 00 - \mathbf{Q}' \,|\mathcal{H}|\, \pi 00 - \mathbf{Q}\rangle$ for the 8 states of intermediate energy at S_o. This matrix blocks into two. The first block involves the states: $|xy, \pi 00 - 000\rangle$, $|xy, \pi 00 - \pi\pi 0\rangle$, $|yz, \pi 00 - 00\pi\rangle$, and $|xz, \pi 00 - \pi\pi\pi\rangle$. Along its diagonal, it has the degenerate levels $\varepsilon_{xy}(\pi 00)$ and $\varepsilon_{xy}(0\pi 0)$, followed by the degenerate levels $\varepsilon_{yz}(\pi 0\pi)$ and $\varepsilon_{xz}(0\pi\pi)$. The off-diagonal elements are: $\langle xy, \pi 00 \,|\mathcal{H}|\, \pi 0\pi, yz\rangle = \langle xy, 0\pi 0 \,|\mathcal{H}|\, 0\pi\pi, xz\rangle$ and $\langle xy, 0\pi 0 \,|\mathcal{H}|\, \pi 0\pi, yz\rangle = -\langle xy, \pi 00 \,|\mathcal{H}|\, 0\pi\pi, xz\rangle$. The states contributing to the second block are: $|zx, \pi 00 - 000\rangle$, $|yz, \pi 00 - \pi\pi 0\rangle$, $|xy, \pi 00 - 00\pi\rangle$, and $|xy, \pi 00 - \pi\pi\pi\rangle$. Along its diagonal, there are the degenerate levels $\varepsilon_{xz}(\pi 00)$ and $\varepsilon_{yz}(0\pi 0)$, followed by the degenerate $\varepsilon_{xy}(\pi 0\pi)$ and $\varepsilon_{xy}(0\pi\pi)$ levels. Its off-diagonal

elements are: $\langle xy, 0\pi\pi\,|\mathcal{H}|\,0\pi0, yz\rangle = \langle xy, \pi0\pi\,|\mathcal{H}|\,\pi00, xz\rangle$ and $\langle xy, \pi0\pi\,|\mathcal{H}|\,0\pi0, yz\rangle = -\langle xy, 0\pi\pi\,|\mathcal{H}|\,\pi00, xz\rangle$. Each of these 4×4 blocks can now be transformed into two degenerate 2×2 blocks. For the first set of states, this 2×2 block is simply:

$$\begin{pmatrix} \varepsilon_{xy}(\pi00) = \varepsilon_{xy}(0\pi0) & \sqrt{\langle xy, \pi00\,|\mathcal{H}|\,\pi0\pi, yz\rangle^2 + \langle xy, 0\pi0\,|\mathcal{H}|\,\pi0\pi, yz\rangle^2} \\ \text{hc} & \varepsilon_{yz}(\pi0\pi) = \varepsilon_{xz}(0\pi\pi) \end{pmatrix} =$$

$$\begin{pmatrix} 860 & \sqrt{81^2+143^2} \\ \text{hc} & 1038 \end{pmatrix}, \begin{pmatrix} 630 & \sqrt{201^2+261^2} \\ \text{hc} & 706 \end{pmatrix}, \begin{pmatrix} 509 & \sqrt{202^2+287^2} \\ \text{hc} & 418 \end{pmatrix} \text{ meV},$$

where we have inserted the values for $CaVO_3$ through $YTiO_3$. Note that the size of the hybridization is $\sqrt{2}$ larger than a typical matrix element. Diagonalization yields the corresponding S_o levels:

$$\varepsilon_1(S_o) = \begin{pmatrix} 762 \\ 1136 \end{pmatrix}, \begin{pmatrix} 336 \\ 1000 \end{pmatrix}, \begin{pmatrix} 817 \\ 110 \end{pmatrix} \text{ meV}.$$

The 2×2 matrix and eigenvalues for the second set of states are respectively:

$$\begin{pmatrix} \varepsilon_{xy}(\pi0\pi) = \varepsilon_{xy}(0\pi\pi) & \sqrt{\langle xy, 0\pi\pi\,|\mathcal{H}|\,0\pi0, yz\rangle^2 + \langle xy, \pi0\pi\,|\mathcal{H}|\,0\pi0, yz\rangle^2} \\ \text{hc} & \varepsilon_{yz}(0\pi0) = \varepsilon_{xz}(\pi00) \end{pmatrix} =$$

$$\begin{pmatrix} 952 & \sqrt{60^2+130^2} \\ \text{hc} & 922 \end{pmatrix}, \begin{pmatrix} 718 & \sqrt{70^2+214^2} \\ \text{hc} & 646 \end{pmatrix}, \begin{pmatrix} 541 & \sqrt{82^2+201^2} \\ \text{hc} & 778 \end{pmatrix} \text{ meV}$$

and

$$\varepsilon_2(S_o) = \begin{pmatrix} 1081 \\ 793 \end{pmatrix}, \begin{pmatrix} 910 \\ 454 \end{pmatrix}, \begin{pmatrix} 412 \\ 907 \end{pmatrix} \text{ meV}$$

We realize that these eigenvalues give the trends well, although accurate agreement with the bands in figure 10 requires inclusion also of the remaining 4 states at S_o, as well as inclusion of longer-range hoppings. The decrease through the series of the lowest, degenerate eigenvalue, that is, of the 3rd and 4th bands at S_o, from 943 meV in $SrVO_3$ and 762 meV in $CaVO_3$ to 336 meV in $LaTiO_3$ and, finally, to 110 meV in $YTiO_3$ is spectacular. Note also the inversion of the cubically averaged $\varepsilon_{yz}(\pi0\pi) = \varepsilon_{xz}(0\pi\pi)$ and $\varepsilon_{xy}(\pi00) = \varepsilon_{xy}(0\pi0)$ levels in $YTiO_3$. In *both* titanates, the couplings between the xy and the yz and xz Bloch waves are strong, but the anomalously low-lying $\varepsilon_{yz}(\pi0\pi) = \varepsilon_{xz}(\pi00)$ in $YTiO_3$ makes the difference.

The chemical reason for the development of the pseudo-gap is the increasing residual A character in the t_{2g} band. This was mentioned before and is demonstrated for the titanates in figure 12, where we have projected the bands onto the A $d_{3z^2_{111}-1}$ and A d_{xy} partial waves. The lowering of the 5th band near Γ_o and the 3rd and 4th bands near X is clearly correlated with, respectively, the A $d_{3z^2_{111}-1}$ and A d_{xy} characters. The cause for this lowering is therefore likely to be hybridization with the above-lying A bands. We saw in section 2 that the $GdFeO_3$-type distortion is larger in $YTiO_3$ than in $LaTiO_3$, because Y^{3+} is smaller than La^{3+}, and because the Y $4d$ bands are lower and

more narrow than the La $5d$ bands (figure 1). As a result, the A d character left behind to hybridize with the Ti t_{2g} band is different in the two cases, and this together with the electrostatics is the reason why the shape of these bands, and, hence, the *orbital orders,* to be considered below, are very different.

In the far right-hand side of figure 12 we have shown the bandstructure calculated for the structure measured at 16 GPa, in which the JT distortion is nearly absent, the $GdFeO_3$-type distortion is slightly increased, and the A positions have moved most [9]. As seen from table 7 and as mentioned at the end of section 3.5, at 16 GPa the crystal-field splitting $t^{000}_{yz,yz} - t^{000}_{xz,xz}$ is reduced from -230 to -167 meV, the crystal-field coupling $t^{000}_{yz,xy} - t^{000}_{xz,xy}$ is increased from -86 (see table 9) to -106 meV, and the anomalously small hopping integral, $t^{001}_{yz,yz}$, is decreased from -65 to -41 meV. As expected, the pseudo-gap *and* the A d_{xy} character have both increased. So at 16 GPa, the bandstructure of $YTiO_3$ is distorted more, rather than less away from the cubic bandstructure of $SrVO_3$.

Still, one may ask: is it the displacement or the scattering properties of the A ion by which the band shape (the pseudo-gap) is determined. To answer this, we have performed LMTO calculations of the bandstructure of $LaTiO_3$ using the crystal structure of $YTiO_3$, both with the cell volume of $YTiO_3$ and with that of $LaTiO_3$. We have also calculated the bandstructure of $YTiO_3$ using the crystal structure of $LaTiO_3$, both with the cell volume of $LaTiO_3$ and with that of $YTiO_3$. In all cases, the result was that, given the structure, it is the $GdFeO_3$-distortion rather than the nature of the A ion which determines the shape of the t_{2g} band.

Let us finally demonstrate that the JT distortion is not the reason for the development of the pseudo-gap. The blue t_{2g} bands in figure 13 are those of $YTiO_3$ with the real, JT-distorted structure, which amounts to a 3% stretch of the O2 square into a rhomb in the y direction in subcells 1 and 3, and in the x direction in subcells 2 and 4. The dashed red bands in the left-hand figure were obtained for the hypothetical structure with perfect TiO_6 octahedra discussed in connection with table 7. We see that the band shapes, in particular those of the pseudo-gap, are *the same,* compared for instance with the huge difference in band shapes between $LaTiO_3$ and $YTiO_3$. The results for the 16 GPa structure, in which the JT distortion is minimal, confirm this conclusion.

3.7. Crystal-field representation and orbital order

Since for the titanates the calculated crystal-field splittings are an order of magnitude larger than the spin-orbit splitting (20 meV) and the magnetic ordering temperatures, it will prove useful to transform from the yz, zx, and xy Wannier orbitals to those linear combinations, $|1\rangle$, $|2\rangle$, and $|3\rangle$, which diagonalize the on-site LDA t_{2g} Hamiltonian, t^{000}, given in the first column of tables 1–5 and 7. Of these so-called crystal-field orbitals, $|1\rangle$ has the lowest energy and $|3\rangle$ the highest. In $CaVO_3$ the lowest orbital remains almost purely xy, in $LaTiO_3$ it is a fairly equal mixture of all three orbitals, and in $YTiO_3$ it is a mixture of yz and xy only.

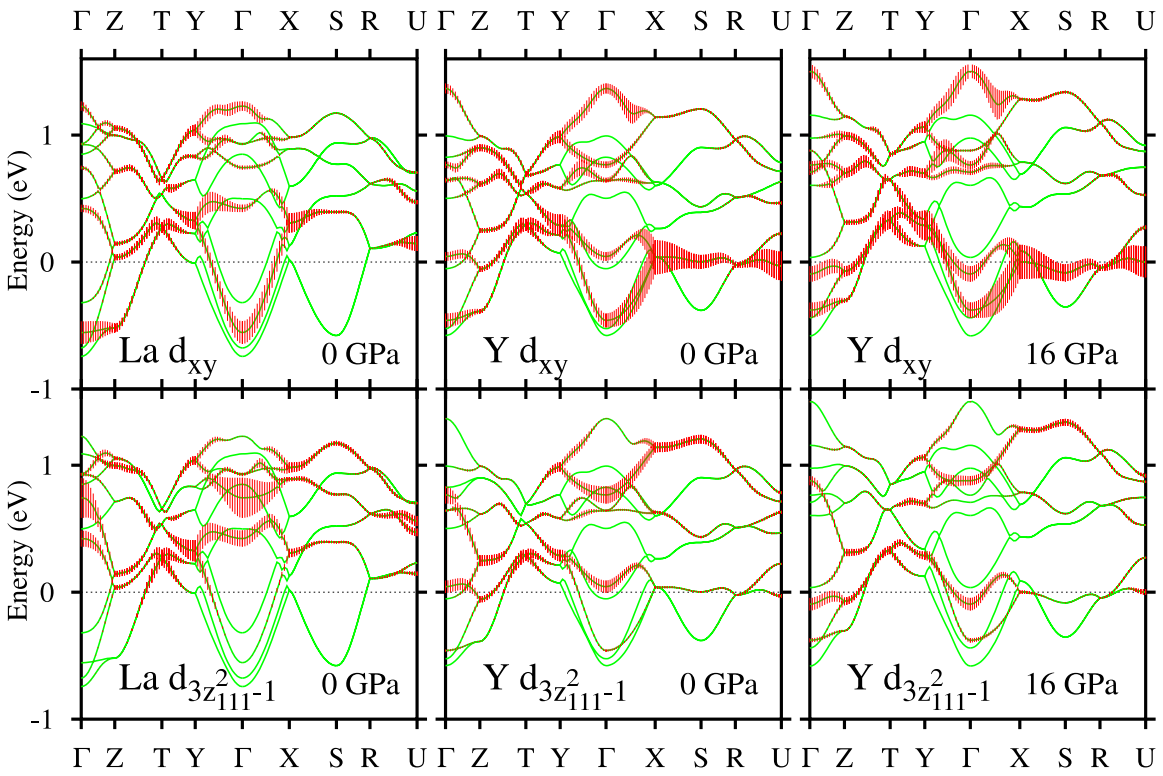

Figure 12. LDA LMTO bandstructures of $LaTiO_3$ [12] and $YTiO_3$ at normal and 16 GPa pressure [9]. The bands have been decorated with A d_{xy} and A $(d_{xy}+d_{yx}+d_{xz})/\sqrt{3}$ partial-wave characters, averaged over all A sites. These characters are seen in figure 15 to be characteristic for the lowest crystal-field orbital.

Specifically for $CaVO_3$, the eigenvalues relatively to ε_F and the eigenvectors at site 000 are respectively:

$$\begin{aligned}\begin{pmatrix}\epsilon_1 & \epsilon_2 & \epsilon_3\end{pmatrix} &= \begin{pmatrix}538 & 610 & 625\end{pmatrix}\ \text{meV} \qquad \text{and}\\ \begin{pmatrix}|1\rangle & |2\rangle & |3\rangle\end{pmatrix} &= \begin{pmatrix}|yz\rangle & |xz\rangle & |xy\rangle\end{pmatrix}\begin{pmatrix}.202 & -.340 & .918\\ .042 & .940 & .339\\ .979 & .030 & -.204\end{pmatrix}.\end{aligned} \tag{17}$$

For $LaTiO_3$ with the older data [44], we get:

$$\begin{aligned}\begin{pmatrix}\epsilon_1 & \epsilon_2 & \epsilon_3\end{pmatrix} &= \begin{pmatrix}398 & 537 & 608\end{pmatrix}\ \text{meV} \qquad \text{and}\\ \begin{pmatrix}|1\rangle & |2\rangle & |3\rangle\end{pmatrix} &= \begin{pmatrix}|yz\rangle & |xz\rangle & |xy\rangle\end{pmatrix}\begin{pmatrix}.715 & -.609 & .344\\ .353 & .739 & .574\\ .604 & .289 & -.743\end{pmatrix},\end{aligned} \tag{18}$$

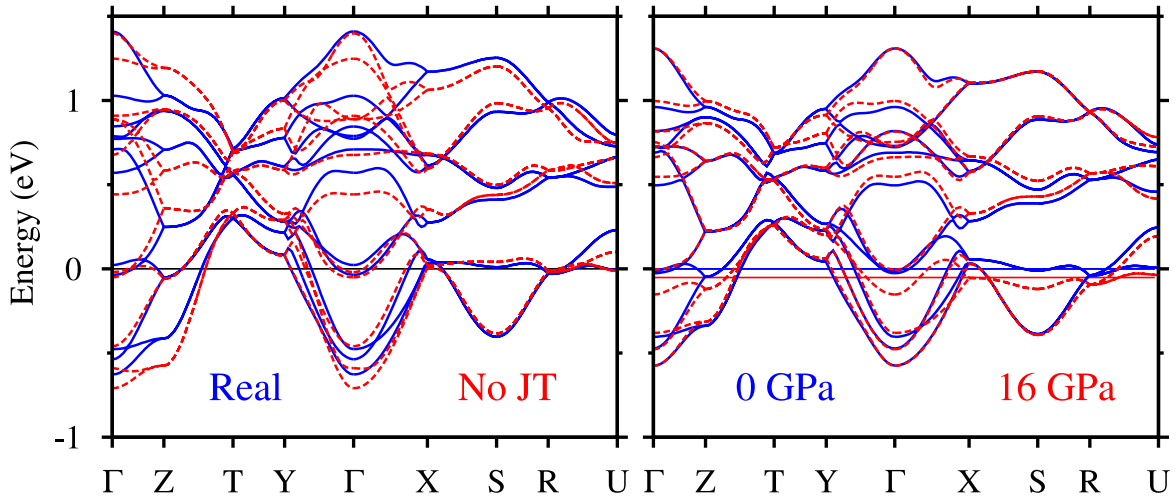

Figure 13. *Left*: $YTiO_3$ t_{2g} bands (blue) for the real structure [20] and those obtained from the hypothetical structure without JT-distortion used also for producing table 7 (dashed red). *Right*: $YTiO_3$ t_{2g} bands for the real structure at normal pressure [9] (blue) and those calculated for the structure at 16 GPa [9], where the JT-distortion has essentially disappeared. The energy axis of the high-pressure bandstructure has been scaled such as to have the bands at normal and high pressure match well. The true scale may be found in figure 12.

whereas with the recent $LaTiO_3$ data [12], results are somewhat different:

$$\begin{aligned}\begin{pmatrix} \epsilon_1 & \epsilon_2 & \epsilon_3 \end{pmatrix} &= \begin{pmatrix} 354 & 546 & 561 \end{pmatrix} \text{ meV} \\ \begin{pmatrix} |1\rangle & |2\rangle & |3\rangle \end{pmatrix} &= \begin{pmatrix} |yz\rangle & |xz\rangle & |xy\rangle \end{pmatrix} \begin{pmatrix} .735 & -.538 & .413 \\ .320 & .812 & .489 \\ .599 & .227 & -.768 \end{pmatrix},\end{aligned} \tag{19}$$

in particular for states $|2\rangle$ and $|3\rangle$. For $YTiO_3$ the eigenvalues and eigenvectors are:

$$\begin{aligned}\begin{pmatrix} \epsilon_1 & \epsilon_2 & \epsilon_3 \end{pmatrix} &= \begin{pmatrix} 289 & 488 & 620 \end{pmatrix} \text{ meV} \\ \begin{pmatrix} |1\rangle & |2\rangle & |3\rangle \end{pmatrix} &= \begin{pmatrix} |yz\rangle & |xz\rangle & |xy\rangle \end{pmatrix} \begin{pmatrix} .781 & -.571 & .253 \\ -.073 & .319 & .945 \\ .620 & .757 & -.207 \end{pmatrix}.\end{aligned} \tag{20}$$

These crystal-field splittings are much larger than the spin-orbit splitting (∼20 meV) and kT, and they agree with what was deduced (0.12-0.30 eV) from spin-polarized x-ray scattering for $LaTiO_3$ [47].

All three eigenfunctions and the two level splittings are shown in figure 14 for the titanates. The orbital of lowest energy, $|1\rangle$, is of course the one for which the electrostatic attraction and the bonding hybridization with the A ions are maximized at the same time as the electrostatic repulsion and the antibonding hybridization with the oxygens is minimized. In $LaTiO_3$, this orbital is directed towards the two La cations closest to Ti, the ones along the shortest diagonal. Also in $YTiO_3$ do the nearest cations attract

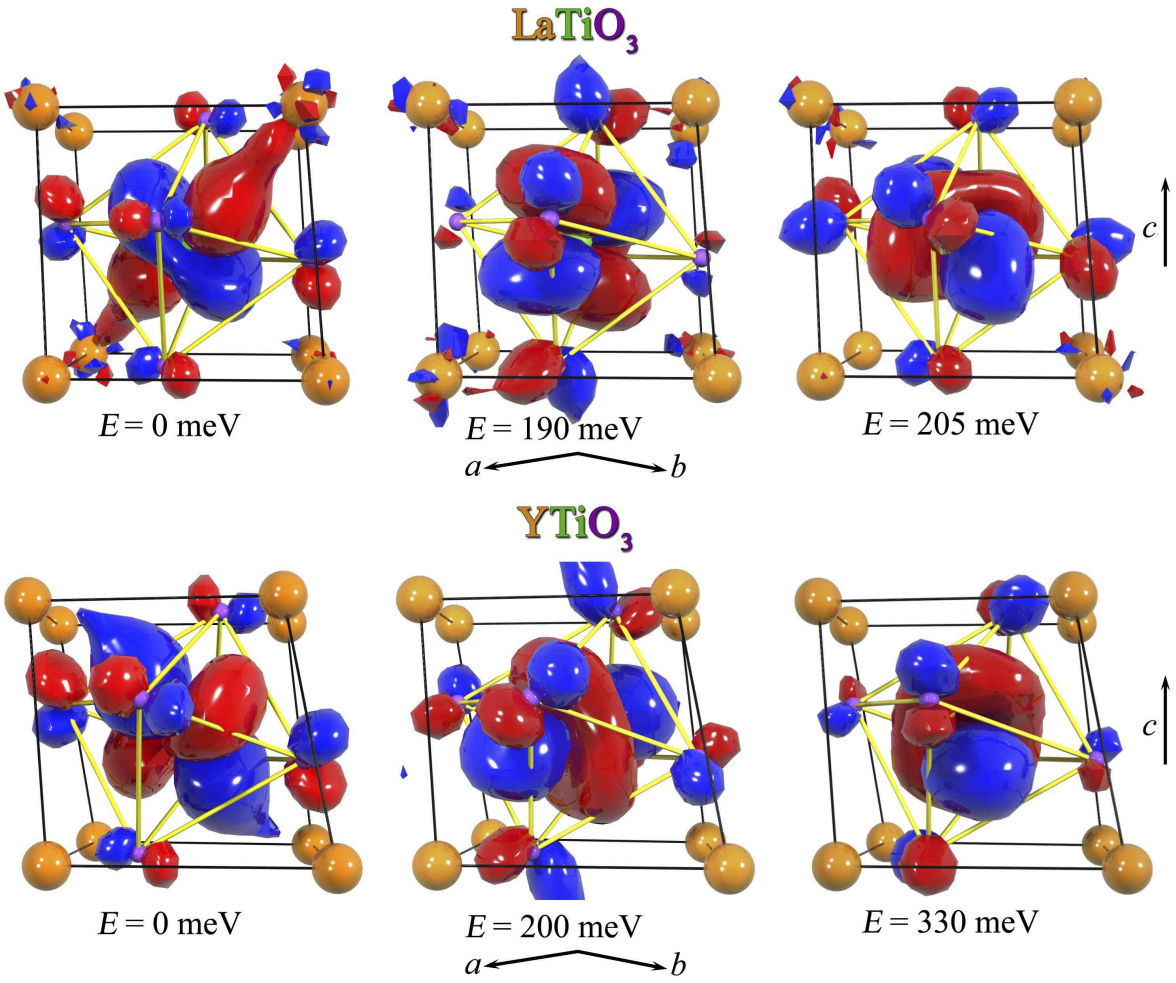

Figure 14. Ti t_{2g} crystal-field splittings and NMTO orbitals $|1\rangle$, $|2\rangle$, and $|3\rangle$ at site 000 (subcell 1) for $LaTiO_3$ [12] and $YTiO_3$ [20] obtained by diagonalization of the on-site LDA Hamiltonian in the orthonormalized t_{2g}-NMTO basis. With the older $LaTiO_3$ data [44], we get crystal-field levels of 0, 140, and 210 meV, whereas using the recent [12] 8 K data yields 0, 207, and 221 meV. For the hypothetical structure of $YTiO_3$ without JT-distortion used in table 7, the crystal field levels are 0, 136, and 259 meV. Orbital $|1\rangle$ has 97 (94) % of its charge density inside the central La_8TiO_6 (Y_8TiO_6) unit. The 3% difference is due to e_g-character on the Ti 010 neighbours in $YTiO_3$. The same contour was chosen as in figure 8. The strong e_g character on Ti 001 for orbital $|2\rangle$ in $YTiO_3$ has been cropped in this figure.

the red lobes of the lowest orbital, and for the same reasons, but in $YTiO_3$ there is also competition from the 2nd-nearest cations and, as a result, the blue lobes bond along the $[1\bar{1}1]$ diagonal with the Y $4d_{xy}$ orbitals. The details of the hybridizations were explained for the constituent yz, xy, and xz orbitals in the preceding subsection.

The difference between the lowest orbital in $LaTiO_3$ and $YTiO_3$ is brought out clearly in figure 15 where we have chosen a lower contour than in figure 14, as well as the orbital at site 010 (see also figure 16). In both materials does each red lobe *bond* to the closest-cation $d_{3z^2_{111}-1}$ orbital directed along the shortest A-B-A diagonal, and

in both materials does each blue lobe form a complex 5-centre, B – 2×O2 – A d_{xy} – O1 *bond* around the 2nd-nearest A-ion towards which the octahedron tilts. But the former mechanism prevails in La and the latter in Y titanate. The effect of A $d_{3z^2_{111}-1}$ and A d_{xy} hybridizations on the t_{2g} bandstructures were shown in figure 12. Finally, for the $YTiO_3$ orbital, we see that two oxygen p lobes which point opposite to the direction of their $GdFeO_2$-type displacement, attain bonding e_g character on their Ti neighbour. As was mentioned in subsection 3.2, this enhances the p lobe and bends it outwards. This hybridization –allowed only by the strong tilt– contributes as well to lowering the energy of orbital $|1\rangle$.

These quantitative differences in the shape of the lowest orbital in La and Y titanate are *not* caused by the small JT distortions. As an example, for $YTiO_3$ without JT distortion the on-site Hamiltonian in table 7 yields the following eigenvalues and eigenvectors:

$$\begin{aligned}\begin{pmatrix} \epsilon_1 & \epsilon_2 & \epsilon_3 \end{pmatrix} &= \begin{pmatrix} 341 & 477 & 600 \end{pmatrix} \text{ meV} \\ \begin{pmatrix} |1\rangle & |2\rangle & |3\rangle \end{pmatrix} &= \begin{pmatrix} |yz\rangle & |xz\rangle & |xy\rangle \end{pmatrix} \begin{pmatrix} .766 & -.473 & .435 \\ -.023 & .696 & .718 \\ .642 & .540 & -.544 \end{pmatrix}. \end{aligned} \tag{21}$$

For the lowest orbital, this is nearly identical with the results for the JT-distorted structure in equation (20), but it differs substantially for the higher orbitals, and that will prove important for the stability of ferromagnetic order in $YTiO_3$ (section 6). For the structure measured at 16 GPa, table 7 yields

$$\begin{aligned}\begin{pmatrix} \epsilon_1 & \epsilon_2 & \epsilon_3 \end{pmatrix} &= \begin{pmatrix} 365 & 584 & 726 \end{pmatrix} \text{ meV} \\ \begin{pmatrix} |1\rangle & |2\rangle & |3\rangle \end{pmatrix} &= \begin{pmatrix} |yz\rangle & |xz\rangle & |xy\rangle \end{pmatrix} \begin{pmatrix} .829 & -.221 & .514 \\ -.243 & .685 & .689 \\ .504 & .693 & -.514 \end{pmatrix}. \end{aligned} \tag{22}$$

Here again, the shape of the lowest orbital is nearly the same as at normal pressure, although *less* cubic and *more* $YTiO_3$'ish. This proves that the shape of the lowest orbital is determined mainly by the $GdFeO_3$-type rather than by the JT distortion.

The shape of the orbital becomes crucial when it is placed in the crystal. As seen in figure 16, the *orbital order* is very *different* in the two titanates. In $LaTiO_3$, the lowest orbital roughly has the bc plane as mirror ($x \leftrightarrow y$), and this means that the glide-mirror operation from site 1 to 2 is roughly a translation, and so are therefore all cubic translations in the xy plane. In $YTiO_3$, the lowest orbital does not have this symmetry, and the orbitals in the xy plane therefore avoid each other even more than in $LaTiO_3$. As a result, the dominating integral, $t_{11}^{100} = t_{11}^{010}$, for hopping between two lowest orbitals on nearest neighbours parallel to the mirror plane is only half as large in $YTiO_3$ (−48 meV) as in $LaTiO_3$ (−98 meV). In both cases, this hopping integral is mainly via d_{xy} character on the two A ions which are 1st-nearest neighbours to one Ti and 2nd-nearest neighbours to the other. But whereas both large hopping integrals, $t_{yz,yz}^{010}$ and $t_{xy,xy}^{010}$, contribute in $LaTiO_3$, only the latter does so in $YTiO_3$. This may be

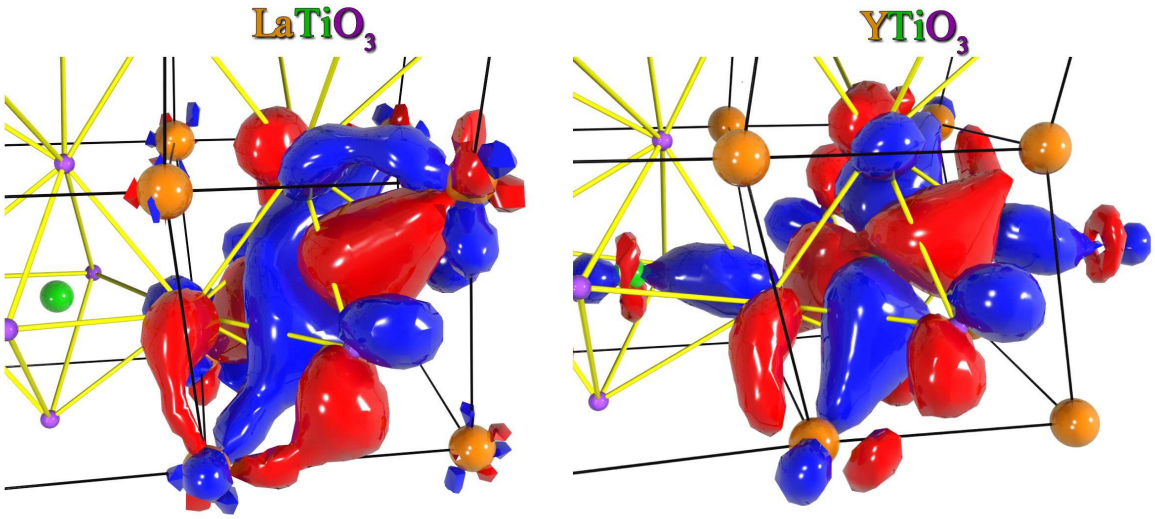

Figure 15. Crystal-field orbital with the lowest energy, $|1\rangle$, at site 010 (subcell 2). A contour value 2/3 of the one used in the previous figures was chosen in order to exhibit the hybridization with the O p and A $d_{3z^2_{111}-1}$ and d_{xy} states. In $LaTiO_3$, the hybridization with $d_{3z^2_{111}-1}$ on the two 1st-nearest A ions dominates over the hybridization with d_{xy} on the two 2nd-nearest A-ions towards which the octahedron tilts. In $YTiO_3$, the opposite is true. For the heavily distorted $YTiO_3$, there is also bonding from O2 p to e_g on two Ti-neighbours. The A $d_{3z^2_{111}-1}$ and d_{xy} hybridizations of the t_{2g} bands were shown in figure 12.

seen in detail from the matrix transformation (23) and (24) given below. Both for La and Y titanate, there is only little O2-mediated hopping because the p character of one orbital hardly couples to the other orbital.

The 1st-nearest-neighbour hopping in the z direction, t_{11}^{001}, is antibonding (105 meV) in $LaTiO_3$, with the sign-convention dictated by the mirror plane, and it is mainly via oxygen p. In fact, since according to the transformation (19), orbital $|1\rangle$ in $LaTiO_3$ is mainly composed of $|yz\rangle$ and $|xy\rangle$, and since the latter hardly couples in the z direction, $t_{11}^{001} \sim -0.5t_{yz,yz}^{001}$ and $t_{yz,yz}^{001} = -193$ meV, as was discussed in connection with equation (5). In $YTiO_3$, orbital $|1\rangle$ is almost exclusively composed of $|yz\rangle$ and $|xy\rangle$, so that here we should have: $t_{11}^{001} \sim -0.6t_{yz,yz}^{001}$. With $t_{yz,yz}^{001}$ anomalously small (-65 meV) due to coupling via Y $4d_{xy}$, t_{11}^{001} becomes not only anomalously small, but even bonding (-38 meV) because now the small coupling (± 64 meV) between $|yz\rangle$ and $|xy\rangle$ in the z direction cannot be neglected. This can be followed explicitly in equations (25) and (26) given below.

Hence for the lowest crystal-field orbital the paths for hopping between nearest Ti neighbours in the xy plane are very different from those for hopping along z. Since exchange couplings are proportional to hopping integrals *squared* in conventional super-exchange theory, and since the spin-wave spectra in antiferromagnetic La as well as in

ferromagnetic Y titanate were both measured to be isotropic, this could be taken as an argument against the applicability of conventional theory for the low-temperature properties of these systems [40]. We shall return to this in section 6.

Hopping integrals squared are very sensitive quantities, and since the residual cation covalencies in the materials with large $GdFeO_3$-type distortions have completely ruined the cubic symmetry of the LDA t_{2g} Hamiltonians, let us explicitly perform the transformation of the dominating t_π hopping integrals, t^{010}, t^{100}, and t^{001}, from the cubic to the crystal-field representation in $LaTiO_3$ and $YTiO_3$. We start from the cubic representation in tables 4 and 5, and use the transformation valid for site 000 given by equations (19) and (20). When transforming the hopping integrals, we should remember that in the cubic representation (middle row in figure 8) those t_{2g} orbitals which would couple strongly if the crystal were cubic, carry the same name in all four subcells, whereas in the crystal-field representation, the orbitals are named and have signs following the space-group symmetry, that is, the bottom row in figure 8 and in figure 16.

The t^{010} matrix for hopping between crystal-field orbitals $|1\rangle$, $|2\rangle$, and $|3\rangle$ at sites 000 and 010, which are related by the glide mirror $(x \leftrightarrow y)$, is for $LaTiO_3$:

$$\begin{pmatrix} .735 & .320 & .599 \\ -.538 & .812 & .227 \\ .413 & .489 & -.768 \end{pmatrix} \begin{pmatrix} -185 & 75 & -34 \\ -43 & 1 & 73 \\ -54 & -33 & -183 \end{pmatrix} \begin{pmatrix} .320 & .812 & .489 \\ .735 & -.538 & .413 \\ .599 & .227 & -.768 \end{pmatrix} \text{meV}$$
$$= \begin{pmatrix} -98 & -192 & 12 \\ 4 & 76 & -22 \\ 120 & -40 & -128 \end{pmatrix} \text{meV}, \tag{23}$$

with the order of rows and columns being like in equations (17)–(22), *i.e.*: yz, xz, xy for the cubic and 1, 2, 3 for the crystal-field representation. In the cubic representation, the elements along the diagonal of the hopping matrix are the well-known t_π, t_δ, t_π. It may be realized that the hopping integrals, $t^{010}_{mm'}$, resulting from this transformation are sums of contributions with varying signs. For $YTiO_3$:

$$\begin{pmatrix} .781 & -.073 & .620 \\ -.571 & .319 & .757 \\ .253 & .945 & -.207 \end{pmatrix} \begin{pmatrix} -184 & 70 & -54 \\ -41 & 28 & 65 \\ -64 & -22 & -162 \end{pmatrix} \begin{pmatrix} -.073 & .319 & .945 \\ .781 & -.571 & .253 \\ .620 & .757 & -.207 \end{pmatrix} \text{meV}$$
$$= \begin{pmatrix} -48 & -191 & -130 \\ -84 & -13 & 44 \\ 94 & 11 & -73 \end{pmatrix} \text{meV}. \tag{24}$$

Note that at the second site 010, we must exchange the yz and xz orbitals. For the t^{100} matrix of hopping integrals between the orbitals at sites 000 and site $100 = 010 + \mathbf{a}$ the transformation is the same, and we simply get:

$$t^{100}_{mm'} = t^{010}_{m'm}.$$

For these hoppings parallel to the mirror plane, the differences between La and Y-titanate are rooted more in the different crystal-field eigenvectors than in the different

hoppings between the yz, xz, and xy orbitals.

The t^{001} matrix for hopping between crystal-field orbitals $|1\rangle$, $|2\rangle$, and $|3\rangle$ at sites 000 and 001, which are related by the A-O1 mirror plane perpendicular to the z axis ($z \to -z$), is for $LaTiO_3$:

$$\begin{pmatrix} .735 & .320 & .599 \\ -.538 & .812 & .227 \\ .413 & .489 & -.768 \end{pmatrix} \begin{pmatrix} -193 & -42 & -59 \\ -42 & -208 & 52 \\ 59 & -52 & -22 \end{pmatrix} \begin{pmatrix} -.735 & .538 & -.413 \\ -.320 & -.812 & -.489 \\ .599 & .227 & -.768 \end{pmatrix} \text{meV}$$
$$= \begin{pmatrix} 105 & 31 & 143 \\ 31 & 188 & -10 \\ 143 & -10 & 85 \end{pmatrix} \text{meV}, \tag{25}$$

and for $YTiO_3$ it is:

$$\begin{pmatrix} .781 & -.073 & .620 \\ -.571 & .319 & .757 \\ .253 & .945 & -.207 \end{pmatrix} \begin{pmatrix} -65 & -63 & -64 \\ -63 & -178 & 83 \\ 64 & -83 & -8 \end{pmatrix} \begin{pmatrix} -.781 & .571 & -.253 \\ .073 & -.319 & -.945 \\ .620 & .757 & -.207 \end{pmatrix} \text{meV}$$
$$= \begin{pmatrix} -38 & -21 & 97 \\ -21 & 107 & 51 \\ 97 & 51 & 167 \end{pmatrix} \text{meV}. \tag{26}$$

Here we must flip the sign of the yz and xz orbitals at site 001. In case of hopping perpendicular to the mirror plane, not only the different crystal-field eigenvectors matter, but also the large non-cubic perturbations of the hopping integrals in $YTiO_3$.

In the cubic representation, the matrices of 1st-nearest-neighbour hopping integrals have two large diagonal elements, t_π, and all other (inter-orbital) elements are small, except in $YTiO_3$, where $t^{001}_{yz,yz} = -65$ meV is anomalously small and the inter-orbital elements are of similar size. In the crystal-field representation, the matrices of 1st-nearest-neighbour hopping integrals do not have this form at all. In particular in $YTiO_3$, the hopping between orbitals $|1\rangle$ is anomalously small and, except in one case, smaller than the hopping from orbital $|1\rangle$ to orbitals $|2\rangle$ and $|3\rangle$. As we shall see in section 6, this is what makes $YTiO_3$ ferromagnetic at low temparature.

In the crystal-field representation, we do *not* mirror the orbitals like in equation (4) in order to obtain the values of integrals corresponding to hops starting from another site than the first. Here the rules are simply:

$$t^{(0,0,1),(x,y,z+1)}_{m',m} = t^{xy\bar{z}}_{m',m} \qquad t^{(0,1,1),(x,y+1,z+1)}_{m',m} = t^{yx\bar{z}}_{m',m}$$

$$t^{(0,0,0),(x,y,z)}_{m',m} \equiv t^{xyz}_{m',m} \qquad t^{(0,1,0),(x,y+1,z)}_{m',m} = t^{yxz}_{m',m}$$

In figure 17 we show the bandstructures decorated with B t_{2g} partial-wave characters in the cubic and the crystal-field representations at site 000 or, equivalently, according to the *bottom* row of figure 8 (see also figure 16). In general, the mixing of characters is considerable in both representations, although the crystal-field splittings – which are small on the scale of the bandwidth – do cause a slight preference for lower-lying bands

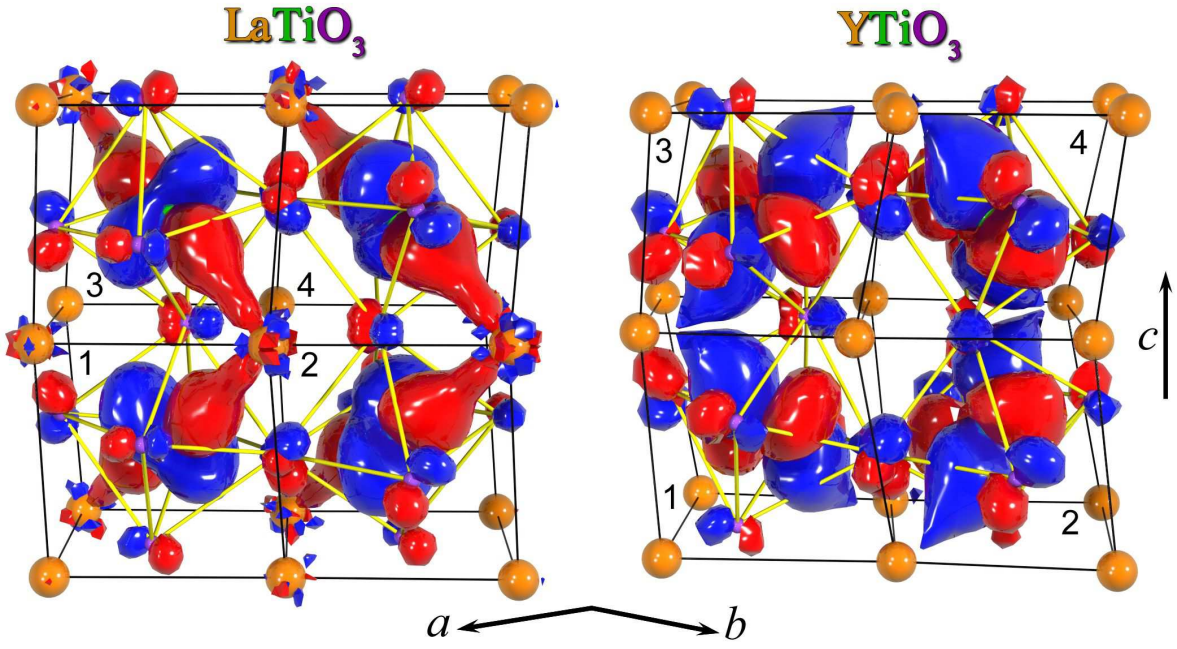

Figure 16. Orbital of the lowest energy, $|1\rangle$, placed in the 4 subcells (1=000, 2=010, 3=001, and 4=011) according to the mirror and glide-mirror symmetries, *i.e.* like in the bottom row of figure 8. This illustrates the orbital order which will crystalize out due to the Coulomb correlations (see subsection 5.3).

to have stronger $|1\rangle$ character (red) and higher-lying bands to have stronger $|3\rangle$ character (blue). Nevertheless, there *are* two important cases of character separation: the bands at the lower edge of the pseudo-gap, which move down and get increasingly occupied as we proceed along the series, have strong $|1\rangle$ character, and the 4th band near Γ_o, which moves upwards and almost empties, has strong $|3\rangle$ character. As we have seen in figures 12 and 15, the $|1\rangle$ bands are those with strong A $d_{3z^2_{111}-1}$ and A d_{xy} characters. The dominant role of those bands in the development of the pseudo-gap is also evident from the top right and the bottom row parts of figure 18, exhibiting the on-site 000 elements,

$$N_{mm'}\left(\varepsilon\right) \equiv \sum_{i\mathbf{k}} u_{\mathbf{R}m,i}\left(\mathbf{k}\right)\, \delta\left[\varepsilon - \varepsilon_i\left(\mathbf{k}\right)\right]\, u^*_{\mathbf{R}m',i}\left(\mathbf{k}\right),$$

of the density-of-states (DOS) matrix. Here, $\mathbf{u}_i\left(\mathbf{k}\right)$ is an eigenvector of the LDA Hamiltonian (7) in a t_{2g} Wannier-function basis.

4. Multi-band Hubbard Hamiltonian and its solution in the dynamical mean-field approximation

Having discussed at length the one-electron, "chemical" part of the Hamiltonian, $H^{LDA}_{t_{2g}}$, we now add the on-site Coulomb repulsion and obtain the multi-band Hubbard Hamiltonian:

$$\mathcal{H}_{t_{2g}} = \mathcal{H}^{LDA}_{t_{2g}} + \sum\nolimits_R \mathcal{U}_R \ . \tag{27}$$

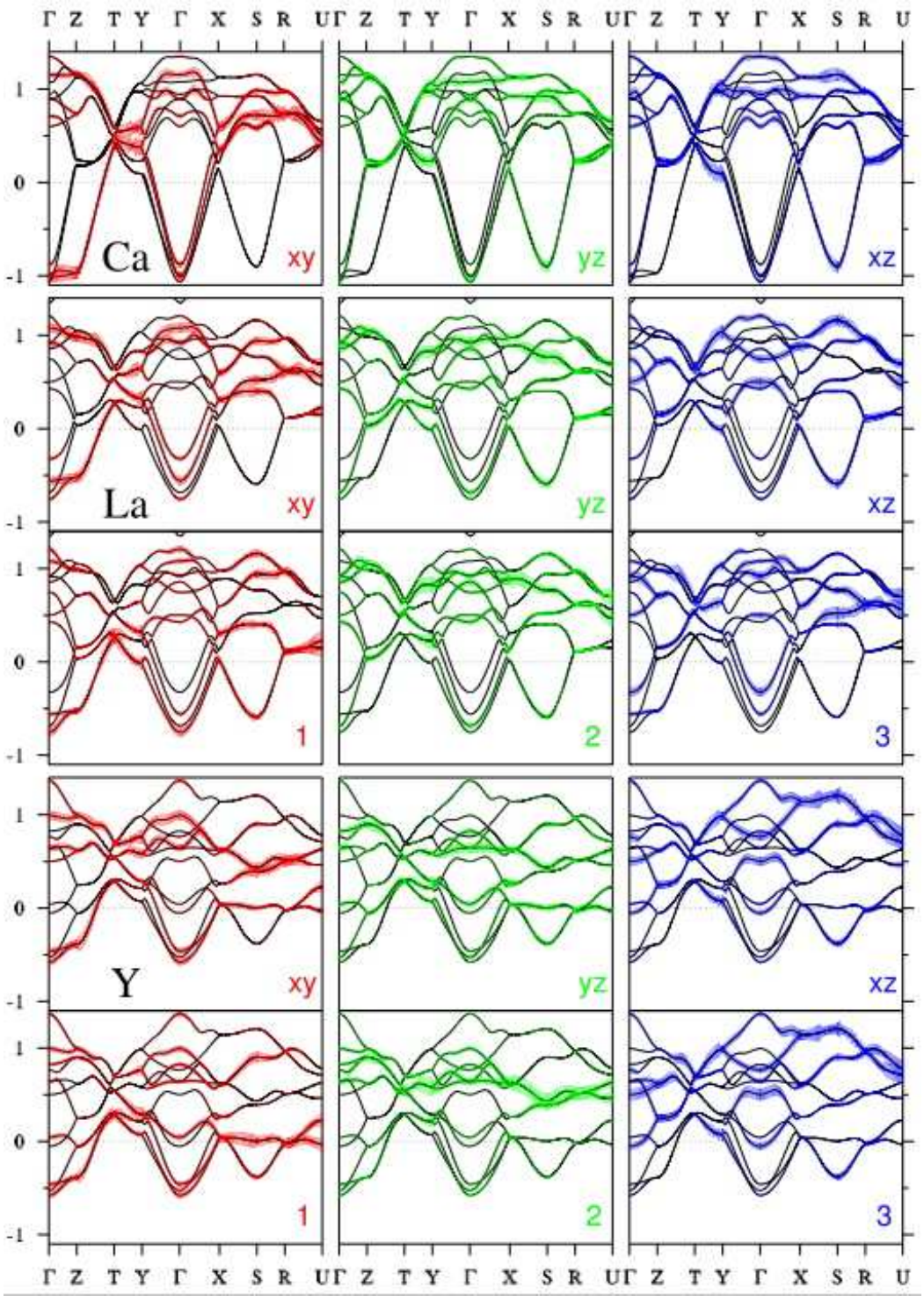

Figure 17. LDA LMTO bandstructures of the orthorhombic perovskites decorated with B partial-wave characters at site 000 in the cubic and the crystal-field representations, or equivalently, according to the *bottom* row of figure 8 and figure 16. For $CaVO_3$ $|1\rangle \approx |xy\rangle$, $|2\rangle \approx |xz\rangle$, and $|3\rangle \approx |yz\rangle$. The points of high symmetry are those mentioned explicitly in the caption to figure 9, and not any of their equivalents.

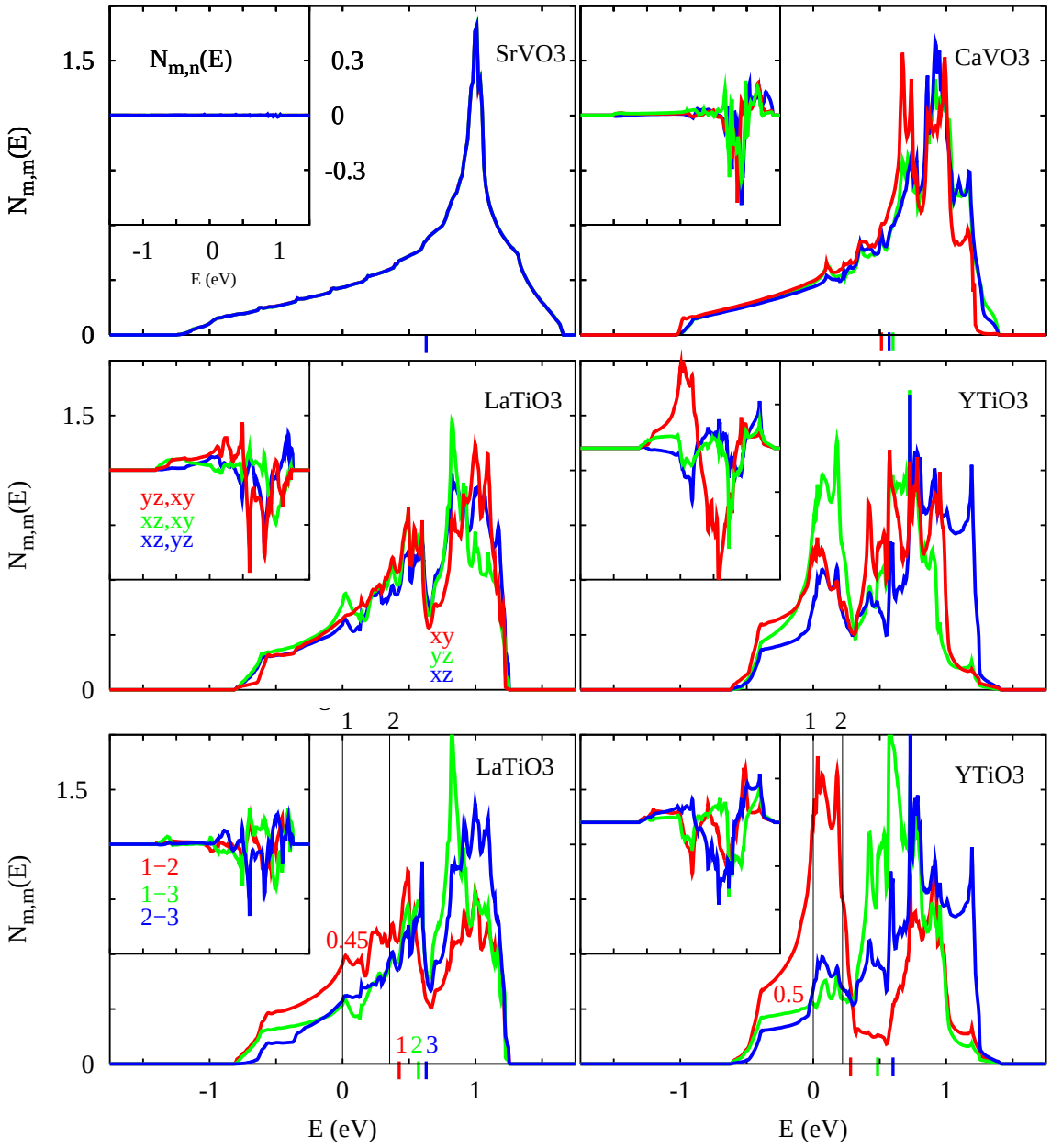

Figure 18. The LDA on-site DOS matrices $N_{mm'}(\varepsilon)$ for site 000 (subcell 1) in the representation of the t_{2g} Wannier functions. The zero of energy is the Fermi level. The DOS unit is states/(eV·spin·ABO_3). The insets show the off-diagonal elements on a reduced energy scale, but the same DOS scale. *Top two rows:* cubic basis as defined in the bottom row of figure 8. *Bottom row:* crystal-field basis as defined in figure 14 and equations (17)–(20). The tick marks indicate the positions of the t_{2g} crystal-field levels. The occupancy of the lowest crystal-field orbital is 0.45 in $LaTiO_3$ and 0.50 in $YTiO_3$. The Fermi levels for occupations with one and two electrons are marked; the latter is the majority-spin Fermi level for a d^1 ferromagnet in the Stoner model. The older data [44] was used for $LaTiO_3$.

Here, $\mathcal{U}$ is such that for a doubly occupied site $\left(t_{2g}^2\right)$, its 15 degenerate states are as follows: a 9-fold degenerate triplet with energy $U-3J$, a 5-fold degenerate singlet with energy $U-J$, and a singlet with energy $U+2J$. For the analogous p^2-configuration these states would be ^3P, ^1D, and ^1S, respectively. The average d^2 energy is

$$U-2J \equiv U'. \tag{28}$$

U is the Coulomb repulsion between two electrons in the same orbital, and J is the Hund's-rule exchange coupling.

Since $\mathcal{H}_{t_{2g}}$ involves only the correlated t_{2g} orbitals, the number of correlated electrons is fixed and the double-counting correction therefore amounts to an irrelevant shift of the chemical potential, which we omit in (27). For transitions from or to a non-correlated LDA band, such as those seen in figures 1, 3, and 4, there *is* a double-counting correction, but it is presumably $\lesssim 1$ eV, because the number of B t_{2g} electrons in the LDA calculation is not far from 1. In those figures, the LDA t_{2g} band should therefore simply be substituted by the correlated t_{2g} band with the Fermi levels lined up.

In general, an LDA+U Hamiltonian like (27) depends on which electronic degrees of freedom, *i.e.* orbitals, are included, and how the correlated orbitals are chosen. This means that in order to be able to treat electronic correlations beyond the LDA, we have to depart from the *ab initio* philosophy and make a system- and even property-dependent choice of an appropriate low-energy Hubbard Hamiltonian. In the present work for the d^1 perovskites, the correlated orbitals are taken as the set of localized t_{2g} LDA Wannier functions. The degrees of freedom from all other bands are neglected, not only in the correlation term, but also in $\mathcal{H}^{LDA}$. For instance, the B e_g band, whose centre is 3 eV above that of the t_{2g} band (see figures 3 and 4), is not treated as correlated, but the e_g characters are downfolded into the t_{2g} orbitals as seen in figures 14 and 15. For the Mott transition, this seems to be the appropriate treatment, as is also suggested by the work of Manini *et al.* [15]. For super-exchange couplings this also seems to hold, as we shall argue in section 6, but for high-energy optical or inverse-photoemission spectra, it is clearly inappropriate. Here, e_g degrees of freedom must be taken explicitly into account in the Hubbard Hamiltonian. This can be done by using as basis either the present t_{2g} basis augmented by the Wannier functions for the LDA e_g band, or the set of Wannier functions for the entire $d\,(t_{2g}+e_g)$ band. The advantage of the former basis set is that it has *no* single-particle coupling between the t_{2g} and e_g bands, and the advantage of the latter is that it is more localized. Anyhow, in the present work we do not compute high-energy properties.

In principle, the on-site Coulomb matrix should be calculated from the Wannier-function basis used, but in the present case it was simpler to keep a single, adjustable parameter, U, and – as we shall see – this yields more insight. The value of this parameter we took to be the *same* for all four materials. For the Hund's-rule coupling we used the following:

$$J = 0.68 \text{ eV} \qquad \text{and} \qquad 0.64 \text{ eV},$$

for the vanadates and titanates, respectively. These are atomic Hartree-Fock values times 0.8 in order to account for the screening in the solid [25].

The Hubbard Hamiltonian (27) is solved in the DMFT [35], *i.e.* under the assumption that the elements, $\Sigma_{Rm,R'm'}(\omega)$, of the self-energy matrix *between* different sites can be neglected. The self-energy is thus assumed to be an effective, energy-dependent and complex crystal-field term. In this case, the on-site Green matrix is:

$$G_{Rm,Rm'}(\omega) = \sum_{\mathbf{k}} \left\{ \left[\omega - \Sigma(\omega) - H^{LDA}(\mathbf{k}) \right]^{-1} \right\}_{Rm,Rm'}, \tag{29}$$

and the many-body lattice problem is then mapped onto an Anderson impurity problem in which the inverse of the bath Green function of the uncorrelated host is required to be $G(\omega)^{-1} + \Sigma(\omega)$. Solution of the Anderson impurity problem must now yield the same $G_{Rm,Rm'}(\omega)$ as equation (29), and this is a self-consistency condition for determination of the self-energy matrix, $\Sigma_{Rm,Rm'}(\omega)$, and the host.

The bottleneck in a DMFT calculation is to solve the Anderson impurity problem, and only a few correlated orbitals can be handled at the moment. In the orthorhombic perovskites all 4 B-sites are *equivalent*, so the t_{2g} impurity problem involves only 3 correlated orbitals. To solve it, we employed the numerically exact Hirsch-Fye [48] quantum Monte Carlo (QMC) method. In order to access temperatures down to 770 K, we used up to 100 slices in imaginary time and about 10^6 QMC sweeps. To reach convergence, 15–20 DMFT iterations were needed. Finally, the spectral function was obtained on the real ω-axis by analytical continuation using the maximum entropy method [49]. Unfortunately, this does not provide us with the self-energy matrix for real ω, so we do not obtain correlated bandstructures in the present applications.

In order to be able to perform the DMFT calculations we adopted the usual approximation of keeping only the density-density terms in the on-site Coulomb-repulsion, *i.e.*

$$\mathcal{U}_R \approx \frac{1}{2} \sum_{mm'\sigma\sigma'} U_{m\sigma,m'\sigma'} n_{Rm\sigma} n_{Rm'\sigma'}, \quad U_{m\sigma,m'\sigma'} = \begin{cases} U & \text{if } m = m' \text{ and } \sigma \neq \sigma' \\ U - 2J & \text{if } m \neq m' \text{ and } \sigma \neq \sigma' \\ U - 3J & \text{if } m \neq m' \text{ and } \sigma = \sigma' \end{cases}.$$

Here, $n_{Rm\sigma} = a^\dagger_{Rm\sigma} a_{Rm\sigma}$, and $a^\dagger_{Rm\sigma}$ creates an electron with spin σ in a localized orbital m at B-site R. In the summation, at least two of the indices on the operators must be different. The repulsion averaged over all doubly occupied states remains as in equation (28) [50].

In previous implementations of the LDA+DMFT method [36, 37] it was assumed that the on-site block of the single-particle Green function is diagonal with identical elements in the space of the correlated orbitals, and the latter were usually taken as orthonormal LMTOs [41], approximated by truncated and renormalized partial waves. These approximations mean that the partial waves *not* belonging to the irreducible representation of the correlated LMTOs –and therefore arising from the tails of LMTOs on neighbouring sites– are neglected. As a consequence, the self-energy in equation (29) merely distorts the energy scale of the LDA DOS, from which the on-site $G(\varepsilon)$

can then be obtained by Hilbert transformation. Although this may be appropriate for *e.g.* cubic systems, it is clearly *not* appropriate for the series of materials considered in the present paper. Here, the self-energy must be allowed to be an effective crystal field – enhanced, energy dependent, and complex through the influence of $\mathcal{U}_R$ – which produces **k**-dependent broadenings and distortions of the bandstructure of the kind we have been discussing extensively in section 3.6. Specifically, in table 9 we should perform the substitutions:

$$t^{000}_{x_i x_j, x_j x_k} \rightarrow t^{000}_{x_i x_j, x_j x_k} + \Sigma_{x_i x_j, x_j x_k}(\omega) \tag{30}$$

It is *not* correct to merely distort the energy scales of the different partial DOS functions differently.

In our new implementation [21] of the LDA+DMFT method, the highly accurate NMTO method is used to create a localized set of correlated orbitals, which then defines the Hubbard Hamiltonian. We choose the localized orbitals to span a subset of LDA bands around the Fermi level *exactly* –the t_{2g} bands in the present application,– and we choose to orthonormalize them symmetrically so that they become a set of Wannier functions. With this set, the matrix elements are then calculated correctly (except the matrix elements of the on-site Coulomb repulsion). Hence, we take all components of the self-energy matrix $\Sigma_{mm'}(\omega)$ between different orbitals on a given site into account. From this 3×3 matrix we use the *Pbnm* symmetry (figure 2) to construct a 12×12 block-diagonal self-energy matrix, which is then inserted in expression (29). The 12×12 matrix $\omega - \Sigma(\omega) - H^{LDA}(\mathbf{k})$ is now inverted as a function of **k**, and, finally, the on-site 3×3 block is summed over **k** to yield the 3×3 on-site $G(\varepsilon)$ matrix.

A recent LDA+DMFT calculation for $La_{1-x}Sr_xTiO_3$ [39] used the crystal-field representation and neglected the off-diagonal elements of the DOS and the self-energy. As seen in the bottom row of figure 18, this may be an intelligible approximation. Nevertheless, even with the crystal-field eigenvectors frozen at the LDA values, the $\Sigma(\omega) + H^{LDA}(\mathbf{k})$ bandstructure should be allowed to change as the effective crystal-field splittings change from iteration to iteration.

Another LDA+DMFT implementation based on Wannier functions was proposed after the completion of the present work [51]. Applications to cubic $SrVO_3$ using t_{2g} Wannier functions yielded low-energy spectral functions similar to those presented in the next section. It is not obvious to us how t_{2g} Wannier functions can provide matrix elements of the self-energy connecting to other bands, except for the trivial double-counting shifts mentioned above. A good idea in that paper is to use the on-site Green function (29) to evaluate the contribution to the charge density from the correlated orbitals and, hence, to adjust the Wannier functions self-consistently, away from their LDA values. For the t^1_{2g} titanates, a useful application would be to calculate the JT distortions from the LDA+DMFT charge density.

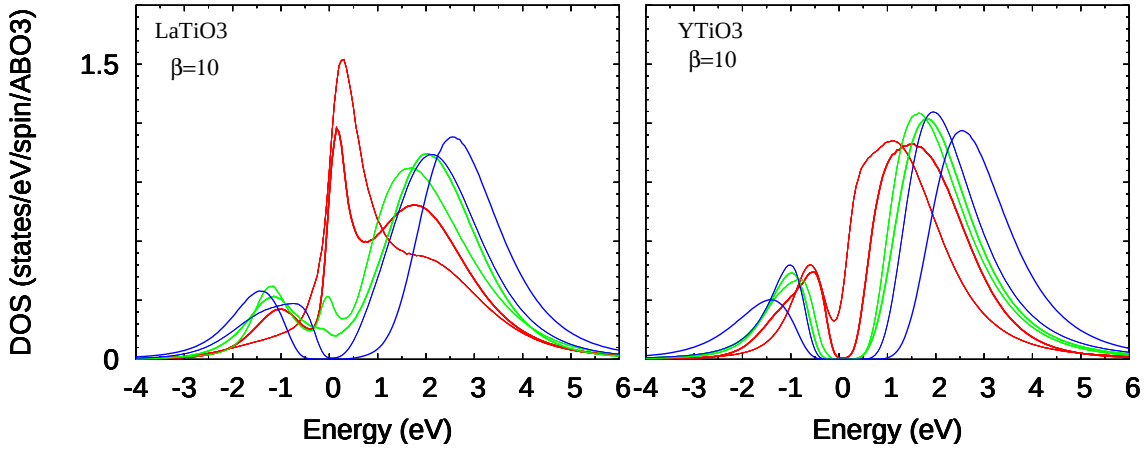

Figure 19. DMFT spectral function for U=3.5 (red), 4.0 (bold red), 4.5 (green), 4.75 (bold green), 5.0 (blue), and 6.0 (bold blue) eV. The average Coulomb repulsion is U'=U − 1.28 eV. kT= 100 meV∼1200 K. For $LaTiO_3$, the older structural data were used [44]. Extensive DMFT calculations were not performed with the recent data [12].

5. High-temperature properties

5.1. The Mott transition

With LDA+DMFT we computed the spectral functions for all four materials as a function of U and at kT=100 meV∼1200 K, *i.e.* way above any magnetic ordering temperature. We do not investigate the complete phase diagram or the order of the Mott transition; rather, we estimate the critical value, U_c, for the high-temperature region where the system is paramagnetic and for which we find a unique solution of the DMFT equations.

For the titanates, the spectra are shown in figure 19. We found that the materials become insulating when $U' \geq U'_c$ with the values of U'_c given in the first row of table 10. Cubic $SrVO_3$ remained metallic at the highest value of U' considered (4.6 eV), and the calculation employed the older structural data [44] for $LaTiO_3$. The decrease of the critical value seen along the series is dramatic, and if we form the ratio with the rms bandwidth W from table 8, we find the numbers given in the central row of table 10. This ratio is *not* constant, but decreases along the series by 35% from $CaVO_3$ to $YTiO_3$. Therefore, the Mott transition is *not* driven merely by the narrowing of the t_{2g} band, but also by its deformation. That is unexpected.

The importance of orbital degeneracy for the Mott transition was first pointed out by Gunnarsson *et al.* [14], who argued that due to the increase in the number of hopping processes in many-body theory compared with band theory, there is an enhancement of the hopping, which for a half-full band is approximately proportional to the square root of its degeneracy. The value, U'_c, necessary to cause a Mott transition for a given bare bandwidth, W, therefore increases with the degeneracy.

Table 10. Critical Coulomb repulsion, U_c', in eV and relatively to the rms bandwidth, W. The crystal-field splitting between the lowest levels is Δ_{12}.

	$SrVO_3$[42]	$CaVO_3$[43]	$LaTiO_3$[44]	$LaTiO_3$([12])	$YTiO_3$[20]
U_c'	> 4.6	4.4	3.6	–	2.5
U_c'/W	(1.96)	1.84	1.65	–	1.34
Δ_{12}/W	0	0.031	0.064	0.093	0.106

Imagine now with Manini *et al.* [15] that this degeneracy is split by a small crystal field: upon increasing U', and thereby reducing the width of the quasiparticle peak towards zero, $ZW \sim \alpha\left[1 - U'/U_c'(N)\right]W$, for some value of $U' < U_c'(N)$ the reduced bandwidth will have reached the same size as the crystal-field splitting. At that point the degeneracy is effectively decreased from N to $N - n$, and herewith U_c', so that a Mott transition may be triggered. One therefore expects a critical crystal-field splitting, $\Delta_c \sim \alpha\left[1 - U_c'(N-n)/U_c'(N)\right]W$. Manini *et al.* specifically solved a simple Hubbard model with one electron in two identical, non-interacting bands whose on-site energies differed by Δ For $\Delta = 0$, they found $U_c'(2)/W \sim 1.8$, and for $\Delta \to \infty$, they found $U_c'(1)/W \sim 1.35$, so that $U_c'(2)/U_c'(1) \sim 1.33$. The surprising result was that U_c'/W decreases from the $\frac{1}{4}$-filled two-band limit to the $\frac{1}{2}$-filled one-band limit for Δ increasing from 0 to merely 10% of the bandwidth, *i.e.* $\Delta_c/W \sim 0.1$, so that $\alpha \sim 0.1/(1 - 1.35/1.8) \approx 0.4$. The crystal field splitting does, however, only control U_c'/W for the Mott transition within the limits from $U_c'(2)/W$ to $U_c'(1)/W$; if for $\Delta > \Delta_c$, U'/W is increased from below 1.35, then the system undergoes a phase transition from a two-band metal to a one-band metal before it goes from a one-band metal to a one-band Mott insulator at $U_c'/W = 1.35$.

For our case of a $\frac{1}{6}$-filled three-band system, Koch *et al.* [52] solved a Hubbard model for the t_{1u}-band in C_{60} and found that hopping is enhanced by merely $\sim \left(1 + \sqrt{2}\right)/2 = 1.21$. Thus, the degeneracy reduction expected from the crystal-field splitting is at most 30%. The striking fact about our values of U_c'/W is that they decrease by considerably more: if we use Manini *et al.*'s α-value, then the 3% crystal-field splitting in $CaVO_3$ has reduced U_c'/W by about 6% from $U_c'(3)/W$, the value appropriate for $SrVO_3$ and listed in parentheses in table 10. Our LDA+DMFT calculations thus yield a decrease in U_c'/W of ∼50% when going from cubic $SrVO_3$ to $YTiO_3$. That is not possible unless the width of the lowest subband narrows more than the rms bandwidth, that is, unless the band deforms along the series, an effect not considered previously. We shall return to this point in section 7.

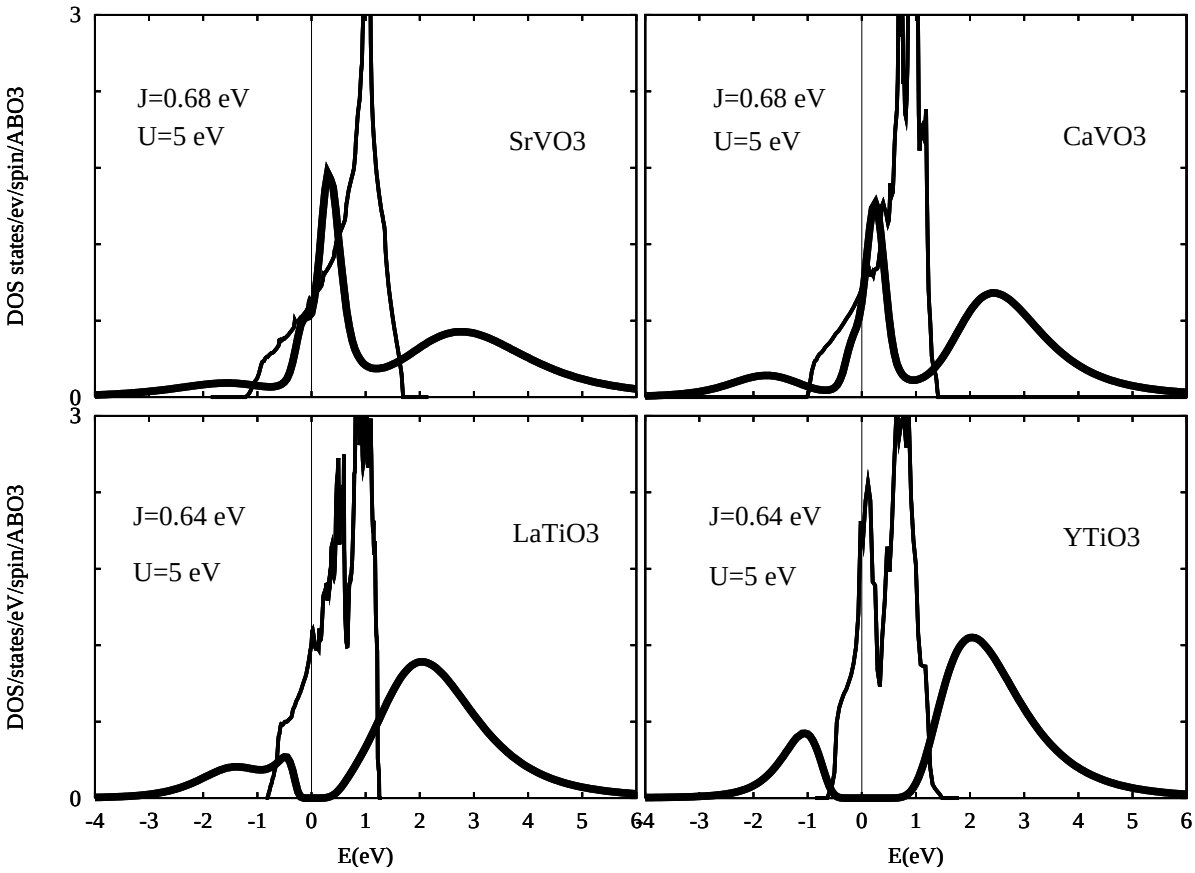

Figure 20. DMFT spectral functions for U=5 eV and T=770 K (bold) and LDA total density of states (weak). For $LaTiO_3$, the old structure was used. Reproduced from [21].

5.2. Spectral functions for U=5 eV and comparison with experiments

The main features of the photoemission spectra for all four materials, as well as the correct values of the Mott-Hubbard gap for the insulators, are reproduced by taking U material independent and equal to 5 eV. This is satisfying because U is expected to be similar for vanadates and titanates, or maybe slightly smaller for the latter [25, 53]: Bocquet *et al.* fitted $2p$ core-level photoemission spectra with a model Hamiltonian containing all O p and B d orbitals and obtained $U' \approx 4.0$ eV for La and Y titanate [54]. This is consistent with the value $U' = 5.0 - 2 \times 0.64 = 3.7$ eV used by us for the less localized t_{2g} orbitals. Similar values of U' have been used by other authors [38, 51]

In Figure 20 we show the spectral functions together with the total LDA DOS. The vanadates exhibit a quasiparticle peak and are therefore metallic, while the titanates are Mott insulators.

For cubic $SrVO_3$ we reproduce the results of previous calculations [38, 55]: the lower Hubbard band is around -1.8 eV and the upper Hubbard band around 3 eV. For $CaVO_3$, the quasiparticle peak loses weight to the lower Hubbard band, which remains at -1.8 eV, while the upper band moves down to 2.5 eV. These results are in very good

agreement with photoemission data [38, 56]. From the linear regime of the self-energy at small Matsubara frequencies we estimate the quasi-particle weight to be $Z = 0.45$ for $SrVO_3$ and 0.29 for $CaVO_3$. For a $\mathbf{k}$ independent self-energy, as assumed in DMFT, this yields $m^*/m = 1/Z = 2.2$ for $SrVO_3$ and 3.5 for $CaVO_3$. These results are in good agreement with the optical-conductivity values of 2.7 and 3.6 [4], as well as with the values 2-3 obtained by thermodynamics [5, 6] and dHvA experiments [46]; they show that $SrVO_3$ and $CaVO_3$ are rather similar, with the latter slightly more correlated than the former. Similar conclusions were drawn in [38].

For the titanates, the lower Hubbard band is around $-1.5\,\mathrm{eV}$, in accord with photoemission [54, 53]. Despite very similar bandwidths, the gaps are very different, approximately 0.3 eV for $LaTiO_3$ and approximately $1\,\mathrm{eV}$ for $YTiO_3$, and this also appears to agree with optical experiments [7].

5.3. Orbital polarization

Diagonalization of the matrix of occupation numbers,

$$n_{x_i x_j, x_j x_k} = \frac{1}{\pi}\mathrm{Im}\int^{\mu} d\omega G_{Rx_i x_j, Rx_j x_k}(\omega),$$

obtained with LDA+DMFT for values of U' exceeding the t_{2g} bandwidth, W, reveals that – within the numerical accuracy – the *eigenvectors,* $w_{x_i x_j, m}$, are the *same* as those which diagonalize the on-site LDA Hamiltonian matrix, that is, n and $t^{\mathbf{0}}$ commute. For the titanates, the eigenvectors are the ones given by equations (18), (19), and (20), and the corresponding eigenfunctions are the crystal-field orbitals shown in subcell 1 in figure 14. However, upon increasing U the orbital *polarizations* increase around the metal-insulator transition –from the small LDA values given in the top and bottom rows of figure 18– and become *nearly complete* after the Mott transition. For this to be true, in the insulators the DMFT must create a self-energy matrix which strongly and uniformly enhances the non-cubic part of the on-site LDA Hamiltonian matrix, *i.e.* for Σ in equation (30) we must have:

$$\Sigma_{x_i x_j, x_j x_k}(\omega) \approx \sum_m w_{x_i x_j, m} n_m U'_m(\omega)\, w_{x_j x_k, m}, \tag{31}$$

so that in the crystal-field representation

$$\Sigma_{mm'}(\omega) \approx \delta_{mm'}\Sigma_m(\omega) = \delta_{mm'} n_m U'_m(\omega), \tag{32}$$

where, as U' increases beyond U'_c, $n_m \to \sim 1$ while $\mathrm{Re}\, U'_m(\omega)$ tends towards a function which is roughly $\frac{a}{\omega} - \frac{1}{2}U' + O(\omega)$ for ω negative and $\frac{a}{\omega} + \frac{1}{2}U' + O(\omega)$ for ω positive, and $\mathrm{Re}\, U'_2(\omega)$ and $\mathrm{Re}\, U'_3(\omega)$ tend towards functions which are roughly $\frac{a}{\omega} + \frac{1}{2}U' + O(\omega)$ independently of the sign of ω. Here, a is a constant. This would mean that the Mott transition takes place in only *one* band, and that this band is the one described by the crystal-field orbital with lowest energy. Static mean-field methods like Hartree-Fock and LDA+U have no ω-dependence of $U'_m(\omega)$, and are therefore unable to split the half-full, lowest band into two. Unfortunately, we cannot present figures of $\Sigma_m(\omega)$ because the

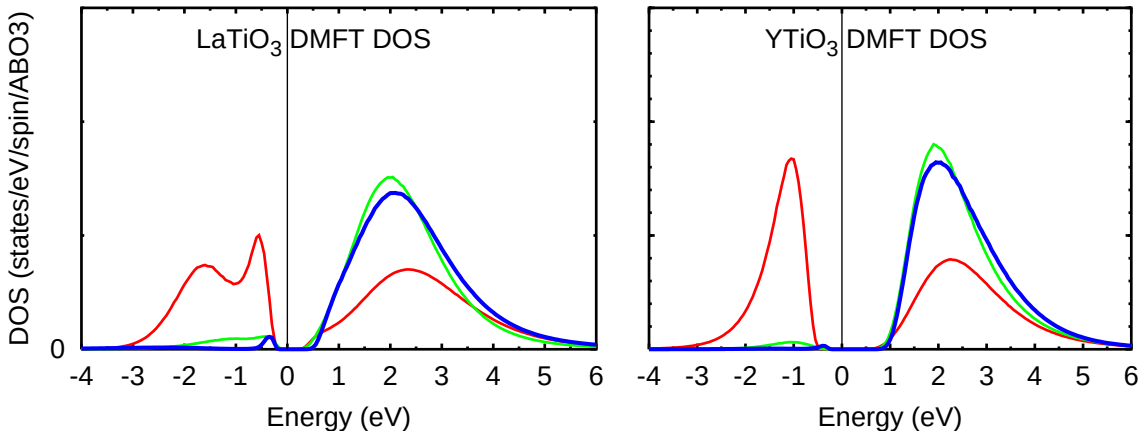

Figure 21. Diagonal elements of the spectral function in the crystal-field basis calculated with LDA+DMFT (U=5 and kT=0.1 eV). The corresponding figure for U=0 and kT=0 is the bottom part of figure 18, which also has the same colour coding: $|1\rangle$ red, $|2\rangle$ green, and $|3\rangle$ blue. The occupation of $|1\rangle$ is 0.88 for $LaTiO_3$ (older structure) and 0.96 for $YTiO_3$. Below ε_F there is one, and above there are five electrons. The off-diagonal elements are two orders of magnitude smaller than the diagonal ones.

methods we use to solve the Anderson impurity problem do not enable us to evaluate the self-energy for real ω.

Figure 21 shows the DOS for the titanates calculated with LDA+DMFT (U=5 eV and kT=0.1 eV) and projected onto the common eigenvectors of the occupation numbers and the crystal-field Hamiltonian. Hence, for $LaTiO_3$ the lowest crystal-field orbital contains 0.49 [12] (0.45 [44]) electrons when U=0 and 0.91 [12] (0.88 [44]) electrons when U= 5 eV. For $YTiO_3$, the respective occupations are 0.50 and 0.96. The nearly complete orbital polarization found for the two insulators indicates that *correlation effects* in the paramagnetic Mott insulating state considerably decrease orbital fluctuations, and makes it unlikely that $YTiO_3$ is a realization of an orbital liquid [57]. In $LaTiO_3$ some orbital fluctuations are still active, although quite weak.

Most recent NMR [58] and x-ray scattering [59] experiments point to an orbital order which is very similar to the one obtained in our calculations. For $LaTiO_3$ our occupied orbital is very similar to the one arrived at slightly earlier by Mochizuki and Imada [24] through model calculations to which we shall return in more detail in section 6. Also some of the results in the recent LDA+DMFT calculation for $La_{1-x}Sr_xTiO_3$ by Craco *et al.* [39] mentioned at the end of section 4 are similar to ours.

Our occupied orbital for $YTiO_3$ is similar to the one obtained with the spin-unrestricted LDA (actually GGA) scheme for T=0 [32]. This is understandable because the LDA properly accounts for the covalency and the electrostatics, and because the occupancy in the spin-unrestricted GGA is very similar to the one obtained by occupying the LDA DOS in the bottom right of figure 18 with a single spin-up electron, *i.e.* filling it to the Fermi level corresponding to n=2. The width of the band filled with one

spin-up electron is seen to be 0.8 eV so that in order to stabilize this ferromagnetic state, a Hund's-rule coupling constant exceeding 0.4 eV is required; this is well satisfied by our J=0.64 eV. In being *metallic,* this ferromagnetic ground state is, however, incorrect and the LDA+U scheme was needed to produce an insulator [32]. Our orbital in equation (20) agrees almost perfectly with the one deduced from NMR [33]: $|1\rangle = 0.8\,|yz\rangle + 0.6\,|xy\rangle$, and well with the one deduced from neutron scattering [34] and a small correction [60]: $|1\rangle = 0.7\,|yz\rangle + 0.7\,|xy\rangle$. Also resonant x-ray scattering confirms the orbital order [60, 61]. Mochizuki and Imada obtained a similar orbital to which we shall return in more detail in section 6.

To visualize the *orbital order,* the nearly full orbital was placed on each of the 4 Ti sites in figure 16. Despite the fact that $LaTiO_3$ and $YTiO_3$ have the same space group, the orbital orders look very different. This difference is, however, quantitative rather than qualitative; as mentioned in section 3.7, it reflects the extent to which the orbital has the *bc* plane as mirror. We emphasize once more that the two different types of JT distortions observed in $LaTiO_3$ and $YTiO_3$ are *not the cause* for the difference in the orbital orders. This was discussed for $YTiO_3$ in section 3.5, was clearly shown in figures 12 and 13, and was finally explicitly brought out in section 3.7 by the eigenvectors (21) and (22). It is however obvious that the oxygen octahedron will relax to the shape of the charge density of the localized electron, and this seems to be the reason why in $YTiO_3$ the O2 square is stretched by 3% into a rhomb along y in subcells 1 and 3, and along x in subcells 2 and 4 [20], while in $LaTiO_3$, it is stretched into a rectangle by 3% along a [12]. This is remarkable because in systems such as $LaMnO_3$, where the low-energy bands are of e_g type, orbital order and large (10%) JT distortions occur *together,* and the different types of orbital orderings are therefore often classified according to the type and spatial arrangement of the JT distortions. We have seen that this does not apply when the low-energy bands are of t_{2g} type, first of all because the t_{2g} orbitals have $pd\pi$ coupling to the *same* oxygen orbitals as the A ions have $pd\sigma$ coupling to and, secondly, because this $pd\pi$ coupling of the t_{2g} electrons is much weaker than the $pd\sigma$ coupling of the e_g electrons (see figures 5 and 6). In conclusion, the crystal-field splitting in the t_{2g}^1 perovskites is due to the $GdFeO_3$-type distortion.

We have thus seen that it is the Coulomb repulsion which causes the electron to localize, but it is chemistry which sets the stage: it determines U_c and selects the orbital to be occupied.

5.4. Pressure-induced metallization

Loa *et al.* recently performed high-pressure experiments on the titanates, in which they monitored the structures and the optical gaps [9]. Some of their results are shown in the left-hand side of figure 22. At 11 GPa, $LaTiO_3$ becomes metallic, its volume contracts slightly, but no apparent change of internal parameters occurs. For $YTiO_3$, the optical gap decreases with increasing pressure, but the material remains insulating up to at least 17 GPa. By extrapolation of this pressure dependence, it was estimated

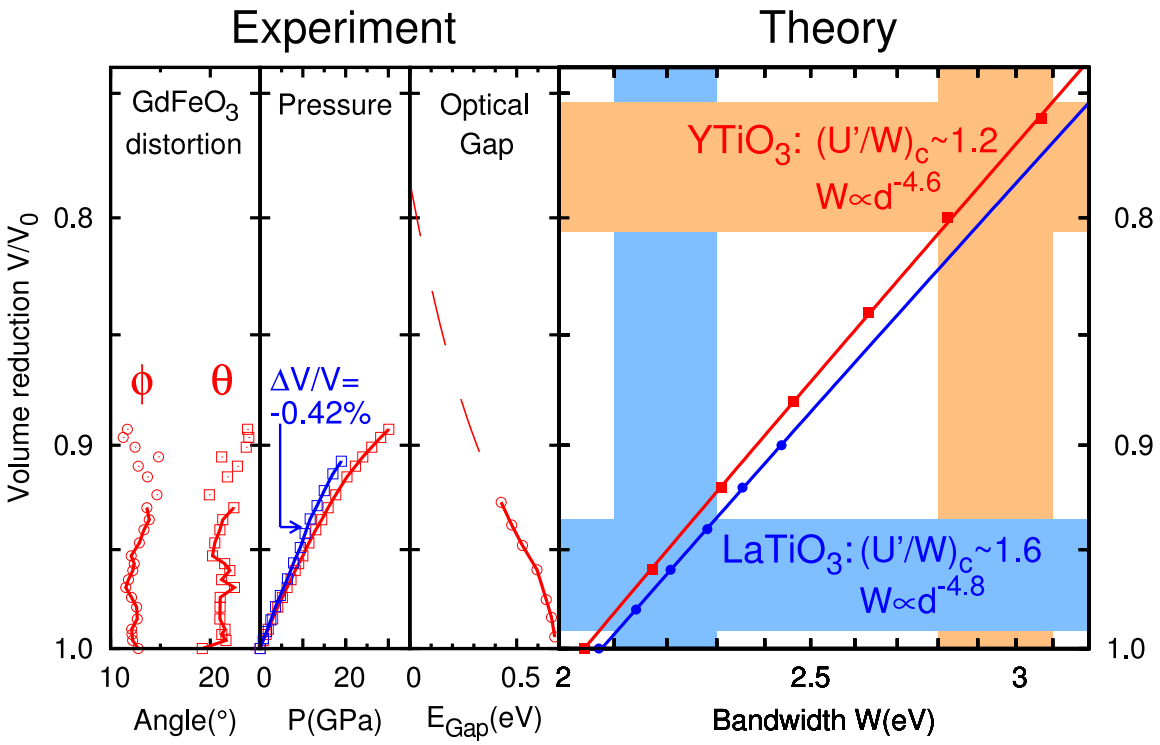

Figure 22. High-pressure metallization of $LaTiO_3$ (blue) and $YTiO_3$ (red). Experimental [9] and theoretical data (horizontal axes) as a function of the reduction of volume from that at normal pressure (vertical axis, log scale). θ and ϕ are the tilt and rotation angles. Rietveld refinement of the crystallographic data was only possible for $V > 0.93V_0$. For $YTiO_3$ the Mott transition has not been observed within the available pressure range, and the dashed line extrapolating the optical gap to zero is a theoretical guess from the right-hand side of the figure. For $LaTiO_3$, the Mott transition takes place at 11 GPa and V=$0.94V_0$, where a discontinuous contraction is observed. W is the calculated LDA t_{2g}-bandwidth (distance between band edges), which is seen to follow a power law in the Ti-Ti distance $d \propto V^{1/3}$. Since the experimental $GdFeO_3$-type distortion seems to be independent of volume, at least up to V=$0.9V_0$, the values U_c'=3.6 and 2.5 eV (table 10) obtained from our LDA+DMFT study of the Mott transition (figure 19) can be used to predict the metallization volume.

that metallization will occur above 40 GPa [9].

We may compute the metallization pressures using LDA+DMFT, provided that we know the structure. Luckily, the experimental data in the left-hand side of figure 22 give no reason to expect that the structures change by anything but a uniform compression; the $GdFeO_3$-type distortion seems to be fairly constant both for $LaTiO_3$ and for $YTiO_3$, at least up to a volume reduction of 0.9. We can therefore use our previous LDA+DMFT calculation of U_c', the value of the average on-site Coulomb repulsion necessary to drive the metal through a Mott transition (figure 19 and table 10), to predict the LDA t_{2g} bandwidth necessary to drive the insulator metallic. This gives:

$$W_c \sim 2.09 \text{ eV} \times \frac{5 - 2 \times 0.64}{3.6} = 2.2 \text{ eV for } LaTiO_3$$

and

$$W_c \sim 2.05 \text{ eV} \times \frac{5 - 2 \times 0.64}{2.5} = 3.0 \text{ eV for } YTiO_3.$$

Since only the width –not the shape– of the band changes, we have used here the simplest measure of the bandwidth, namely the energy distance between the band edges $\left(W_{t_{2g}}\right)$. To find the critical volume reduction, V_c/V_0, we now merely need to compute this bandwidth as a function of volume. The result is shown in the right-hand side of figure 22. The critical volume and corresponding pressure is then

$$V_c \sim 0.96V_0 \quad \text{and} \quad P_c \sim 7 \text{ GPa for } LaTiO_3,$$

which is in reasonable accord with the experiments, and

$$V_c \sim 0.78V_0 \quad \text{and} \quad P_c \sim 100 \text{ GPa for } YTiO_3.$$

For $YTiO_3$, V_c is uncertain because the $GdFeO_3$-distortion is only known to be constant for volumes larger than $0.9V_0$, but the corresponding, sketched behaviour of the optical gap does not look unreasonable. The critical pressure is more uncertain than the volume because it hinges on an extrapolation of the pressure-volume relation as well.

A most recent, refined study of $YTiO_3$ [9] revealed that between 9 and 14 GPa the JT distortion essentially disappears, but the distortion of the Y sublattice increases. This was mentioned at the end of section 3.5, and the 16 GPa structure was used to calculate the bandstructure shown on the right-hand sides of figures 12 and 13. This bandstructure justifies our approximation of assuming a rigid bandshape, although the Y positions shift so as to increase the residual covalency and, hence, to increase the pseudo-gap. A corresponding correction of U_c would be towards a slightly lower value, and that would *increase* our estimate –to *above* 100 GPa– for the pressure where metallization should occur if no further structural changes were to take place. Most importantly, the fact that the JT distortion is strongly reduced in the 16 GPa structure does *not* mean that the orbital order has changed drastically. That was explained at the end of the preceding subsection. The reduced JT distortion will, however, change the low-temperature magnetic order from ferromagnetic to A-type antiferromagnetic, as well as the ordering temperature. This we shall show in section 6.

5.5. Onset of optical absorption in the titanates

Let us calculate how the difference between $LaTiO_3$ and $YTiO_3$ shows up in the optical transitions between the lower and upper t_{2g} Hubbard bands seen in figure 21. Experimentally, the onset of the optical conductivity is more gradual in $LaTiO_3$ than in $YTiO_3$ [9, 62, 63].

The optical conductivity has previously been evaluated for $LaTiO_3$ in LDA+U [64] and LDA+DMFT [65] calculations. However, the $GdFeO_3$-type distortion, crucial to the present study, was neglected in both calculations where, on the other hand, the optical matrix elements were treated with more care than in our study.

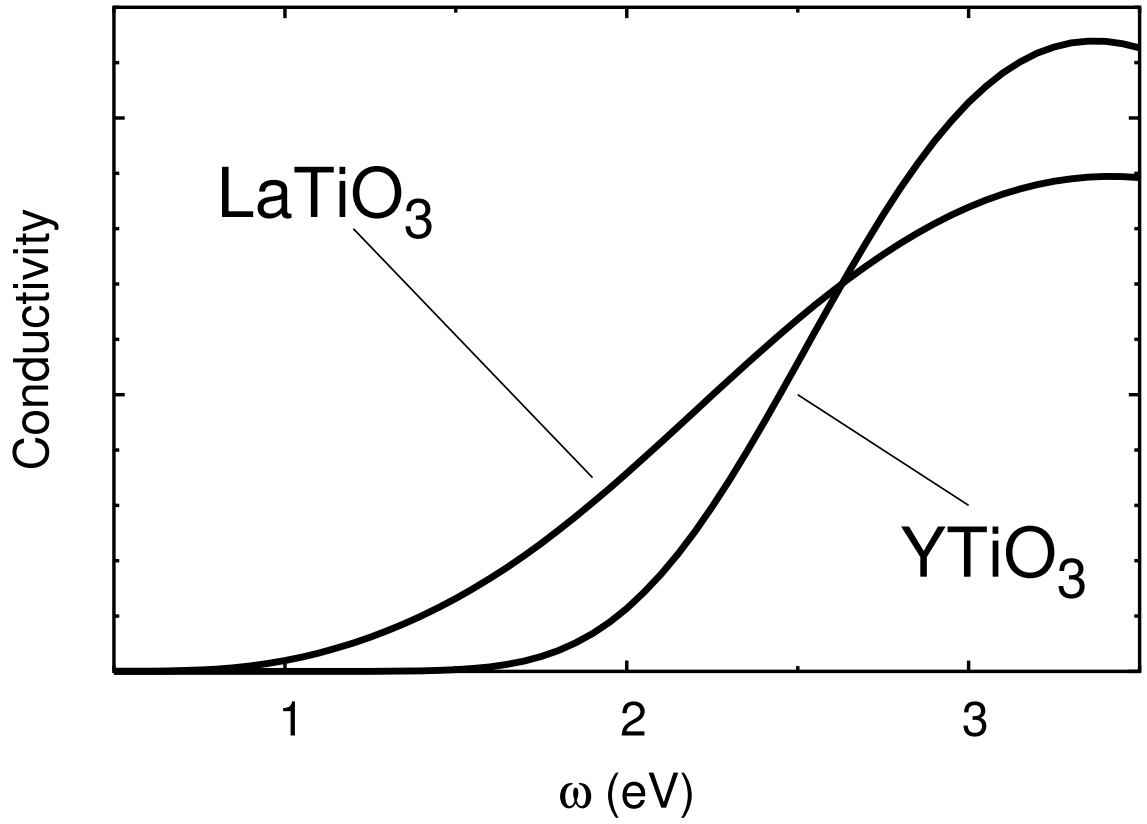

Figure 23. Real part of the optical conductivity obtained by LDA+DMFT with U=5 eV, kT=0.1 eV, and treating the matrix elements as explained in the text. The recent structural data for $LaTiO_3$ was used [12].

The optical conductivity can be expressed in terms of the current-current correlation function [66]. In the dynamical mean-field approximation there are no vertex corrections and the conductivity can therefore be written as [67, 68, 69]:

$$\sigma(\omega) \propto \frac{1}{\omega} \sum_{\mathbf{k}} \int d\omega' \left[n(\omega') - n(\omega + \omega') \right] \sum_{ijkl} M_{ij}\left(\mathbf{k}\right) A_{jk}(\mathbf{k}, \omega') M_{kl}\left(\mathbf{k}\right) A_{li}(\mathbf{k}, \omega' + \omega). \quad (33)$$

Here, $n(\omega)$ is the Fermi distribution function, $M_{ij}\left(\mathbf{k}\right)$ the optical matrix element, and

$$A_{ij}\left(\mathbf{k}, \omega\right) = \frac{1}{\pi} \mathrm{Im} \left\{ \left[\omega - \Sigma\left(\omega\right) - H^{LDA}\left(\mathbf{k}\right) \right]^{-1} \right\}_{ij}$$

the spectral function at real energy. The latter can be obtained by analytical continuation from the QMC data created in the course of an LDA+DMFT calculation. We shall assume that all transitions between t_{2g} crystal-field orbitals (see figure 21), and allowed by the Fermi functions, have *equal* probability. Compared with charge-transfer transitions (O $2p$–Ti $3d$ and O $2p$–A d), these transitions are all weak, and we do not expect some to be stronger than others. With this approximation, equation (33)

reduces to:

$$\sigma(\omega) \propto \frac{1}{\omega}\sum_{\mathbf{k}}\int d\omega' \left[n(\omega') - n(\omega+\omega')\right]\sum_{ij} A_{ij}(\mathbf{k},\omega')\sum_{ij} A_{ij}(\mathbf{k},\omega'+\omega),$$

where i and j now run over the crystal-field orbitals.

The real part of the optical conductivity obtained from our LDA+DMFT (U=5 eV, kT=0.1 eV) calculations are given in figure 23. By going from the indirect DOS gaps in figures 20 and 21 to the direct gaps in figure 23, the latter are seen to be increased by approximately 0.5 eV, to 0.8 eV in $LaTiO_3$ and to 1.5 eV $YTiO_3$. We observe that, even without detailed matrix-element effects, the onset of inter-band transitions is more gradual in $LaTiO_3$ than in $YTiO_3$. That is presumably the same trend as seen for the upper Hubbard band in figure 21, where the lower edge of bands $|2\rangle$ and $|3\rangle$ rises more gradually in $LaTiO_3$ than in $YTiO_3$; in $LaTiO_3$ the peak is reached after 1.5 eV, but in $YTiO_3$ after 1.0 eV.

6. Low-temperature, magnetic properties of the titanates

6.1. Introduction

The origin of the magnetic phases of $LaTiO_3$ and $YTiO_3$ have been a puzzle for decades [2, 3]. Whereas $LaTiO_3$ is a G-type antiferromagnet with T_N=150 K and a small moment of 0.57 μ_B, $YTiO_3$ is a ferromagnet with a low Curie temperature, T_C=30 K, and a good-sized moment, 0.8μ_B [11, 12].

The early idea was that in Mott insulators, the magnetic structure is rooted in orbital order. Hence, the different magnetic ground states in $LaTiO_3$ and $YTiO_3$ ought to arise from different orbital orders. Orbital order, presumably caused by electron correlation, should be accompanied by a JT elongation of the TiO_6 octahedron, and in perovskites the stacking along the c axis was found to be either parallel (d type) or perpendicular (a type). Since the d^1 titanates were found to have a mirror plane perpendicular to the c axis, they have d type orbital order if they are JT distorted. In $YTiO_3$, a small (3%) JT distortion was observed, but hardly any in $LaTiO_3$. In their series of model Hartree-Fock calculations, Mizokawa and Fujimori could obtain an antiferromagnetic ground state for $LaTiO_3$ –but only by virtue of the spin-orbit coupling– as well as the ferromagnetic ground state for $YTiO_3$. However, they could not explain why d- rather than a-type orbital order is realized in $YTiO_3$ [25]. This problem was later solved by Mizokawa, Khomskii, and Sawatzky by including A d orbitals together with the $GdFeO_3$-type distortion in their model. However, these authors also noted that, given the smallness of any JT distortion in $LaTiO_3$, this mechanism would make $LaTiO_3$ ferro- rather than antiferromagnetic [26].

Early on in the game, the correct magnetic orders had actually been computed by Solovyev, Hamada, and Terakura for $LaTiO_3$ [31] and by Sawada and Terakura for $YTiO_3$ [32] with the LDA+U method. They adjusted U to the experimentally measured

Mott gap. Their *orbital* order for $YTiO_3$ was subsequently confirmed by NMR [33], neutron scattering [34], and resonant x-ray scattering [61].

The spin-wave spectra were then measured and found to be essentially isotropic and gapless in both titanates [10, 40]. This lead Khaliullin and collaborators to question the existence of orbital order in the titanates. They demonstrated that with the accepted orbital order in $YTiO_3$, conventional super-exchange theory, as used in the model studies, leads to an *an*isotropic spin-wave spectrum and, even worse, to an antiferromagnetic ground state. If, on the other hand, the t_{2g} levels were degenerate, the isotropy of the spin-wave spectra could easily be explained by strong quantum fluctuations in orbital space (orbital liquid theory [16, 57]). The assumption that the t_{2g} levels are nearly degenerate was justified by the smallness of the observed JT distortions.

Mochizuki and Imada [28] then pointed out that in order to obtain the observed G-type antiferromagnetism, as well as exchange-coupling constants in accord with the measured spin-wave spectra ($J_{se}^{001} = J_{se}^{010/100} = 15\,\mathrm{meV}$), it would suffice if the Ti $3d_{3z^2_{111}-1}$ level were lower than the two other t_{2g} levels by an amount exceeding the spin-orbit splitting and kT, *i.e.* by $\gtrsim$40 meV. A tiny deformation of the octahedron along [111] would enable this. They also gave arguments why such an orbital order had not been observed in resonant x-ray scattering [10]. At the same time [27], Mochizuki and Imada published strong-coupling (in U/t, as in super-exchange theory) studies of the antiferromagnetic-to-ferromagnetic transition, which takes place as the angle of the O-Ti-O bond ($\sim$ degree of $GdFeO_3$-type distortion) decreases beyond that in $LaTiO_3$. In these studies, the JT distortion was assumed to be d-like, that is, with one level (xz on site 1) *above* a doubly-degenerate level (yz and xy on site 1). The dominant effect was found to be the t_{2g}-to-e_g hopping via oxygen which increases with distortion, as we have seen in figures 14 and 15. Such hopping processes make it possible to reach virtual high-spin states with configuration $t_{2g}^{\uparrow}e_g^{\uparrow}$ and, hence, favour ferromagnetism. This study [27] therefore predicted that the orbital order is not influenced by the increasing $GdFeO_3$-type distortion, but that the exchange coupling along the z direction, where the t_{2g}-p-e_g hopping is strongest, changes sign from A-type antiferromagnetic (*i.e.,* ferromagnetic parallel to the mirror plane) to ferromagnetic. None of these studies [27, 28] included the A d orbitals which had been found crucial by Mizokawa, Khomskii, and Sawatzky [26].

Now, orbital-liquid theory had predicted that there be a significant contribution to the specific heat at low temperature, but this was not observed [18, 19]. Moreover, a 3% JT stretch of one of the basal O squares into a rectangle was recently discovered in $LaTiO_3$ [12], thus bringing strong evidence for non-degenerate t_{2g} levels and a JT distortion of a different type than the one in $YTiO_3$. Mochizuki and Imada finally [24, 29] included the A d orbitals and realized that what stabilizes a single level with $d_{3z^2_{111}-1}$-character, and therefore G-type antiferromagnetism, is not JT distortion, but the $GdFeO_3$-type distortion which makes the A ions produce a crystal field. Its electrostatic and covalent contributions were estimated to give about the same lowest state, namely $|1\rangle = 0.68\,|yz\rangle + 0.41\,|zx\rangle + 0.61\,|xy\rangle$. With this orbital order, they

obtained super-exchange coupling constants ($J_{se}^{001} = 19.7\,\mathrm{meV}$ and $J_{se}^{010/100} = 18.5\,\mathrm{meV}$) in almost perfect agreement with the experimental values [10]. Proceeding along the series of rare-earth titanates with decreasing ionic radius from $LaTiO_3$ to $SmTiO_3$, the J_{se} values were found to decrease by 20%, and the lowest orbital to become $|1\rangle = 0.73\,|yz\rangle + 0.24\,|zx\rangle + 0.63\,|xy\rangle$. From this continuous transition towards the case of $YTiO_3$, it was concluded that beyond Sm the JT distortion should be *the* factor which controls the magnetism, *i.e.* the JT distortion should be responsible for the ferromagnetism of $YTiO_3$ [29]. This work did not mention including the coupling to the e_g degrees of freedom.

Essentially the same conclusions were reached independently, and in one shot, by using a new, parameter-free density-functional approach [21]. The present paper tells the story as it is seen from that side. The fact that very similar conclusions concerning the splitting of the orbital degeneracy and its universal origin were reached in such a short time, not only by different theory groups, but by many experimental groups as well, strengthens the case for those conclusions. Nevertheless, we, too, must demonstrate that the orbital order obtained is consistent with the magnetic structures and the spin-wave spectra [10, 40]. We thus move a step backwards and repeat Khaliullin's calculation [40] of the inter-atomic exchange integrals by 2nd-order perturbation theory in t/U, this time using the crystal-fields and hopping integrals obtained from our LDA Wannier functions:

6.2. Super-exchange couplings

The super-exchange Hamiltonian is obtained from the t_{2g} Hubbard Hamiltonian, $\mathcal{H}_{t_{2g}}$, given by expression (27), including now the spin-flip terms neglected for the purpose of the DMFT calculations. Following the standard approach, we work in the many-electron representation which diagonalizes the *on-site* terms, $\mathcal{H}^{LDA}_{t_{2g};R=R'} + \mathcal{U}_R$, of $\mathcal{H}_{t_{2g}}$. The remaining, non-diagonal part of $\mathcal{H}_{t_{2g}}$ is the LDA hopping, $\mathcal{T}$. The super-exchange Hamiltonian, $\mathcal{H}_{se}$, is then obtained by Löwdin downfolding (A.5) of the subspace which has one or more sites doubly occupied:

$$\mathcal{H}_{se} = \mathcal{P}_s \mathcal{T} \left\{ (1 - \mathcal{P}_s) \left(E - \mathcal{H}_{t_{2g}} \right) (1 - \mathcal{P}_s) \right\}^{-1} \mathcal{T} \mathcal{P}_s. \tag{34}$$

Here, $\mathcal{P}_s$ projects onto the subspace of singly-occupied sites. To order t/U, the projection $1 - \mathcal{P}_s$ can be substituted by $\mathcal{P}_d$, which projects onto the space of *one* doubly-occupied site, and $\mathcal{H}_{t_{2g}}$ can be substituted by the on-site part of the Hamiltonian. Expression (34) then reduces to the 2nd-order perturbation expansion for $\mathcal{H}_{se}$ used by Khaliullin *et al.*

We now specialize to the cases of $LaTiO_3$ and $YTiO_3$. As explained in the previous section, the main result of our many-body LDA+DMFT calculations was that the density matrix is diagonalized by the crystal-field orbitals, $|m\rangle$, and that the orbital with the lowest energy, $|1\rangle$, is occupied with 0.91 electron in $LaTiO_3$ and with 0.96 in $YTiO_3$. In the following, we shall assume that $|1\rangle$ is *completely* occupied. For the *two* sites, R and R', between which we want to compute the super-exchange coupling, the

states with *no* double occupancy, *i.e.* $t_{2g}^1 + t_{2g}^1$, are then the Slater determinants $|1)$ through $|4)$ in the pictogram below, and the states with *one* double occupancy with which they couple, line by line in the pictogram, are the 15 t_{2g}^2 states $|5)$ through $|19)$ (soft bras and kets denote two-electron states):

$$
|1) = \begin{array}{|cc|}\hline - & - \\ - & - \\ \uparrow & \downarrow \\ \hline\end{array}
\qquad
|5) = \begin{array}{|cc|}\hline - & - \\ - & - \\ - & \uparrow\downarrow \\ \hline\end{array}
\qquad
|6) = \begin{array}{|cc|}\hline - & - \\ - & \uparrow \\ - & \downarrow \\ \hline\end{array}
\qquad
|7) = \begin{array}{|cc|}\hline - & \uparrow \\ - & - \\ - & \downarrow \\ \hline\end{array}
$$

$$
|2) = \begin{array}{|cc|}\hline - & - \\ - & - \\ \downarrow & \uparrow \\ \hline\end{array}
\qquad
|5) = \begin{array}{|cc|}\hline - & - \\ - & - \\ - & \uparrow\downarrow \\ \hline\end{array}
\qquad
|8) = \begin{array}{|cc|}\hline - & - \\ - & \downarrow \\ - & \uparrow \\ \hline\end{array}
\qquad
|9) = \begin{array}{|cc|}\hline - & \downarrow \\ - & - \\ - & \uparrow \\ \hline\end{array}
$$

$$
|3) = \begin{array}{|cc|}\hline - & - \\ - & - \\ \uparrow & \uparrow \\ \hline\end{array}
\qquad
|10) = \begin{array}{|cc|}\hline - & - \\ - & \uparrow \\ - & \uparrow \\ \hline\end{array}
\qquad
|11) = \begin{array}{|cc|}\hline - & \uparrow \\ - & - \\ - & \uparrow \\ \hline\end{array}
\qquad
|14) = \begin{array}{|cc|}\hline - & - \\ - & \uparrow\downarrow \\ - & - \\ \hline\end{array}
$$

$$
|4) = \begin{array}{|cc|}\hline - & - \\ - & - \\ \downarrow & \downarrow \\ \hline\end{array}
\qquad
|12) = \begin{array}{|cc|}\hline - & - \\ - & \downarrow \\ - & \downarrow \\ \hline\end{array}
\qquad
|13) = \begin{array}{|cc|}\hline - & \downarrow \\ - & - \\ - & \downarrow \\ \hline\end{array}
\qquad
|15) = \begin{array}{|cc|}\hline - & \uparrow\downarrow \\ - & - \\ - & - \\ \hline\end{array}
$$

$$
|16) = \begin{array}{|cc|}\hline - & \downarrow \\ - & \uparrow \\ - & - \\ \hline\end{array}
\qquad
|17) = \begin{array}{|cc|}\hline - & \uparrow \\ - & \downarrow \\ - & - \\ \hline\end{array}
\qquad
|18) = \begin{array}{|cc|}\hline - & \uparrow \\ - & \uparrow \\ - & - \\ \hline\end{array}
\qquad
|19) = \begin{array}{|cc|}\hline - & \downarrow \\ - & \downarrow \\ - & - \\ \hline\end{array}
\quad . \tag{35}
$$

In this space of 19 two-electron states, the matrix element of the Hamiltonian $\mathcal{H}_{t_{2g}}$ between states $(1|$ through $(4|$ and $|5)$ through $|13)$ is a hopping integral, such as $(1R|\mathcal{H}_{t_{2g}}|7R') = \left\langle 1R \left| \mathcal{H}_{t_{2g}}^{LDA} \right| 3R' \right\rangle \equiv t_{13}$ between crystal-field orbital $|1\rangle$ on site R and crystal-field orbital $|3\rangle$ on site R'. The matrix elements in the t_{2g}^2-subspace are the eigenfunctions of $\mathcal{U}$ plus the crystal-field splittings, $\Delta_m \equiv \epsilon_m - \epsilon_1$. Now, the orders of magnitude produced by our LDA calculations for the titanates are: $t \sim \Delta \sim 0.3J \sim 0.04U$, and we may therefore neglect Δ when evaluating the t_{2g}^2 eigenfunctions (although this is not done in our numerical calculations). The t_{2g}^2 eigenfunctions are then simply the p^2-states listed following expression (27). The transformation from the two-electron basis (35) to the one which diagonalizes $\mathcal{U}$ is very simple: it merely involves combining states $|6)$ and $|8)$ into a singlet and a triplet (belonging to respectively ^1D and ^3P), the same for $|7)$ and $|9)$, and combining states $|5)$, $|14)$, and $|15)$ into the ^1S singlet and the two singlets belonging to ^1D. One of the latter does not couple to the singly-occupied states $|1)$ through $|4)$, and the same holds for the three triplets formed from $|16)$ through $|19)$. The singlet formed from states $|16)$ and $|17)$ belonging to ^1D does

not couple either. As a result, the off-diagonal block of $H_{t_{2g}} - 2\epsilon_1$ is then:

$$
\begin{array}{c|ccccccccccc}
 & \frac{1}{\sqrt{3}}\times\begin{bmatrix}|5)\\ +|14)\\ +|15)\end{bmatrix} & \frac{1}{\sqrt{6}}\times\begin{bmatrix}2|5)\\ -|14)\\ -|15)\end{bmatrix} & \frac{1}{\sqrt{2}}\times\begin{bmatrix}|6)\\ +|8)\end{bmatrix} & \frac{1}{\sqrt{2}}\times\begin{bmatrix}|7)\\ +|9)\end{bmatrix} & \frac{1}{\sqrt{2}}\times\begin{bmatrix}|6)\\ -|8)\end{bmatrix} & \frac{1}{\sqrt{2}}\times\begin{bmatrix}|7)\\ -|9)\end{bmatrix} & |10) & |11) & |12) & |13) \\
(1| & \frac{t_{11}}{\sqrt{3}} & \sqrt{\frac{2}{3}}t_{11} & \frac{t_{12}}{\sqrt{2}} & \frac{t_{13}}{\sqrt{2}} & \frac{t_{12}}{\sqrt{2}} & \frac{t_{13}}{\sqrt{2}} & 0 & 0 & 0 & 0 \\
(2| & \frac{t_{11}}{\sqrt{3}} & \sqrt{\frac{2}{3}}t_{11} & \frac{t_{12}}{\sqrt{2}} & \frac{t_{13}}{\sqrt{2}} & -\frac{t_{12}}{\sqrt{2}} & -\frac{t_{13}}{\sqrt{2}} & 0 & 0 & 0 & 0 \\
(3| & 0 & 0 & 0 & 0 & 0 & 0 & t_{12} & t_{13} & 0 & 0 \\
(4| & 0 & 0 & 0 & 0 & 0 & 0 & 0 & 0 & t_{12} & t_{13} \\
. & U+2J+\frac{2}{3}(\Delta_2+\Delta_3) & 0 & 0 & 0 & 0 & 0 & 0 & 0 & 0 & 0 \\
. & 0 & U-J+\frac{1}{3}(\Delta_2+\Delta_3) & 0 & 0 & 0 & 0 & 0 & 0 & 0 & 0 \\
. & 0 & 0 & U-J+\Delta_2 & 0 & 0 & 0 & 0 & 0 & 0 & 0 \\
. & 0 & 0 & 0 & U-J+\Delta_3 & 0 & 0 & 0 & 0 & 0 & 0 \\
. & 0 & 0 & 0 & 0 & U-3J+\Delta_2 & 0 & 0 & 0 & 0 & 0 \\
. & 0 & 0 & 0 & 0 & 0 & U-3J+\Delta_3 & 0 & 0 & 0 & 0 \\
(10| & 0 & 0 & 0 & 0 & 0 & 0 & U-3J+\Delta_2 & 0 & 0 & 0 \\
(11| & 0 & 0 & 0 & 0 & 0 & 0 & 0 & U-3J+\Delta_3 & 0 & 0 \\
(12| & 0 & 0 & 0 & 0 & 0 & 0 & 0 & 0 & U-3J+\Delta_2 & 0 \\
(13| & 0 & 0 & 0 & 0 & 0 & 0 & 0 & 0 & 0 & U-3J+\Delta_3
\end{array}
\tag{36}
$$

Running along the rows, we have the following t_{2g}^2-states: the ^1S-state, three of the five ^1D-states, and six of the nine ^3P-states. With the high-energy subspace diagonalized, it is now trivial to downfold to the low-energy subspace, $|1)$ through $|4)$, obtaining the super-exchange Hamiltonian (34) with $E = 2\epsilon_1$. For the energy difference between the Néel state and the ferromagnetic state, we thus obtain:

$$(3|\mathcal{H}_{se}|3) - (1|\mathcal{H}_{se}|1) = t_{11}^2\left(\frac{\frac{1}{3}}{U+2J} + \frac{\frac{2}{3}}{U-J}\right) + \frac{t_{12}^2+t_{13}^2}{2}\left(\frac{1}{U-J} - \frac{1}{U-3J}\right), \tag{37}$$

which for spin $\frac{1}{2}$, is $\frac{1}{4}$ times the super-exchange coupling, J_{se}, between the two sites considered. For simplicity, and because it is a good approximation, we have left out the

crystal-field splittings in the denominators, but they are trivial to include by returning to the full Hamiltonian (36).

The super-exchange coupling (37) is the sum of terms caused by intra- and inter-level hops. As is well known, the first term is positive, that is, it favours antiferromagnetic alignment, and the latter is negative. Ferromagnetic alignment is thus favoured when the hopping to excited levels exceeds the hopping in the ground state by a critical ratio, τ_0 :

$$\frac{\sqrt{\frac{1}{2}\left(t_{12}^2+t_{13}^2\right)}}{|t_{11}|} \equiv \tau > \tau_0 \equiv \sqrt{\frac{(1+J/U)\,(1-3J/U)}{(2J/U)\,(1+2J/U)}}. \tag{38}$$

For the actual value of the ratio between the Hund's-rule coupling to the Coulomb repulsion, $J/U = 0.64/5 \approx 0.13$, this equation gives $\tau_0 = 1.47$. Similarly, for a given ratio of inter- to intra-level hopping integrals, one may find a critical value of the Hund's-rule coupling to be exceeded in order to produce ferromagnetic coupling:

$$\frac{J}{U} > \left(\frac{J}{U}\right)_0 = \frac{\sqrt{4+6\tau^2+\tau^4}-1-\tau^2}{3+4\tau^2}. \tag{39}$$

We now consider the super-exchange coupling between two nearest neighbours on either side of the mirror plane, *i.e.* those separated by 001, and between two nearest neighbours in the xy-plane, *i.e.* those separated by 010 or 100. In the latter case, we must average over the two sites related by a glide mirror, and this amounts to taking the average of the 010 and 100 exchange couplings. Couplings between farther neighbours are very small because the squares of the corresponding hopping integrals determine J_{se}, so we neglect them. In table 11, we have extracted t_{1m}^{010} and t_{1m}^{100} for $LaTiO_3$ from equation (23), and t_{1m}^{001} from equation (25). For $YTiO_3$, we use equations (24) and (26) in the same way. From these hopping integrals and the values of U and J, we can now evaluate the various contributions in (37) to the super-exchange coupling, and the corresponding rows have been inserted in the tables. The summed up, total J_{se} may be found in an inserted row. Finally, J_{se} evaluated numerically without neglecting the crystal-field splittings has been included in a row marked J_{se}^{Δ}.

For $LaTiO_3$ and the coupling to 001, we see that the antiferromagnetic intra-level hopping dominates and that the total J_{se}^{001} is 5.0 meV. Including the crystal-field splittings makes no difference in this case. Parallel to the mirror plane, a couple of large inter-level hopping integrals make the total exchange constant smaller, $J_{se}^{100/010} = 3.2\,\text{meV}$, but still antiferromagnetic. These values are much smaller than the values obtained from the neutron scattering [10] and Raman experiments [70], and also than the values obtained with the model Hamiltonian [24, 29]. With the older structural data [44], we find the perpendicular and the parallel exchange-coupling constants to be both 6 meV. Using the low-temperature structural data [12], we compute the LDA Hamiltonian given in the left-hand side of table 7, and with that, we can calculate the crystal-field eigenvalues and vectors like in equation (19), and then transform the hopping integrals to the crystal-field representation like in equations (23) and (25). The result is given in table 12: due to a 10% increase of $t_{11}^{010} = t_{11}^{010}$ the isotropy is increased,

Table 11. Hopping integrals, t_{1m}^{xyz}, and superexchange couplings, J_{se}, in meV

	$LaTiO_3$						$YTiO_3$					
xyz	001		010		100		001		010		100	
$1,m$	t_{1m}	J_{se}	t_{1m}	J_{se}	t_{1m}	J_{se}	t_{1m}	J_{se}	t_{1m}	J_{se}	t_{1m}	J_{se}
$1,1$	105	9.1	−98	7.9	−98	7.9	−38	1.2	−48	1.9	−48	1.9
$1,2$	31	−0.2	−192	−7.0	4	−0.0	−21	−0.1	−191	−7.0	−84	−1.3
$1,3$	143	−3.9	12	0.0	120	−2.7	97	−1.8	−130	−3.2	94	−1.7
J_{se}		5.0		0.9		5.2		−0.7		−8.3		−1.1
J_{se}^{Δ}		5.0				3.2		−0.5				−4.0
τ		0.99				1.16		1.85				2.74
$\left(\frac{J}{U}\right)_0$		0.19				0.16		0.10				0.05

Table 12. t_{1m}^{xyz} and J_{se} in meV for $LaTiO_3$ at T=8 K.

xyz	001		010		100	
$1,m$	t_{1m}	J_{se}	t_{1m}	J_{se}	t_{1m}	J_{se}
$1,1$	114	10.7	−108	9.6	−108	9.6
$1,2$	43	−0.4	−182	−6.3	23	−0.1
$1,3$	142	−3.8	23	−0.1	119	−2.7
J_{se}		6.5		3.2		6.8
τ		0.92				1.02
$\left(\frac{J}{U}\right)_0$		0.20				0.18

$J_{se}^{001} = 6.5$ and $J_{se}^{100/010} = 5.0\,\text{meV}$, but our *ab initio* exchange coupling remains 2–3 times smaller than the experimental value. Had we, instead of the computed crystal-field eigenvectors (19), used the simplified ones:

$$\begin{pmatrix} |1\rangle & |2\rangle & |3\rangle \end{pmatrix} = \begin{pmatrix} |yz\rangle & |xz\rangle & |xy\rangle \end{pmatrix} \begin{pmatrix} \frac{1}{\sqrt{3}} & -\frac{1}{\sqrt{2}} & \frac{1}{\sqrt{6}} \\ \frac{1}{\sqrt{3}} & \frac{1}{\sqrt{2}} & \frac{1}{\sqrt{6}} \\ \frac{1}{\sqrt{3}} & 0 & -\frac{2}{\sqrt{6}} \end{pmatrix}, \qquad (40)$$

where $|1\rangle = 3z_{111}^2 - 1$, we would have obtained $J_{se}^{001} = 15$ and $J_{se}^{100/010} = 10\,\text{meV}$, as shown in table 13 below. This demonstrates the extreme sensitivity of the exchange coupling constants to the crystal-field eigenvectors.

For $YTiO_3$, the small intra-level 001 hopping makes the ferromagnetic inter-level coupling dominate so that $J_{se}^{001} = -0.5$ meV, as seen in table 11. Parallel to the

Table 13. t_{1m}^{xyz} and J_{se} in meV using the simplified eigenvectors (40) and (41).

	$LaTiO_3$						$YTiO_3$					
xyz	001		010		100		001		010		100	
$1,m$	t_{1m}	J_{se}	t_{1m}	J_{se}	t_{1m}	J_{se}	t_{1m}	J_{se}	t_{1m}	J_{se}	t_{1m}	J_{se}
$1,1$	150	18.5	−128	13.5	−128	13.5	−35	1.0	−84	5.8	−84	5.8
$1,2$	51	−0.5	−133	−3.4	71	−1.0	−36	−0.2	−132	−3.3	−100	−1.9
$1,3$	126	−3.0	12	−0.0	101	−1.9	103	−2.0	−175	−5.8	65	−0.8
J_{se}		15.0		10.1		10.6		−1.3		−3.3		3.1
		10.3										−0.1
τ		0.64				0.71		2.20				1.49
$\left(\frac{J}{U}\right)_0$		0.25				0.24		0.07				0.13

mirror-plane the large inter-orbital hopping integrals, however, make the calculated exchange coupling robustly ferromagnetic: $J_{se}^{100/010} = -4.0\,\text{meV}$. This is consistent with the measured Curie temperature and the spin-wave spectra, which give −3 meV [40]. Had we, like for $LaTiO_3$, used simplified crystal-field eigenvectors for $YTiO_3$, namely

$$\begin{pmatrix} |1\rangle & |2\rangle & |3\rangle \end{pmatrix} = \begin{pmatrix} |yz\rangle & |xz\rangle & |xy\rangle \end{pmatrix} \begin{pmatrix} \frac{1}{\sqrt{2}} & -\frac{1}{\sqrt{2}} & 0 \\ 0 & 0 & 1 \\ \frac{1}{\sqrt{2}} & \frac{1}{\sqrt{2}} & 0 \end{pmatrix}, \tag{41}$$

we would have obtained $J_{se}^{001} = -1.3$ and $J_{se}^{100/010} = -0.1\,\text{meV}$, as demonstrated in the right-hand side of table 13. So $YTiO_3$ does stay ferromagnetic, but just barely.

From the hopping integrals, we can also calculate the ratio, τ, between the intra- and inter-level hoppings using (38). The corresponding lines have been added at the bottom of tables 11–16. We see that for both titanates, τ is *nearly isotropic* and, for $LaTiO_3$, it is significantly *smaller* than the critical ratio, τ_0=1.47, whereas for $YTiO_3$, it is significantly larger. This agrees with the experimental facts. Obviously, the small t_{11} and the large t_{12} and t_{13} in $YTiO_3$, make this material profit from the Hund's-rule coupling in the t_{2g}^2 state and, hence, have a ferromagnetic ground state.

Using (39) we can calculate the critical J/U ratio needed for the coupling to be ferromagnetic. $(J/U)_0$ is seen to be significantly larger than the actual value (0.13) for $LaTiO_3$, and significantly smaller in $YTiO_3$. In the bottom panels of figure 24 we show the perpendicular (red) and parallel (blue) exchange couplings as functions of J/U, computed with inclusion of the crystal-field splittings. The latter are seen to have only minor effects, at least on the scale of the figure, but not on the scale of experiments, *e.g.* the largest deviation of the critical J/U values obtained without crystal-field splitting is found for the in-plane exchange coupling in $LaTiO_3$. Here, the full calculation in the figure gives $(J/U)_0$=0.175, while the approximate value quoted in the table is 0.19.

Table 14. t_{1m}^{xyz} and J_{se} in meV for cubic hopping.

	$LaTiO_3$							$YTiO_3$						
xyz	001		010		100			001		010		100		
$1,m$	t_{1m}	J_{se}	t_{1m}	J_{se}	t_{1m}	J_{se}		t_{1m}	J_{se}	t_{1m}	J_{se}	t_{1m}	J_{se}	
1,1	96	7.6	−89	6.5	−89	6.5		92	7.0	−49	2.0	−49	2.0	
1,2	−20	−0.1	−110	−2.3	5	−0.0		−70	−0.9	−108	−2.2	−76	−1.1	
1,3	69	−0.9	15	−0.0	49	−0.5		19	−0.1	−91	−1.6	22	−0.1	
J_{se}		6.6		4.2		6.1	5.2		6.0		−1.8		0.8	−0.5
τ		0.53					0.68		0.56					1.65
$\left(\frac{J}{U}\right)_0$		0.27					0.24		0.27					0.11

Table 15. t_{1m}^{xyz} and J_{se} in meV for simplified eigenvectors and cubic hopping.

	$LaTiO_3$							$YTiO_3$						
xyz	001		010		100			001		010		100		
$1,m$	t_{1m}	J_{se}	t_{1m}	J_{se}	t_{1m}	J_{se}		t_{1m}	J_{se}	t_{1m}	J_{se}	t_{1m}	J_{se}	
1,1	100	8.2	−100	8.2	−100	8.2		75	4.6	−75	4.6	−75	4.6	
1,2	0	0.0	−61	−0.7	61	−0.7		−75	−1.1	−75	−1.1	−75	−1.1	
1,3	71	−1.0	35	−0.2	35	−0.2		0	0.0	−106	−2.1	0	0.0	
J_{se}		7.3		7.3		7.3	7.3		3.6		1.4		3.6	2.5
τ		0.50					0.50		0.71					1.00
$\left(\frac{J}{U}\right)_0$		0.28					0.28		0.24					0.19

Our LDA-NMTO results should be seen on the background of the claim [40] that orbital order is inconsistent with the observed magnetic ground states and isotropic spin-wave spectra in $YTiO_3$. This claim was based on the assumption that the *hopping* is as in the *cubic* structure, where the xy, yz, and xz bands are identical, independent, and 2D. In that case, there is only *one* nearest-neighbour hopping integral, the effective t_π between two similar orbitals in the same plane (in case of $SrVO_3$, this is the −281 meV quoted in table 1). As we have seen and explained in great detail in section 3, the hopping between the xy, yz, and xz LDA Wannier functions is, however, *very different* due to the $GdFeO_3$-type distortion in the titanates. In order to demonstrate that this is the reason for the discrepancy between our calculation and that of Khaliullin [40], we first of all note that our expression (37) reduces to their equation (3) if one assumes

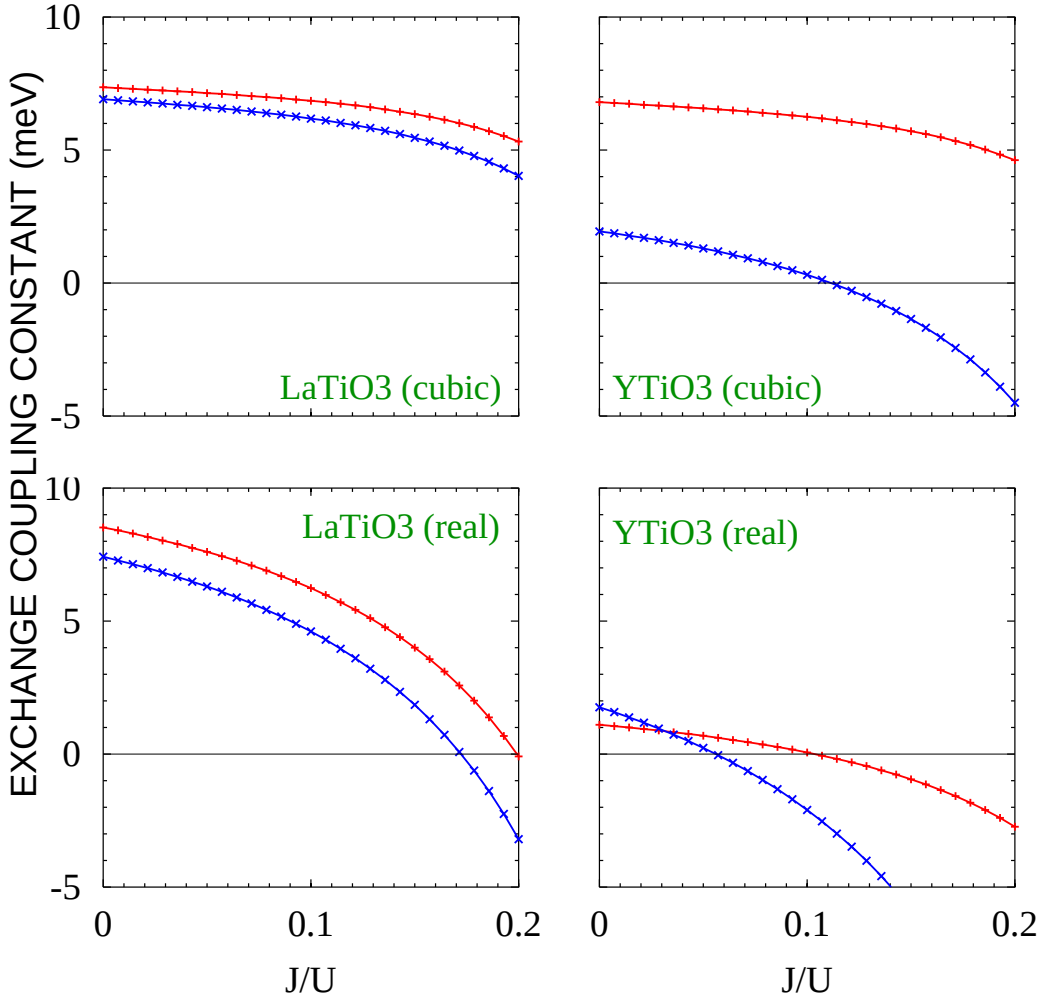

Figure 24. Nearest-neighbour exchange coupling constants perpendicular (red) and parallel (blue) to the mirror planes as functions of the ratio between the Hund's-rule coupling and the on-site repulsion, J/U. See figure 4 in reference [40]. Antiferro- and ferromagnetic couplings are respectively positive and negative. Input were $U = 5$ eV and the orbitally ordered states given by equations (19) and (20). In the upper row, degenerate t_{2g}-levels and cubic hopping with t_π=−150 meV were used, like in table 14. The values of the exchange-coupling constants for $J/U = 0.64/5 = 0.13$ are those listed in table 11 as J^{Δ}_{se}.

cubic hopping and uses the eigenvector of the lowest crystal-field state $|1\rangle$ in $YTiO_3$. Since equation (37) is general, we can use it also for "cubic" $LaTiO_3$. In table 14 we have therefore listed the hopping integrals obtained by applying our crystal-field transformations (19) and (20) to *cubic hopping* with $t_\pi \equiv -150$ meV. In this case, the difference between $LaTiO_3$ and $YTiO_3$ stems exclusively from the different crystal-field eigenvectors. The differences with the *ab initio* values of the hopping integrals listed in table 11 are seen to be large, although some of the trends are captured by the *ab initio* crystal-field eigenvectors. From the values of τ and $(J/U)_0$, we realize that,

although both "cubic materials" are antiferromagnetic, as claimed in [40], $YTiO_3$ does have a tendency to couple ferromagnetically in the plane. The calculation for the cubic titanates is included as the top panel of figure 24.

If we finally take cubic hoppings, as well as the simplified eigenvector (40) for $LaTiO_3$ and (41) for $YTiO_3$, these then being the only difference between the two materials, we obtain the results shown in table 15. Both "materials" are fairly isotropic, G-type antiferromagnets with the exchange coupling two times larger in $LaTiO_3$ than in $YTiO_3$.

In conclusion, the sign of the super-exchange coupling that we calculate using conventional theory and LDA t_{2g} Wannier functions is consistent with the observed magnetic ground states of $LaTiO_3$ and $YTiO_3$. The mechanism by which the different magnetic orders come out of the calculations is through orbital order caused by the Coulomb repulsion and a strong crystal-field, and through distortion of the cubic hopping integrals. Both the crystal field and the modification of the hopping integrals are caused by the $GdFeO_3$-type distortion. The fact that we can explain *both* the Mott gap *and* the observed magnetic order from the orbital order and hopping integrals calculated without adjustable parameters with the LDA, seems to rule out the orbital-liquid scenario for the t_{2g}^1 titanates.

The discrepancies between experiment and computation do deserve further investigation, however.

The size of our J_{se}^{001} exchange-coupling for $YTiO_3$ agrees with the experimental values, but the anisotropy is too large. Due to the near-cancellation of terms, the calculated exchange coupling constants are very small, as they should be in order to account for the low Curie temperature, but this also makes them sensitive to detail. For instance, the values of our calculated 2nd-nearest-neighbour constants, $J_{se}^{011/101} = +0.2$ meV, $J_{se}^{01\bar{1}/10\bar{1}} = +0.3$ meV, $J_{se}^{110} = +0.5$ meV, and $J_{se}^{1\bar{1}0} = +0.2$ meV, are *anti*ferromagnetic and *not* negligible compared with the 1st-nearest-neighbour values in table 11. We shall see a further example of this sensitivity in section 6.3, where we consider the influence of the JT distortion. Moreover, the computational inaccuracies mentioned in appendix B may influence these delicate exchange-coupling constants.

For $LaTiO_3$, our exchange couplings in table 12 are isotropic, but three times smaller than the experimental values. In this case, our calculated 2nd-nearest-neighbour constants, $J_{se}^{011/101} = -0.2$ meV, $J_{se}^{01\bar{1}/10\bar{1}} = -0.1$ meV, $J_{se}^{110} = +0.9$ meV, and $J_{se}^{1\bar{1}0} = 0$ meV, are small in comparison with the 1st-nearest-neighbour values. Also the computational inaccuracies mentioned in appendix B are presumably too small to explain this discrepancy.

In general, one suspects that the LDA overestimates covalency. If that would cause the scale of our hopping integrals to be too large, our value of U chosen to account for the Mott transition would also be too large in order to compensate for this, but then our t^2/U should be too large – but, in fact, the opposite seems to be true for $LaTiO_3$. Nevertheless, since our hopping integrals result from a delicate balance between Ti-O, Ti-Ti, A-O, and Ti-A covalencies as seen in sections 3.3, 3.4, and 3.7, the degree to which

the LDA gets this balance right is decisive for the accuracy of the calculated exchange couplings. To check this further, calculations with other density functionals are needed, and so are experiments to test the implications of the strong cation covalency predicted by our [21] and earlier model calculations [24, 26].

Another reason for the factor-three discrepancy in $LaTiO_3$ could be that the e_g degrees of freedom should have been treated explicitly because, as was pointed out by Mochizuki and Imada [27], the energy of the e_g band is merely a few times $2J$ above that of the t_{2g} band (see figure 4). However, not fully treating the e_g degrees of freedom should lead us to underestimate the tendency towards ferromagnetism – a problem that we do not have for $LaTiO_3$. Besides, if we were to include the e_g degrees of freedom in the Hubbard model, we could do so by adding the space of the Wannier functions for the e_g band to the space of Wannier functions for the t_{2g} band, because with this choice the Wannier orbitals and, hence, the parameter values for the t_{2g} band would be unchanged. But in this d basis there is no single-particle coupling between the t_{2g} and e_g subspaces, and therefore no coupling in the 2nd-order perturbation expression (34). As a result, our super-exchange calculation in which only the t_{2g} degrees of freedom are treated and the e_g- as well as all other single-particle channels are downfolded, is correct.

The factor-three discrepancy might be related to the fact that the magnetic moment in $LaTiO_3$ is anomalously small ($0.57\,\mu_B$). Our assumption of complete orbital order and subsequent use of 2nd-order perturbation theory are clearly insufficient if the orbitally-ordered state changes at low temperature. A future spin-polarized LDA+DMFT calculation should allow us to calculate the magnetic moment and to keep full account of the inter-site coupling between spin and orbital degrees of freedom. For a general discussion of the why the magnetic moment is so small in $LaTiO_3$, we refer to reference [29].

Finally, it is possible that in these t_{2g} materials with strong A covalency the eigenvectors of the density matrix calculated more accurately than in the single-site DMFT differ sufficiently from those of the crystal-field Hamiltonian to influence the exchange-coupling constants.

6.3. Influence of the JT distortion in $YTiO_3$

We have found that the JT distortion in $YTiO_3$ does not create, but merely reflects the orbital order driven by the Coulomb correlations and controlled by the $GdFeO_3$-type distortion through the crystal field set up by the A ions. Mochizuki and Imada [29] now speculated that for strongly $GdFeO_3$-distorted materials like $YTiO_3$, where the magnetism is weak, the JT distortion could be a controlling factor for the *magnetic* order. This we now investigate.

Using the LDA Hamiltonian (table 7) computed for our hypothetical $YTiO_3$ without JT distortion, we obtain the hopping integrals and exchange couplings given in table 16: $J_{se}^{001} = -3.0$ meV and $J_{se}^{100/010} = +2.5$ meV. This gives ferromagnetic order along z and

Table 16. t_{1m}^{xyz} and J_{se} in meV.

	$YTiO_3$ without JT distortion						$YTiO_3$ at 15.9 GPa					
xyz	001		010		100		001		010		100	
$1,m$	t_{1m}	J_{se}	t_{1m}	J_{se}	t_{1m}	J_{se}	t_{1m}	J_{se}	t_{1m}	J_{se}	t_{1m}	J_{se}
1, 1	−23	0.4	−104	8.9	−104	8.9	−87	6.2	11	0.1	11	0.1
1, 2	52	−0.5	−200	−7.6	−47	−0.4	−15	0.0	−253	−12.2	−22	−0.1
1, 3	123	−2.9	−24	−0.1	157	−4.7	81	−1.3	−41	−0.3	130	−3.2
J_{se}		−3.0		1.2		3.8		4.9		−12.4		−3.2
τ		4.11				1.25		0.67				13.1
$\left(\frac{J}{U}\right)_0$		0.03				0.15		0.25				0.00

antiferromagnetic order in the plane, that is, C-type antiferromagnetism and, hence, a completely different result than obtained for the proper structure.

For the high-pressure phase observed by Loa *et al.* to have strongly reduced JT distortion, but slightly increased $GdFeO_3$-type distortion, we find the results given in the right-hand side of table 16: $J_{se}^{001} = +4.9$ meV and $J_{se}^{100/010} = -7.8$ meV. This causes a third kind of ground state with robust antiferromagnetic order along z and ferromagnetic order in the plane: a type-A antiferromagnet.

In conclusion, our *ab initio* calculations support the speculation of Mochizuki and Imada [29] that, although not very important for the orbital order, the JT distortion *is* of crucial importance for the magnetic order in $YTiO_3$. This should be tested experimentally.

7. Unfolding the orthorhombic band

In this paper we have first seen three degenerate, independent, and nearly two-dimensional cubic bands develop into twelve inequivalent and coupled orthorhombic bands, which narrow down and develop a pseudo-gap under increasing $GdFeO_3$-type distortion (figures 3, 10, 17, and 18). In order to treat the Coulomb correlations, we have constructed a set of highly localized t_{2g} Wannier functions for these bands and have defined the corresponding Hubbard Hamiltonian. With this set of Wannier functions, the splitting of the lower t_{2g} levels reaches a mere 10% of the bandwidth, but this, together with the 30% decrease of the entire bandwidth through the series (table 8) is important for determining where in the series the Mott transition occurs (table 10). However, U_c'/W decreases by 50% when going from $SrVO_3$ to $YTiO_3$, and that is significantly more that the ∼30% which can be gained by a crystal-field induced decrease of the effective degeneracy from 3 to 1. Therefore, the width of the lowest

subband must decrease faster than the width of the entire t_{2g} band.

A second surprising result of the LDA+DMFT calculations was that once U' exceeds $\sim W$, the eigenvectors of the density matrix are essentially the same as those of the on-site LDA Hamiltonian, and as $U' \approx U'_c$, the orbital fluctuations become strongly suppressed. As a result, only the orbital of lowest energy is occupied in $LaTiO_3$ and $YTiO_3$. As seen in figure 21, the $\langle 1\,|\varepsilon|\,1\rangle$ element of the spectral function is divided into a lower occupied and a higher unoccupied Hubbard band, while the diagonal elements of the higher orbitals, $\langle 2\,|\varepsilon|\,2\rangle$ and $\langle 3\,|\varepsilon|\,3\rangle$, have weight almost exclusively in the upper, unoccupied Hubbard band. The off-diagonal elements, $\langle 1\,|\varepsilon|\,2\rangle$, $\langle 2\,|\varepsilon|\,3\rangle$, and $\langle 1\,|\varepsilon|\,3\rangle$, are completely negligible. We thus found orbital order, particularly in $YTiO_3$. Our conclusion of those two findings was that the self-energy must behave in the way explained around equations (31) and (32).

In section 6 we found that the increasing tendency towards ferromagnetic coupling is due to the increasing strength of the hopping in the orbitally ordered state from the lowest crystal-field orbital to the higher orbitals on the neighbouring sites, compared with that of the hopping between the lowest orbitals. This is what the ratio τ given in tables 11–16 measures. Increasing τ, of course, tends to decrease the width of band 1.

What remains unexplained is the 50% effect brought out by table 10 or, in other words, why for merely $U' \geq 1.6W$ in $LaTiO_3$ and $1.3W$ in $YTiO_3$ the lower half of *one* band (per Ti) – considerably more narrow than W – lies below the bottom of the others, and why this band has pure LDA crystal-field character $|1\rangle$. In figure 17 it is hard to identify such four orthorhombic LDA bands with $|1\rangle$ character. That is, the orthorhombic LDA bands display little tendency towards symmetry breaking. Nevertheless, we shall now demonstrate that behind the LDA pseudo-gap in the orthorhombic $GdFeO_3$-distorted perovskites there *is* a real gap. This gap is a direct one in a *pseudo-cubic* $\mathbf{k}$ space where it splits off the lowest t_{2g} band.

The way we arrived at this result was, first, to see whether with the NMTO method we could produce *one* Wannier function which describes the four lowest orthorhombic bands and has the character of the lowest crystal-field orbital. The result of this attempt is demonstrated in figure 25. The dashed black bands are the correct LDA bands, as obtained with a large NMTO basis set, and the 4 red bands are obtained with a *truly minimal* NMTO *basis set* containing only *one* t_{2g} orbital per site, the one with the symmetry of the lowest crystal-field orbital, *i.e.* with the eigenvector $|1\rangle$ defined in equations (19) and (20) for $LaTiO_3$ and $YTiO_3$, respectively. Since this orbital is *not* the partner of two other t_{2g} orbitals, which together with it would span the entire t_{2g} band, the $|2\rangle$ and $|3\rangle$ characters (figure 14) are downfolded into the tail of this new, *extended* $|1\rangle$ orbital, which we shall name $|\mathrm{I}\rangle$ and show in figure 26. Moreover, the energy mesh of $|\mathrm{I}\rangle$ was chosen to span only the occupied part of the t_{2g} band. The blue bands in figure 25 are obtained from *another* truly minimal NMTO *basis set* with *two* t_{2g} orbitals per site, $|\mathrm{II}\rangle$ and $|\mathrm{III}\rangle$, with respectively $|2\rangle$ and $|3\rangle$ character, and with $|1\rangle$ downfolded in the tails. Its energy mesh is mostly in the empty part of the t_{2g} band (appendix A). The marvel is that orbital $|\mathrm{I}\rangle$ picks 4 of the 12 t_{2g} bands, that orbitals $|\mathrm{II}\rangle$ and $|\mathrm{III}\rangle$

Table 17. H^{LDA} in meV for $LaTiO_3$ [12].

xyz	000	001	010	100	011	$10\bar{1}$	$01\bar{1}$	101	110	$1\bar{1}0$	111	$11\bar{1}$	$\bar{1}11$	$1\bar{1}1$
m',m														
I,I	9	156	−60	−60	−31	−31	−25	−25	−46	−38	−10	−10	−15	−15
II,II	748	116	31	31	−2	−2	−16	−16	6	16	7	7	−1	−1
III,III	716	102	−101	−101	29	29	38	38	−24	−23	9	9	12	12
II,III	14	11	−21	10	5	−26	−10	−26	−55	−34	−10	14	3	14
III,II	14	11	10	−21	−26	5	−26	−10	−55	−34	14	−10	14	3

002	020	200	$2\bar{1}0$	$\bar{1}20$	102	012	$0\bar{1}2$	$\bar{1}02$	201	$\bar{2}01$	$02\bar{1}$	021	210	120
−33	−55	−30	4	4	−2	−2	−7	−7	−12	−12	42	42	−5	−5
0	−1	82	−18	−18	−9	−9	0	0	−24	−24	−3	−3	−14	−14
31	5	−13	2	2	−2	−2	1	1	10	10	−5	−5	5	5
10	−1	−6	0	−7	1	1	5	13	8	4	8	2	0	−4
10	−1	−6	−7	0	1	1	13	5	4	8	2	8	−4	0

Table 18. H^{LDA} in meV for $YTiO_3$.

xyz	000	001	010	100	011	$10\bar{1}$	$01\bar{1}$	101	110	$1\bar{1}0$	111	$11\bar{1}$	$\bar{1}11$	$1\bar{1}1$
m',m														
I,I	−38	62	−39	−39	−7	−7	−24	−24	−39	−11	−9	−9	7	7
II,II	674	44	−20	−20	7	7	1	1	46	54	0	0	−12	−12
III,III	706	127	−58	−58	10	10	−9	−9	−48	−60	17	17	6	6
II,III	59	22	5	30	−3	−22	−14	−20	−9	−12	−20	10	2	0
III,II	59	22	30	5	−22	−3	−20	−14	−9	−12	10	−20	0	2

002	020	200	$2\bar{1}0$	$\bar{1}20$	102	012	$0\bar{1}2$	$\bar{1}02$	201	$\bar{2}01$	$02\bar{1}$	021	210	120
−35	−60	−32	5	5	1	1	0	0	−14	−14	32	32	−14	−14
−15	−11	59	−4	−4	−9	−9	−11	−11	−10	−10	−8	−8	9	9
25	−8	6	−9	−9	−1	−1	8	8	0	0	1	1	−7	−7
13	−4	49	−8	−19	8	−5	−3	13	−17	−14	12	5	−20	−10
13	−4	49	−19	−8	−5	8	13	−3	−14	−17	5	12	−10	−20

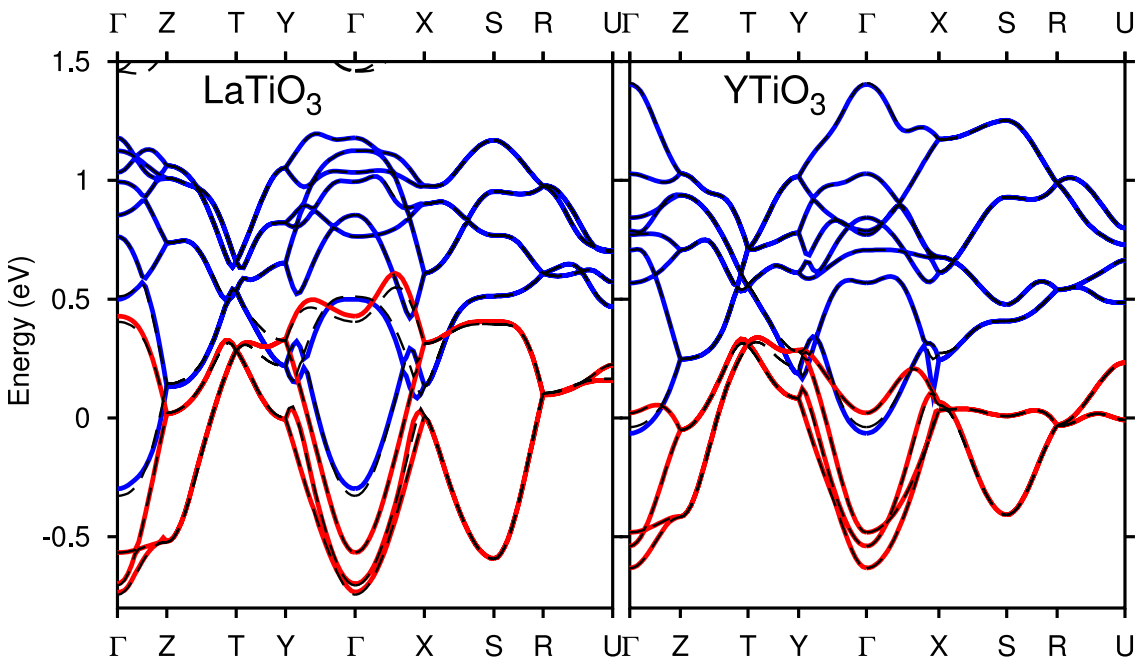

Figure 25. LDA bands obtained with a large NMTO basis set (dashed black) and with truly minimal sets, downfolded to respectively the lowest t_{2g} crystal-field orbital $|\mathrm{I}\rangle$ (red) and the two highest crystal-field orbitals $|\mathrm{II}\rangle$ and $|\mathrm{III}\rangle$ (blue). The following NMTO energy meshes were used: for the $LaTiO_3$ red bands $\epsilon_n = -0.55$, -0.45, and 0.04 eV, and for the blue bands $\epsilon_n = -0.94$, 0.70, 1.11 and 1.17 eV. For $YTiO_3$, $\epsilon_n = -0.25$, -0.12, and 0.40 eV for the red bands, and $\epsilon_n = -0.80$, 0.70, 1.04, 1.31, and 1.65 eV for the blue bands.

together pick the remaining 8 t_{2g} bands, and that the 4th band near Γ is the lowest of the blue bands and has exclusively $|\mathrm{III}\rangle$ character. The fact that such a decomposition of the bandstructure is possible is not trivial, at least not from the point of view of the orthorhombic bands. Since all the LDA Bloch states are orthonormal, so are the three extended crystal-field Wannier functions, to the extent that they span the LDA bands, and –as figure 25 demonstrates– they do this with good accuracy.

Comparison of the bands in figure 25 with the ones decorated with the local 1,2,3 characters in figure 17 confirms that band I picks four low bands with dominant 1-character. The orbital which describes those four bands has 1-character in its head and the minority characters 2 and 3 in its tail, on the neighbouring Ti sites. The way in which it acquires a low energy is for a given neighbour to pick that linear combination of orbitals 2 and 3 which provides the *same* orientation of the oxygen p function to be shared, and then to add this linear combination with the *opposite* phase and an appropriate amplitude. In this way, the resulting oxygen p function will *bond* with the Ti characters on the neighbours.

The Hamiltonian for band I and the one for bands II and III are now orthonormalized and Fourier transformed. The resulting on-site and hopping matrix

elements are given in tables 17 and 18. Remember that, by virtue of our NMTO construction, there is no LDA interaction between orbital I and the two other orbitals. We note that the splitting between level I and the nearly degenerate levels II and III is huge, 0.7 eV. The bands have therefore really been separated and what we have is extreme orbital order at the LDA level. For $LaTiO_3$ ($YTiO_3$), the energy of orbital I has been lowered by 0.35 (0.30) eV from that of orbital 1, and the energies of orbitals II and III have been raised from those of orbitals 2 and 3 by, in total, the same amount. This has been achieved by adding to orbital 1 *bonding* 2- and 3-characters at the neighbouring sites, as was mentioned above, and by adding to orbitals 2 and 3 *antibonding* 1-character at the neighbours. It is therefore also obvious that we have got rid of inter-orbital hopping at the expense of inter-site Coulomb repulsion and Hund's-rule coupling, without which the ferromagnetism of $YTiO_3$ cannot be explained. For the set of extended crystal-field orbitals, the Fermi level almost coincides with the lowest level; it is slightly below in $LaTiO_3$ and a bit above in $YTiO_3$. This is because the 4th band at Γ (band III) dips deeper below the Fermi level in $LaTiO_3$ than in $YTiO_3$.

One might argue that these Wannier orbitals are far too extended to be of any use for describing correlated electrons. The way to think about these orbitals is, however, as the initial, Σ=0 orbitals in a self-consistent LDA+DMFT approach like the one recently suggested [51]. As self-consistency is approached, the self-energy will separate the bands and the extended Wannier orbitals will localize so that $|\mathrm{I}\rangle \rightarrow |1\rangle$, $|\mathrm{II}\rangle \rightarrow |2\rangle$, and $|\mathrm{III}\rangle \rightarrow |3\rangle$. So what the initial orbitals do is to tell us in which way, if any, "the chemistry" wants to break the symmetry. In the present case of t_{2g}^1 titanates, it is clear that the chemistry tells us that we have *one* half-filled band, rather than three degenerate $\frac{1}{6}$-full bands. For this one band the DMFT will finally create a self-energy which will separate it into a lower and an upper Hubbard band, provided that the width of this band is sufficiently small.

For orbital I, the 1st-nearest neighbour hopping integral perpendicular to the mirror plane is positive, while those parallel to the plane are negative, and merely half the size. Moreover, the hopping integrals in $YTiO_3$ are half the size of those in $LaTiO_3$. A way to analyze the hoppings would be to express $|\mathrm{I}\rangle$ as a linear combination of $|1\rangle$, $|2\rangle$, and $|3\rangle$ on the same site and on the 6 neighbour sites. This would, for instance, explain why the hopping is twice as strong in the z direction as in the parallel direction, despite the fact –obvious from figure 26– that the orbital is most extended in the y direction and least in the z direction. As we have experienced before, hopping integrals are sums of terms with alternating signs.

For $LaTiO_3$ and $YTiO_3$ we have thus succeeded in decoupling *one* orbital and in removing the coupling between the two other orbitals approximately. The consequence of this is that we can *fold* the band structure *out* in a *pseudo-cubic* Brillouin zone (see figures 2 and 9). The reason is that the group of covering operations for a *single* orbital on the B sites is *cyclic,* provided that the orbital is defined as in the *bottom* row of figure 8. As a result, we can now let $\exp i\mathbf{k}\cdot\mathbf{R}$ be the irreducible representations of this cyclic group with $\mathbf{R}$ being primitive monoclinic translations. The meaning of $\mathbf{k}$ in the large,

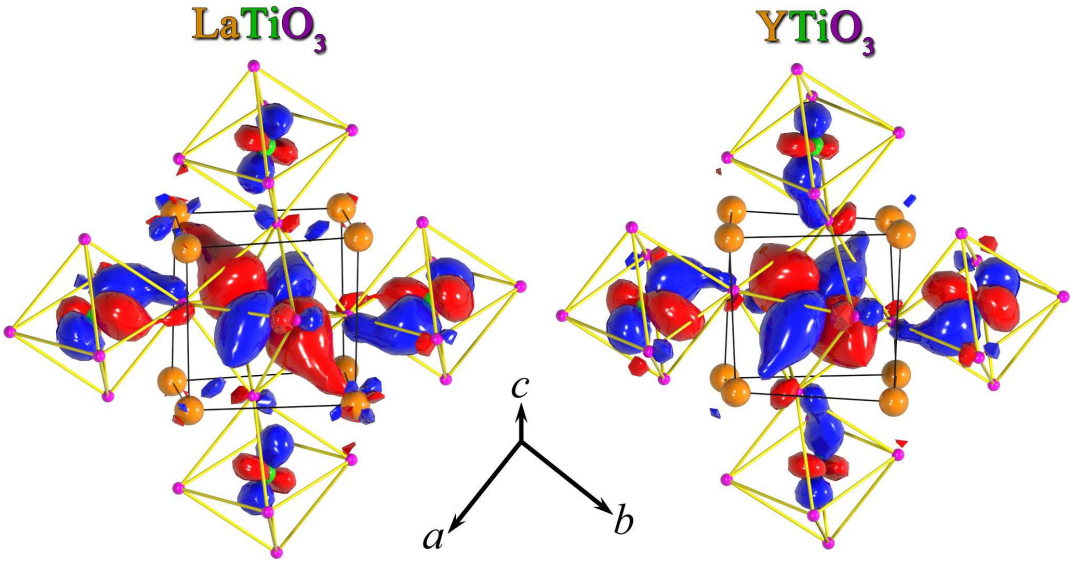

Figure 26. Extended crystal-field NMTO |I⟩ spanning the red LDA bands of figure 25 and with the same local character as |1⟩ in figure 14Compared with that figure, the present viewpoint is more from the top, looking down on a mirror-plane. The central part of the orbital is in subcell 1 000 and the rest is in subcells 2: 010 to the left and right, and 100 up and down. The amplitude in subcell 3 001 is smaller and has been truncated for the sake of clarity. The contour is the same as in figure 14. This orbital (before orthogonalization) has 63% of its charge density on the central A_8BO_6 unit, and this holds for both titanates. When moved to the neighbouring Ti sites, this orbital follows the space-group symmetry, like orbital |1⟩ in figure 16 (orbital order).

primitive monoclinic BZ is thus different from that in section 3.6, where we combined the B-centred orbitals, $|\mathbf{R}, m\rangle$, into Bloch sums following the middle-row convention of figure 8. In the present, so-called *pseudo-cubic* scheme, we still use equations (8) and (9), but there is only a single orbital shape, $|\mathbf{R}\rangle$, and there will be *no* coupling between the four **Q** vectors.

For band I of $LaTiO_3$ and $YTiO_3$ the unfolding is demonstrated in figure 27. For a single orbital, the band dispersion is given by equation (1), an amazingly simple result considering the complicated orthorhombic bandstructures at the bottom of figure 27, not to speak of figure 10. Since the dominating nearest-neighbour hopping integral, t^{001}, is positive and the perpendicular ones, t^{010}=t^{100}, are negative, the bottom of the band is at 00π and the top is in the k_z=0 plane near $\pi\pi0$ and $\pi00$. This may seem unfamiliar, but is related to the necessity of using the orbital-order convention at the bottom row of figure 8 instead of the physical convention in the middle row. We shall return to this later when we consider the cubic t_{2g} bands

In figure 28 we include the hybridized bands II and III, this time in the orthorhombic zone because the hybridization cannot be folded out. The result is the dashed black band structure, which is the t_{2g} band structure, but with all hops longer than to the 120 neighbours truncated. The red band structure is that of band I, which is identical

to the four lowest black bands, and to the bands in the bottom panel of figure 27. The green and blue bands are, respectively, the unhybridized bands II and III, and they are seen to be reasonably accurate below, and up to 0.3 eV above, the Fermi level.

With the hybridization between bands II and III neglected, also these bands may be folded out: all three bands are then given by equation (1), and they are shown in figure 29. We see that the lowest band is separated from the two others by a direct gap. Hence, the *pseudo-gap* is a real gap in pseudo-cubic **k** space, but with the lowest and the upper bands overlapping in energy.

Before continuing the discussion, let us first explain how the pseudo-gap arises under increasing $GdFeO_3$-type distortion. This we did in section 3.6 by using conventional **Q** coupling and considering the orthorhombic S_o point. Now, we want to use the pseudo-cubic **k** representation and connect back to the cubic limit, with its three degenerate, non-interacting, two-dimensional bands. That limit is given in the bottom row of figure 29, where we used the 2nd-nearest-neighbour model (2) with $t_\delta = 0$. However, the pseudo-cubic representation is valid only if we neglect hybridization between the three Bloch waves defined *with orbital order* (bottom row of figure 8). This means that we first have to break the cubic symmetry and prepare the cubic bands for the $GdFeO_3$-type distortion. In other words, we have to pick band I, and this will of course be the xy band because this is the band for which the orbital order does not break the physical coupling (for xy, the bottom and middle-row definitions in figure 8 are the same). The k_x, k_y dispersion is thus given by equation (2), also in the pseudo-cubic zone; this is the red band in figure 29. With $t_\delta = 0$, this band has no k_z dispersion and its minimum is at $00k_z$, the saddle-points at $\pi 0 k_z$ and $0\pi k_z$, and the maximum at $\pi\pi k_z$. The bandwidth is $8\,|t_\pi|$, and with increasing $t'_\sigma/t_\pi \equiv r$, the energy of the saddle-points shifts away from the minimum towards the maximum, *i.e.* the lower part of the band is stretched. The value of r chosen for the figure is that of $SrVO_3$, whose cubic band structure was shown along the same path in figure 11. Moreover, $t_\pi = -250$ meV, which is numerically a bit smaller than that of $SrVO_3$, but is like those of $CaVO_3$.

Next, we consider the yz and xz bands. Lets us be pedagogical and perform their unfolding explicitly. The hopping Hamiltonian in the *four-site orthorhombic* Bloch representation is given by:

$H/(2\,\lvert t_\pi\rvert)$	$yz\,(1)$	$xz\,(2)$	$-yz\,(3)$	$-xz\,(4)$	$xz\,(1)$	$yz\,(2)$	$-xz\,(3)$	$-yz\,(4)$
$yz\,(1)$	0	0	c_z	0	0	$-c_y$	0	$2rc_yc_z$
$xz\,(2)$	0	0	0	c_z	$-c_x$	0	$2rc_xc_z$	0
$-yz\,(3)$	c_z	0	0	0	0	$2rc_yc_z$	0	$-c_y$
$-xz\,(4)$	0	c_z	0	0	$2rc_xc_z$	0	$-c_x$	0
$xz\,(1)$	0	$-c_x$	0	$2rc_xc_z$	0	0	c_z	0
$yz\,(2)$	$-c_y$	0	$2rc_yc_z$	0	0	0	0	c_z
$-xz\,(3)$	0	$2rc_xc_z$	0	$-c_x$	c_z	0	0	0
$-yz\,(4)$	$2rc_yc_z$	0	$-c_y$	0	0	c_z	0	0

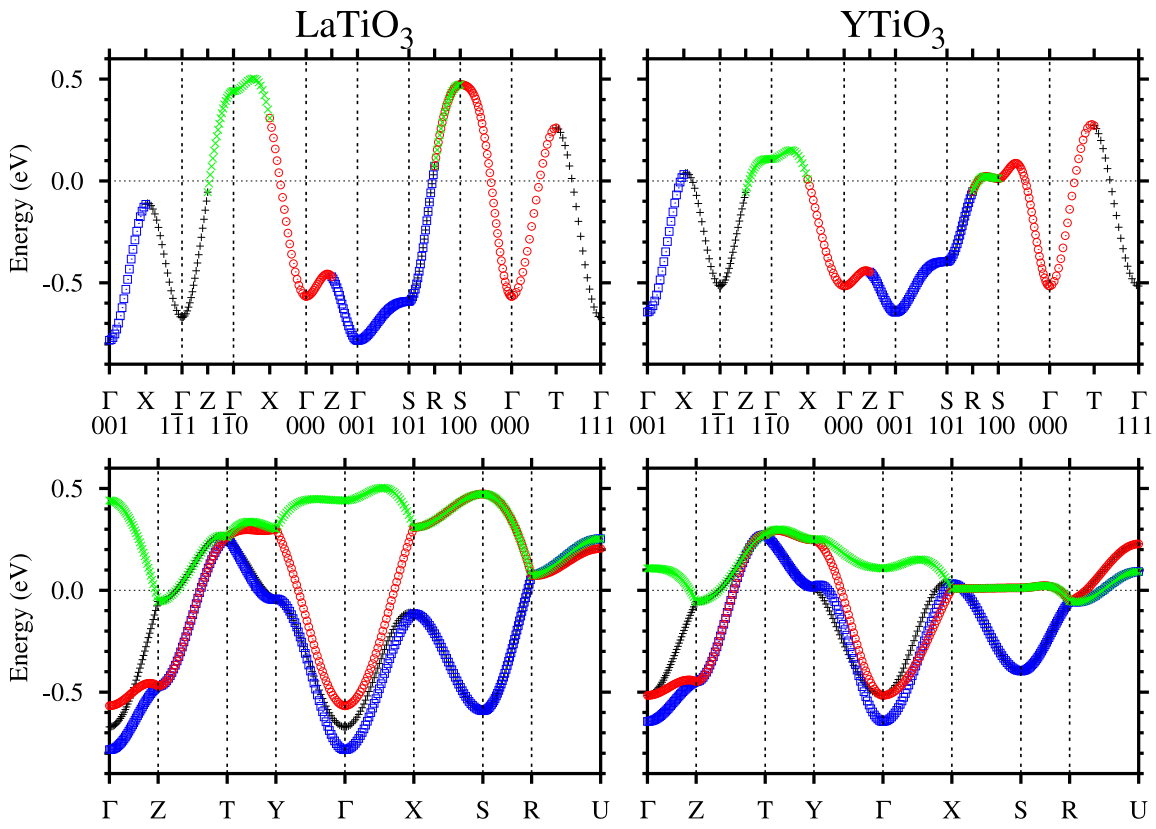

Figure 27. Folding band I out from the orthorhombic (bottom) to the pseudo-cubic BZ (top). See figure 9. In the orthorhombic zone with 4 sites, **R**, the eigenvectors are $\frac{1}{2}\exp i\mathbf{Q}\cdot\mathbf{R}$ with $\mathbf{Q} = 000$ (red), 00π (blue), $\pi\pi 0$ (green), and $\pi\pi\pi$ (black). The unit along the abscissa is π. The bands were produced using tables 17 and 18. The pseudo-cubic bands are given by equation (1). The letters denote high-symmetry points in the orthorhombic BZ and the path taken along the simple monoclinic BZ is the same as in figure 11, but the pseudo-cubic **k** includes the orbital order.

where the rows and columns have been ordered so that the first 4 Bloch waves belong to the middle, and the last 4 Bloch waves to the right column in the bottom row of figure 8. After the unitary transformation (9), $H/\left(2\left|t_\pi\right|\right)$ becomes:

$yz(000)$	$xz(00\pi)$	$-yz(\pi\pi 0)$	$-xz(\pi\pi\pi)$	$xz(000)$	$yz(00\pi)$	$-xz(\pi\pi 0)$	$-yz(\pi\pi\pi)$
c_z	0	0	0	$-(1-2rc_z)u$	0	$-(1-2rc_z)v$	0
0	$-c_z$	0	0	0	$-(1+2rc_z)u$	0	$-(1+2rc_z)v$
0	0	c_z	0	$(1-2rc_z)v$	0	$(1-2rc_z)u$	0
0	0	0	$-c_z$	0	$(1+2rc_z)v$	0	$(1+2rc_z)u$
$-(1-2rc_z)u$	0	$(1-2rc_z)v$	0	c_z	0	0	0
0	$-(1+2rc_z)u$	0	$(1+2rc_z)v$	0	$-c_z$	0	0
$-(1-2rc_z)v$	0	$(1-2rc_z)u$	0	0	0	c_z	0
0	$-(1+2rc_z)v$	0	$(1+2rc_z)u$	0	0	0	$-c_z$

,

where for simplicity of notation we have defined

$$u \equiv \frac{1}{2}\left(c_x + c_y\right), \quad \text{and} \quad v \equiv \frac{1}{2}\left(c_x - c_y\right).$$

Along the diagonal we only have the k_z dispersion, as is also obvious from the bottom row of figure 8. We may, however, get rid of the off-diagonal elements proportional to u by transformation to

$$|\mathrm{III}\rangle = \frac{1}{\sqrt{2}}\left(|yz\rangle - |xz\rangle\right) \quad \text{and} \quad |\mathrm{II}\rangle = \frac{1}{\sqrt{2}}\left(|yz\rangle + |xz\rangle\right),$$

where $|yz\rangle$ and $|xz\rangle$ now refer to subcell 1, or, equivalently, follow the notation of the bottom row in figure 8. This yields a block-diagonal Hamiltonian with the following four blocks:

$$\begin{array}{|cc|}\hline \mathrm{II}\,(000,\mathbf{k}) & \mathrm{III}\,(\pi\pi 0,\mathbf{k}) \\ & \\ \varepsilon\,(\mathbf{k}-\pi\pi\pi) & \delta\,(\mathbf{k}-\pi\pi\pi) \\ \delta\,(\mathbf{k}-\pi\pi\pi) & \varepsilon\,(\mathbf{k}-\pi\pi\pi) \\ \hline \end{array}, \quad \begin{array}{|cc|}\hline \mathrm{II}\,(\pi\pi 0,\mathbf{k}) & \mathrm{III}\,(000,\mathbf{k}) \\ & \\ \varepsilon\,(\mathbf{k}-00\pi) & \delta\,(\mathbf{k}-00\pi) \\ \delta\,(\mathbf{k}-00\pi) & \varepsilon\,(\mathbf{k}-00\pi) \\ \hline \end{array}, \tag{42}$$

$$\begin{array}{|cc|}\hline \mathrm{II}\,(00\pi,\mathbf{k}) & \mathrm{III}\,(\pi\pi\pi,\mathbf{k}) \\ & \\ \varepsilon\,(\mathbf{k}-\pi\pi 0) & \delta\,(\mathbf{k}-\pi\pi 0) \\ \delta\,(\mathbf{k}-\pi\pi 0) & \varepsilon\,(\mathbf{k}-\pi\pi 0) \\ \hline \end{array}, \quad \begin{array}{|cc|}\hline \mathrm{II}\,(\pi\pi\pi,\mathbf{k}) & \mathrm{III}\,(00\pi,\mathbf{k}) \\ & \\ \varepsilon\,(\mathbf{k}) & \delta\,(\mathbf{k}) \\ \delta\,(\mathbf{k}) & \varepsilon\,(\mathbf{k}) \\ \hline \end{array}, \tag{43}$$

where according to equation (2),

$$\begin{aligned} \varepsilon\,(\mathbf{k}) &\equiv \frac{1}{2}\left[\varepsilon_{yz}\,(\mathbf{k}) + \varepsilon_{xz}\,(\mathbf{k})\right] = 2t_\pi\left(u + c_z\right) + 4t'_\sigma u c_z, \\ \delta\,(\mathbf{k}) &\equiv \frac{1}{2}\left[\varepsilon_{yz}\,(\mathbf{k}) - \varepsilon_{xz}\,(\mathbf{k})\right] = -2t_\pi\left(1 + 2rc_z\right)v, \end{aligned}$$

are, respectively, the average and half the difference of the yz and xz band dispersions with $\mathbf{k}$ in the orthorhombic zone. The eight yz and xz bands are thus obtained by hybridization between pairs of degenerate average bands, $\mathrm{II}\,(\mathbf{Q},\mathbf{k})$ and $\mathrm{III}\,(\mathbf{Q}+\pi\pi 0,\mathbf{k})$. There exists such a pair of hybridized bands, $\varepsilon_{yz}\,(\mathbf{k}-\mathbf{Q})$ and $\varepsilon_{xz}\,(\mathbf{k}-\mathbf{Q})$, for each of the four $\mathbf{Q}$ vectors. These are 8 of the 12 bands seen in figure 11 for $SrVO_3$, and the remaining 4 are the $\varepsilon_{xy}\,(\mathbf{k}+\mathbf{Q})$ bands. Note that the $\varepsilon_{x_ix_j}\,(\mathbf{k})$ and $\varepsilon_{x_ix_j}\,(\mathbf{k}-\mathbf{Q})$ bands are degenerate at the corresponding boundary of the orthorhombic BZ (red in figure 9).

The orthorhombic zone may now be folded out in the k_z direction because the 1st and 2nd Hamiltonians (43) are identical with, respectively, the 1st and 2nd Hamiltonians (42), if considered as functions of the wave vector $\vec{\mathbf{k}} \equiv \mathbf{k} + \mathbf{Q}_z$. If we therefore let the latter run over the orthorhombic zone *doubled* in the k_z direction, the Hamiltonians (43) should be dropped. This is *exact* for *any* band structure, and examination of any set of orthorhombic bands in this paper will reveal that they *can* be folded out along any vertical path, *i.e.* a pair of bands along $\Gamma_o Z_o$ can be folded out to one band along 000 – 00π, and similarly for $\mathrm{Y}_o\mathrm{T}_o \to \frac{\pi}{2}\frac{\pi}{2}0$ – $\frac{\pi}{2}\frac{\pi}{2}\pi$, and $\mathrm{S}_o\mathrm{R}_o \to \pi 00$ – $\pi 0\pi$. This is also the reason why all orthorhombic bands are at least 2-fold degenerate on the horizontal face

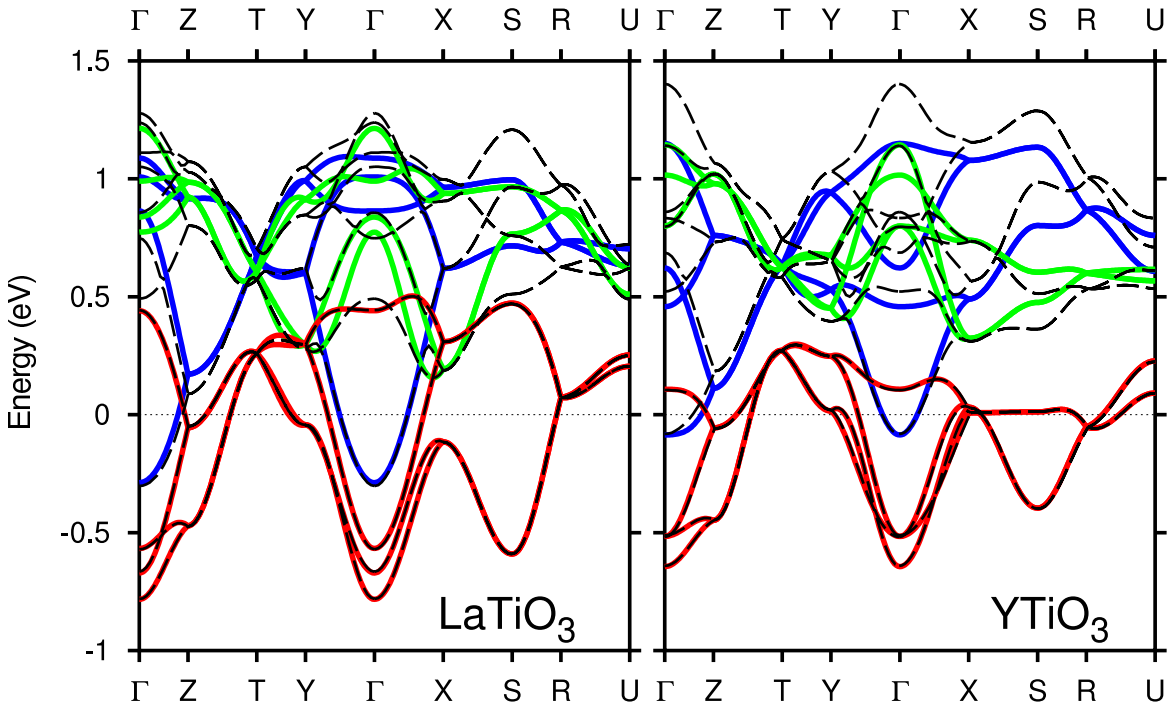

Figure 28. Hybridized (dashed black) and unhybridized I (red), II (green), and III (blue) bands produced from the on-site and hopping integrals in tables 17 and 18.

$k_z = \frac{\pi}{2}$. The cubic bands folded out to the double orthorhombic zone are the yz and xz bands (2) translated to $\pi\pi\pi$ and the same bands translated to 00π, as can be seen from the Hamiltonians (42).

Folding out to a pseudo-cubic BZ is *not* exact for a Hamiltonian, but only for a single band. Consider, *e.g.*, the cubic band Hamiltonians (42) as functions of the pseudo-cubic wave vector $\bar{\mathbf{k}} \equiv \vec{\mathbf{k}} + \mathbf{Q}_{xy} = \mathbf{k} - \mathbf{Q}$:

$$\begin{array}{|cc|}\hline \mathrm{II}\,(000,\mathbf{k}) & \mathrm{III}\,(\pi\pi 0,\mathbf{k}) \\ & \\ \varepsilon\left(\bar{\mathbf{k}}-\pi\pi\pi\right) & \delta\left(\mathbf{k}-\pi\pi\pi\right) \\ \delta\left(\mathbf{k}-\pi\pi\pi\right) & \varepsilon\left(\bar{\mathbf{k}}-00\pi\right) \\ \hline\end{array}\quad,\quad \begin{array}{|cc|}\hline \mathrm{II}\,(\pi\pi 0,\mathbf{k}) & \mathrm{III}\,(000,\mathbf{k}) \\ & \\ \varepsilon\left(\bar{\mathbf{k}}-\pi\pi\pi\right) & \delta\left(\mathbf{k}-00\pi\right) \\ \delta\left(\mathbf{k}-00\pi\right) & \varepsilon\left(\bar{\mathbf{k}}-00\pi\right) \\ \hline\end{array}\quad.$$

We have obviously succeeded in folding out the diagonal elements, but the *hybridization* cannot be folded out. In the pseudo-cubic zone, we have two bands, namely the average band, $\varepsilon\,(\mathbf{k})$, translated to the sites 00π and $\pi\pi\pi$. But there is no way in which these two bands can hybridize in the pseudo-cubic zone to yield the proper cubic bands. That can only occur after translation by $\pi\pi 0$, *i.e.* by returning to the double orthorhombic zone. Although important for nearly cubic bands, the neglected coupling between bands II and III causes no problem for the lowest $\frac{1}{3}$ of the t_{2g} band in the titanates. This must be so because we have succeeded in downfolding band I correctly with the NMTO method.

The cubic bands are given in the bottom part of figure 29. In red $\varepsilon_{xy}\left(\bar{\mathbf{k}}\right)$, in green $\varepsilon_{yz}\left(\bar{\mathbf{k}}-\pi\pi\pi\right)$ and $\varepsilon_{xz}\left(\bar{\mathbf{k}}-\pi\pi\pi\right)$, and in blue $\varepsilon_{yz}\left(\bar{\mathbf{k}}-00\pi\right)$ and $\varepsilon_{xz}\left(\bar{\mathbf{k}}-00\pi\right)$. These yz

and xz bands are degenerate, and therefore equal their respective averages, $\varepsilon\left(\bar{\mathbf{k}}{-}\pi\pi\pi\right)$ with wave function $yz + xz$ and $\varepsilon\left(\bar{\mathbf{k}}{-}00\pi\right)$ with wave function $yz - xz$, in the ($\pm$110) planes containing 00π, 000, $\pm\pi\pi0$, and $\pm\pi\pi\pi$.

In this pseudo-cubic representation we may now follow the development of the bands as a function of the $GdFeO_3$-type distortion. For this purpose it is helpful to use the orthorhombic labelling at the bottom of figure 29 to relate the simple pseudo-cubic bands to the cubically averaged bands in figure 11 and to the projected orthorhombic bands in figure 17. The pseudo-cubic bands of $CaVO_3$ are intermediate between those of the cubic 2nd-nearest neighbour model and those of $LaTiO_3$. Starting from the cubic bands, the 45 meV coupling between the yz and xz orbitals in $CaVO_3$ (table 2), produces a 90 meV gap between the green and blue bands at X_o $\frac{\pi}{2}\frac{-\pi}{2}\pi$, and similarly at Y_o $\frac{\pi}{2}\frac{\pi}{2}\pi$, just above the Fermi level. The couplings between the other pairs of orbitals are $\sim$30 meV and the 3-fold degenerate red-green-blue level at T_o $\frac{\pi}{2}\frac{\pi}{2}\frac{\pi}{2}$ splits well above ε_F. Along Γ_o 00π – S_o $\pi0\pi$ – R_o $\pi0\frac{\pi}{2}$ – S_o $\pi00$ there is a splitting between the red xy and the green band almost at the Fermi level, and at high energy there is a splitting of all three bands. Moreover, the xy-band is lowered by $\sim$70 meV due to the crystal-field splitting. Finally, going along Γ_o $\pi\bar{\pi}\pi$ – Z_o $\pi\bar{\pi}\frac{\pi}{2}$ – Γ_o $\pi\bar{\pi}0$ – X_o $\frac{\pi}{2}\frac{\bar{\pi}}{2}0$ – Γ_o 000 there is a red-blue, a green-blue, and a red-green splitting. Of these, the latter splitting between the xy and the $yz + xz$ bands is at the lowest energy. In conclusion, due to the coupling between the xy, yz, and xz orbitals in $CaVO_3$, there are small splittings (<100 meV) at the crossings of the cubic bands, and this separates off a lowest band. The top of this band is a red-green maximum between X_o $\frac{\pi}{2}\frac{\bar{\pi}}{2}0$ and Γ_o 000, and the corresponding width of the lowest band can be read from figure 10 or 17 as being 1.80 eV. This is substantially smaller than the t_{2g} bandwidth (2.45 eV) listed in table 8. Due to the sharp avoided crossings, the Wannier function for the lowest band in $CaVO_3$ has very long range and is certainly not a suitable basis for a Hubbard model.

We now go to the titanates, for which the red, green, and blue bands in figure 29 are the I, II, and III bands corresponding to the extended Wannier functions defined earlier in this section. The strongest nearest-neighbour hopping integral coupling between the xy, yz and xz orbitals (tables 4 and 5) has increased to 75 meV in $LaTiO_3$ and 83 meV in $YTiO_3$, and the avoided crossings at X_o $\frac{\pi}{2}\frac{\bar{\pi}}{2}\pi$, Y_o $\frac{\pi}{2}\frac{\pi}{2}\pi$, and T_o $\frac{\pi}{2}\frac{\pi}{2}\frac{\pi}{2}$ have increased correspondingly to 150 and 166 meV. This can be seen in figures 10 or 17, but not really in figure 29 where the truncation of the separate Fourier series (1) for the red and green bands has rounded off the avoided crossings. Moreover, as may be seen from figure 25, numerical truncations in the NMTO calculation of the extended Wannier functions also produce some error in the II+III Hamiltonian near sharp avoided crossings, most noticeably at X_o. Along Γ_o 000 – Z_o $00\frac{\pi}{2}$ – Γ_o 00π there is now a red-blue avoided crossing which was not noticed in the 2nd-nearest-neighbour model where the xy band neither disperses along k_z, nor couples to the yz and xz bands. As seen from figure 17, this avoided crossing is between bands I and III near Γ_o 00π. Here, band III is purely 3-like and much more dispersive in $LaTiO_3$ than in $YTiO_3$, and it also lies higher because the 1-3 crystal field splitting is 205 meV in $LaTiO_3$, but 330 meV in $YTiO_3$. These

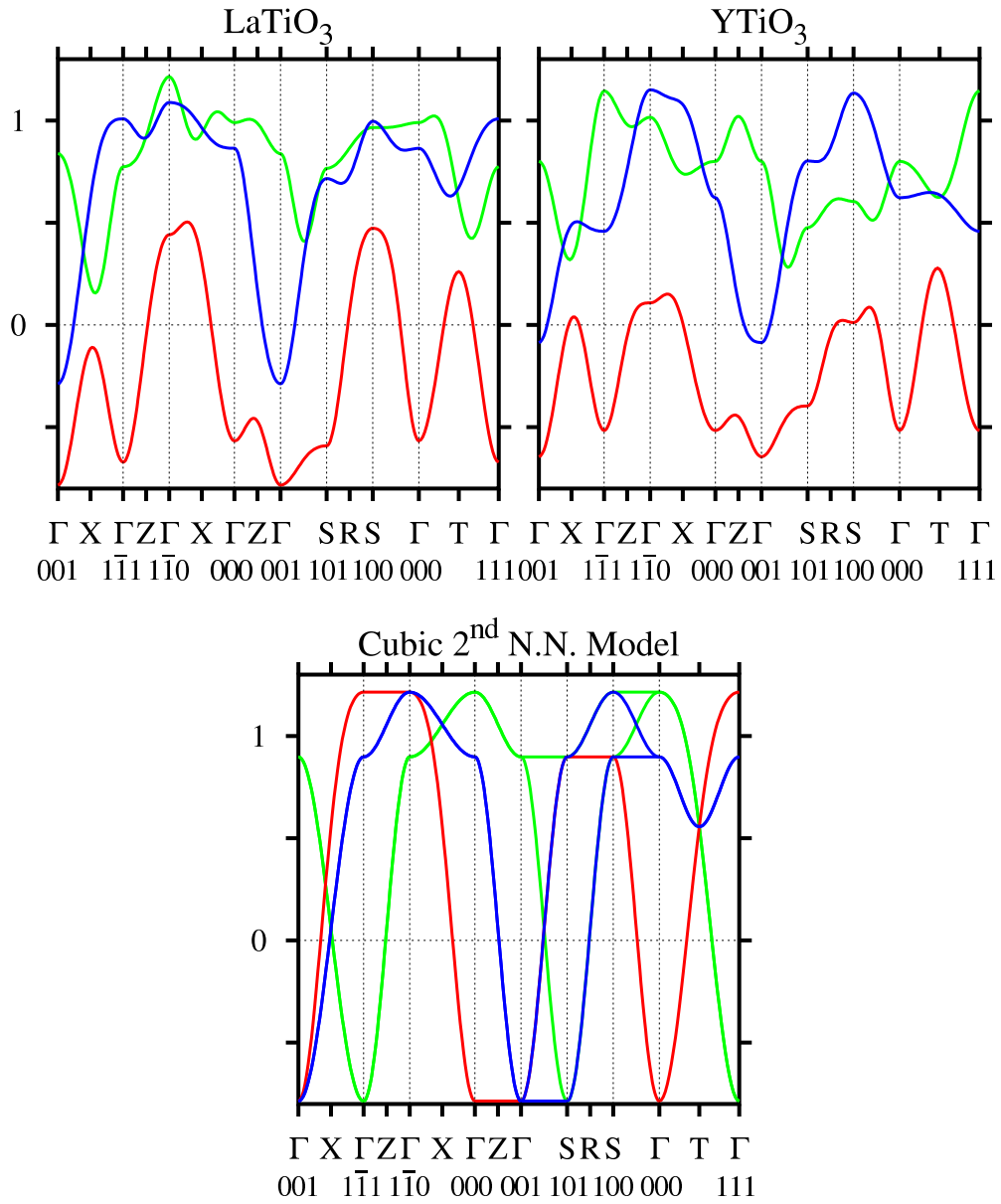

Figure 29. Bandstructures in the pseudo-cubic BZ (figure 9). For the titanates, the red band (I) is the same as in figure 27, and the green (II) and blue (III) bands are identical with those in figure 28, but folded out. The hybridization between II and III is neglected. The bands are described by equation (1) with the parameters given in tables 17 and 18. For the cubic model, given by equation (2) with $t_\pi = -250$ meV, $t'_\sigma/t_\pi = r = 0.34$ and $t_\delta = 0$, the red band (I) is xy, the green bands are $\varepsilon_{yz}\left(\bar{\mathbf{k}}-\pi\pi\pi\right)$ and $\varepsilon_{xz}\left(\bar{\mathbf{k}}-\pi\pi\pi\right)$, and the blue bands are $\varepsilon_{yz}\left(\bar{\mathbf{k}}-00\pi\right)$ and $\varepsilon_{xz}\left(\bar{\mathbf{k}}-00\pi\right)$. These yz and xz bands are degenerate in the (± 110) planes containing 00π, 000, $\pm\pi\pi 0$, and $\pm\pi\pi\pi$. Here, they therefore equal their respective averages, namely $\varepsilon\left(\bar{\mathbf{k}}-\pi\pi\pi\right)$, the green $yz+xz$ band II, and $\varepsilon\left(\bar{\mathbf{k}}-00\pi\right)$, the blue $yz-xz$ band III. The cubic bands are roughly those of $SrVO_3$ and are shown along the same path in reciprocal space as in figure 11. The unit along the abscissa is π.

Table 19. Width of the lowest band, I, in eV and the ratio $W_{\rm I}/W$

	$SrVO_3$[42]	$CaVO_3$[43]	$LaTiO_3$[44]	$LaTiO_3$[12]	$YTiO_3$[20]
$W_{\rm I}$	2.85	1.80	1.40	1.30	0.95
$W_{\rm I}/W$	1.00	0.74	0.63	0.62	0.50

differences in dispersion and position of band 3 might be the underlying cause for the differences in the onset of optical absorption calculated in subsection 5.5 and discussed most recently by Rückamp *et al.* [63].

Avoided crossings give rise to small tongues in the joint density of states,

$$J_f(\omega) = \sum\nolimits_{\vec{\mathbf{k}}} \delta\left\{\omega + \varepsilon_{\rm I}\left(\vec{\mathbf{k}}\right) - \varepsilon_f\left(\vec{\mathbf{k}}\right)\right\},$$

extending down to ∼0.15 eV, but the strong onset of $J_f(\omega)$ occurs at higher energies: at 0.24 eV in $LaTiO_3$, and at 0.33 eV in $YTiO_3$. This relatively large gap is due to the combined effects of orbital order, strong hopping from orbital 1 to orbitals 2 and 3, and comparatively weak hopping between orbitals 1 (table 11). This gives band I a relatively small width, and it causes orbital I to have a much lower energy (0.7 eV) than orbitals II and II. This energy is *the number of nearest neighbours* times twice a typical hopping integral between orbital 1 and orbital 2 or 3, times some reduction factor due to the localization of the extended Wannier functions. This may be realized from figure 26 and the discussion given at the beginning of this section. Even in the basis of xy, yz, xz orbitals, the inter-orbital hopping increases strongly along the series, a fact mentioned in connection with table 6. Going now the crystal-field basis dramatically enhances inter-orbital hopping. Specifically, the ratio τ defined in equation (38) is larger for $YTiO_3$ than for $LaTiO_3$ (table 11). This is what makes $YTiO_3$ ferromagnetic *and* what tends to make the relative width of band I small.

The pseudo-gap penetrates the density of states in figure 18 better in $YTiO_3$ than in $LaTiO_3$, because there is less indirect band overlap in $YTiO_3$. The chemical reason is that the maxima of band I between Γ_o $\pi\bar{\pi}0$ and X_o $\frac{\pi}{2}\frac{\bar{\pi}}{2}0$, near S_o $\pi 00$, and at T_o $\frac{\pi}{2}\frac{\pi}{2}\frac{\pi}{2}$ are pushed down by the A $d_{3z^2_{111}-1}$ and d_{xy} characters, as was demonstrated in figure 12. In terms of effective hopping integrals, this is what makes $t^{001}_{yz,yz}$ in $YTiO_3$ anomalously small, as was explained in connection with equation (5) and referred to many times. This then points to the common reason why $YTiO_3$ is ferromagnetic, both according to super-exchange theory and in the Stoner band picture. Finally we can read off the width, $W_{\rm I}$, of the lowest band in figures 10 and 17, and list them in table 19 together with the relative subband widths $W_{\rm I}/W$.

8. Summary and Outlook

By means of Wannier functions obtained from *ab initio* density-functional (LDA) calculations we have studied the series of orthorhombic perovskites ABO_3 = $SrVO_3$, $CaVO_3$, $LaTiO_3$,and $YTiO_3$ in which, under the influence of an increasing $GdFeO_3$-type distortion, the single B t_{2g} electron becomes increasingly localized and undergoes a Mott transition between $CaVO_3$ and $LaTiO_3$. The energy bands in figure 1 and the Wannier functions for the oxygen $2p$ band in figures 5 and 6 show that covalency between the occupied O p and the empty large-cation A s and, in particular, d states is an important mechanism of this distortion (figure 7). The A d states $pd\sigma$-bond with the *same* oxygen p orbitals as those with which the empty B t_{2g} states $pd\pi$-bond and, as a result, the B t_{2g} Wannier functions have, not only oxygen $pd\pi$ but also residual A $d_{3z^2_{111}-1}$ and d_{xy} characters (figures 8, 12 and 15). This situation is very different from the one in e^1_g perovskites such as $LaMnO_3$, where the e_g orbitals $pd\sigma$-bond –and thus cause strong JT distortion– to *different* oxygen orbitals than those bonding to A d. Through the series of t^1_{2g} perovskites, the increasing misalignment of the xy, yz,and zx orbitals and the theft of O p character by the A ions lead to a decrease of the t_{2g} bandwidth, W, by about 50 % (tables 6 and 8 and figures 10 and 11), and the increasing A $d_{3z^2_{111}-1}$ and d_{xy} character leads to increasing inter-orbital coupling, splitting of the t_{2g} degeneracy (figure 14 and equations (17)–(20)), and to the development of a lowest subband (figures 25, 27 and 29) with a width, W_I, which decreases from W to $\frac{1}{2}W$ (table 19). To the LDA low-energy Hamiltonian defined by the t_{2g} Wannier functions we have finally added the on-site Coulomb interaction terms.

In order to calculate the correlated spectral densities and, hence, to study the Mott transition, Pavarini *et al.* [21] solved this Hubbard Hamiltonian in the single-site dynamical mean-field approximation (DMFT) at temperatures well above those where magnetic orderings occur in the titanates. The critical values, U'_c, of the average Coulomb interaction, U', required to drive the materials into the Mott insulating state decrease by a factor two through the series (figure 19 and table 10), thus reflecting not only the decreasing W, but also the increasing crystal-field splittings and the decreasing width of the lowest subband. For the titanates, the Mott transition occurs essentially in the lowest subband, that is, the orbital degeneracy decreases from 3 in $SrVO_3$ to $\sim$1 in the titanates (figure 21) and, for $U' \geq U'_c$, the occupied orbital is the Wannier function for the lowest crystal-field level. Using $U' \approx 3.7\,\mathrm{eV}$ for all four materials, the spectral densities in figure 20 not only reproduce the trend that $SrVO_3$ and $CaVO_3$ are metals with increasing mass enhancements and $LaTiO_3$ and $YTiO_3$ Mott insulators with increasing gaps, but also the quantitative features of photoemission and BIS spectra. In the titanates, the orbital polarization is nearly complete (0.91 in $LaTiO_3$ and 0.96 in $YTiO_3$) and the crystal-field splittings and orbital orders agree well with recent experiments. The difference between the orbital orders in La and Y titanate (figure 16) is quantitative, rather than qualitative, and is caused by the dominating A character being $d_{3z^2_{111}-1}$ in $LaTiO_3$ and being d_{xy} in the more heavily $GdFeO_3$-type distorted $YTiO_3$.

The difference in the onsets of optical conductivities in the titanates is reasonably well accounted for (figure 23). The volume reduction needed to make $LaTiO_3$ a metal is reproduced and that for $YTiO_3$ is predicted (figure 22).

In order to calculate the magnetic orderings in the insulators at low temperature we have assumed complete orbital order and have applied conventional super-exchange theory to our Hubbard Hamiltonians. In accord with experiments, we find $LaTiO_3$ to be a G-type antiferromagnet with fairly isotropic exchange coupling constants, but with values three times smaller than those obtained by from spin-wave spectra (table 12). We correctly find $YTiO_3$ to be a ferromagnet with very small coupling constants, but their anisotropy is too large (table 11 and figure 24). The reason for the trend from antiferro- towards ferromagnetism with increasing $GdFeO_3$-type distortion is that the hopping between the nearest-neighbour Wannier functions for the lowest crystal-field level decreases compared with the hoppings to the higher-level Wannier functions. This is also the mechanism for creating a lowest subband of reduced width. At the point where the super-exchange coupling becomes weak – because it changes sign – the JT distortion becomes the controlling factor for the magnetic order, although it hardly influences the orbital order. We find that $YTiO_3$ without JT distortion should be a C-type antiferromagnet and that $YTiO_3$ at 16 GPa pressure, where the JT distortion is strongly reduced, should become an A-type antiferromagnet below ~ 100 K (table 16).

Our results concerning the role of the $GdFeO_3$-type and JT distortions for the crystal-field splittings, orbital orders, and magnetic couplings are in accord with those obtained from studies of model Hamiltonians by Mochizuki and Imada [29]. Both theoretical works, together with an increasing number of experimental works, point to a crystal-field splitting in the titanates at the order of 200 meV, *i.e.* much larger that kT and the spin-orbit splitting. This puts doubts on the applicability to the titanates of the recent orbital-liquid theory [16, 17], which is based on the assumption the t_{2g} orbitals are nearly degenerate. Although the picture we have presented appears consistent from the chemical point of view, the fine balance between O-A, O-B, A-B, and B-B covalencies is hardly reproduced with sufficient accuracy to describe the magnetic exchange couplings well in these t_{2g}^1 materials. This may be due to the LDA, to our use of the atomic-spheres approximation to generate the LDA potentials, and to our NMTO t_{2g} Wannier functions being too extended for use as basis functions for the Hubbard model. Moreover, our assumption of complete orbital order for $LaTiO_3$ may be too crude considering the fact that the measured magnetic moment is only $0.57\,\mu_B$ in this material. Only other types of calculations, for instance spin-polarized LDA+DMFT calculations for $LaTiO_3$, can throw light on this in the future.

In order to prepare the grounds for future experimental and theoretical clarification, and also to ease the applicability of the present theoretical work to the wealth of interesting, similar t_{2g} systems, we have presented a great deal of detail about why our results come out the way they do, and we have tabulated the LDA on-site and hopping matrix elements (tables 1, 2, 4, and 5). Moreover, in section 3.6 we have given an analytical expression in the $\mathbf{k}+\mathbf{Q}$ representation for the orthorhombic Hamiltonian,

into which the self-energy may be included, once it has been extracted from calculations or experiments. In the present LDA+DMFT calculations the **k**-dependence of the self-energy was totally neglected, but our success in explaining the Mott transition in the series of t_{2g}^1 perovskites indicates that, for these systems, the single-site DMFT is indeed a good approximation. On the other hand, since the $GdFeO_3$-type distortion severely influences not only the on-site matrix elements, but also the hopping integrals in t_{2g} systems, this might induce a **k**-dependence of the self-energy not found in e_g systems. In the near future it would be useful to get hold of the self-energy matrix for *real* frequencies, because this would give us the correlated bandstructure (**k**-dependent spectral function), which could then be compared with for instance angle-resolved photoemission and dHvA experiments. For metals, theoretical work on the electron liquid [71] indicates that the self-energy does have a significant **k**-dependence, and that could be checked. In the future it may be possible to use cluster-DMFT calculations to evaluate the **k**-dependence of the self-energy for real systems.

In this paper we have also demonstrated the use of the new NMTO downfolding technique [30] as a tool for generating truly minimal basis sets, Wannier functions in particular. It is of course possible to generate sets of Wannier functions which span also the oxygen p and transition-ion e_g LDA bands as needed when describing high-energy excitations. As another extreme, it is sometimes possible to downfold to even fewer than three t_{2g} functions and, in such cases, discover tendencies towards symmetry breaking, which may be exploited by the Coulomb correlations (figure 25). We may, in general, follow the localization process more closely and accurately by generating the Wannier functions self-consistently during the cause of a DMFT calculation [51].

We are convinced that the rich physics of the materials studied in this paper, as well as the computational techniques used to do so, will remain active fields of research for years to come.

Acknowledgments

We are indebted to A. I. Lichtenstein, A. Georges, S. Biermann, and A. Poteryaev for having initiated and taken part in this research at its earlier stages. Our interest in these materials was aroused by G. Khaliullin, B. Keimer, and C. Ulrich. The use of software developed by T. Saha-Dasgupta as well as discussions with her are gratefully acknowledged. With Olle Gunnarsson and Erik Koch we have enjoyed many enlightening discussions and from them we have received more fruitful suggestions than from anyone else. I. Loa and K. Syassen informed us about their high-pressure experiments and allowed us to make use of their results prior to publication. Contacts with M. Grüninger, D. D. Sarma and K. Maiti are also acknowledged. N. A. Spalding kindly referred us to the work of Woodward. Finally, we would like to thank the KITP Santa Barbara for hospitality (NSF Grant No. PHY99-07949) and the INFM-Iniziativa Calcolo Parallelo for support.

Appendix A. NMTO basis sets

The Nth-order muffin-tin orbitals (NMTO) method [30] is more intelligible, flexible, and accurate than its predecessor, the linear muffin-tin orbitals (LMTO) method [41], a so-called fast band-structure method. In the present paper, we use the NMTO method for generation of localized Wannier functions for the Kohn-Sham band-structure problem.

The method constructs a set of local-orbital basis functions which span the solutions of Schrödinger's equation –actually, the (scalar) Dirac equation– for a local potential, written as a superposition, $\sum_R v_R\left(|\mathbf{r}-\mathbf{R}|\right)$, of spherically symmetric potential wells with ranges s_R, a so-called overlapping muffin-tin potential. This is done by first solving the radial equations (numerically) to find $\varphi_{Rl}\left(\epsilon_n,|\mathbf{r}-\mathbf{R}|\right)$ for all angular momenta, l, with non-vanishing phase-shifts, for all potential wells, R, and for a chosen set of energies spanning the region of interest, $\epsilon_n=\epsilon_1,....,\epsilon_N$. These energies are the ones shown on the right-hand side of figure 4 for the oxygen $2p$ bands and on the right-hand side of figure 10 for the B $3d\left(t_{2g}\right)$ bands.

The partial-wave channels, Rlm, are now partitioned into *active* and passive. The active ones are those for which one wants to have orbitals in the basis set; *i.e.,* they are the chosen one-electron degrees of freedom. For the red bands in figures 3 and 10, the B $d\left(t_{2g}\right)$ channels are active, while for the red bands in figure 4, the oxygen p channels are active. In all figures, the black bands are calculated with a large NMTO set having the O p, B spd, and A spd channels active.

For each active channel, $\bar{R}\bar{l}\bar{m}$, a so-called *kinked* partial wave, $\phi_{\bar{R}\bar{l}\bar{m}}\left(\epsilon_n,\mathbf{r}\right)$, is constructed from *all* the partial waves, $\varphi_{Rl}\left(\epsilon_n,|\mathbf{r}-\mathbf{R}|\right)Y_{lm}\left(\widehat{\mathbf{r}-\mathbf{R}}\right)$, inside the potential-spheres, and from *one* solution, $\psi_{\bar{R}\bar{l}\bar{m}}\left(\epsilon_n,\mathbf{r}\right)$, of the wave-equation in the interstitial, a so-called screened spherical wave. The construction is such that the kinked partial wave is a solution of Schrödinger's equation at energy ϵ_n in all space, except at so-called hard screening-spheres –which are concentric with the potential-spheres, but have no overlap– where it is allowed to have radial kinks in the *active* channels. It is now clear that if we can form a linear combination of such kinked partial waves with the property that all kinks cancel, we have found a solution of Schrödinger's equation with energy ϵ_n. In fact, this kink-cancellation condition leads to the classical method of Korringa, Kohn and Rostoker [72] (KKR), but in a general, so-called screened representation and valid for overlapping MT potentials to leading order in the potential overlap. The screened KKR equations are a set of energy-dependent, homogeneous linear equations, with a matrix, $K_{\vec{R}\vec{l}\vec{m},\bar{R}\bar{l}\bar{m}}\left(\varepsilon\right)$, whose rows and columns are labelled by the active channels. We do not solve this set of secular equations, but proceed a bit differently:

The major computational task in the screened KKR and NMTO methods is to construct the set of *envelope* functions for the kinked partial waves, the set of screened spherical waves, as superpositions of spherical Hankel functions. This is known as the real-space calculation of the screened structure-matrix, which is the non-diagonal part of the KKR matrix, $K\left(\epsilon_n\right)$. Now, $\psi_{\bar{R}\bar{l}\bar{m}}\left(\epsilon_n,\mathbf{r}\right)$ must join smoothly onto all the *passive* partial waves, *i.e.* it must have the proper phase shifts. For all the *active* channels,

except the eigenchannel, $\bar{R}\bar{l}\bar{m}$, it can be forced to *vanish* at the screening spheres, and it is this confinement which makes it *localized,* provided that this is possible with the actual choices of energy, partition between active and passive channels, and screening-radii, a_R. Since the screened spherical wave is required to vanish merely for the *other* active channels, but not for the eigenchannel, it is an impurity solution for the hard-sphere solid. In order to obtain maximal localization, the hard spheres are usually chosen to be nearly touching. The passive channels are said to be *downfolded.*

As an example, let us consider the set of O $2p$ kinked partial waves at the energy ϵ_1 in figure 4 and assume that this set equals the set of NMTOs shown in figures 5 and 6, which is approximately true. This set consists of the three p_x, p_y, and p_z orbitals on *all* oxygens in the solid. The O1 p_x orbital shown in the 3rd column and upper row of figure 5 therefore satisfies the following conditions: at its *own* site, the p_y- and p_z-projections vanish, at all *other* oxygen sites in the solid, *all* three oxygen p-projections vanish, and all *remaining* projections, *i.e.* O *sd*.., La *spdf*.., and Ti *spd*.., are smooth solutions of Schrödinger's equation at energy ϵ_1. Also the oxygen p-projections are solutions of Schrödinger's equation at energy ϵ_1, but they have kinks at the screening-spheres.

Another example are the B d_{xy}, d_{yz}, and d_{xz} NMTOs shown figure 8. In order to generate the orbitals with the convention used in the second row, the active channels were specified simply as d_{xy}, d_{yz}, and d_{xz} on each of the four B-sites, with x, y, and z referring to the *global* axes. This is possible when the structure is nearly cubic, because then the orbitals can adjust their orientation due to the freedom of, say, the d_{xy}-NMTO to contain any on-site character, except d_{yz} and d_{xz}, such as for instance $d_{x^2-y^2}$ and d_{3z^2-1}.

The set of NMTOs is formed as a superposition of the kinked-partial-wave sets for the energies, $\epsilon_1, ..., \epsilon_N$:

$$\chi^{(N)}_{\vec{R}\vec{l}\vec{m}}(\mathbf{r}) = \sum_{n=0}^{N} \sum_{\bar{R}\bar{l}\bar{m}} \phi_{\bar{R}\bar{l}\bar{m}}(\epsilon_n, \mathbf{r})\, L^{(N)}_{n;\bar{R}\bar{l}\bar{m},\vec{R}\vec{l}\vec{m}}. \tag{A.1}$$

Note that the size of this NMTO basis set is given by the number of active channels and is independent of the number, $N+1$, of energy points. The coefficient matrices, $L^{(N)}_n$, in equation (A.1) are determined by the condition that the set of NMTOs span the solutions, $\Psi_i(\varepsilon_i, \mathbf{r})$, of Schrödinger's equation with an error

$$\begin{aligned} \Psi^{(N)}_i(\mathbf{r}) - \Psi_i(\varepsilon_i, \mathbf{r}) &= c^{(N)}(\varepsilon_i - \epsilon_0)(\varepsilon_i - \epsilon_1)...(\varepsilon_i - \epsilon_N) \\ &\quad + o\left((\varepsilon_i - \epsilon_0)(\varepsilon_i - \epsilon_1)...(\varepsilon_i - \epsilon_N)\right). \end{aligned} \tag{A.2}$$

This is polynomial approximation for the Hilbert space of Schrödinger solutions and $L^{(N)}_n$ are the coefficients in the corresponding Lagrange interpolation formula. An NMTO with $N > 0$, has no kinks, but merely discontinuities in the $(2N+1)$st radial derivatives at the screening-spheres for the active channels.

The Lagrange coefficients, $L^{(N)}_n$, as well as the Hamiltonian and overlap matrices in the NMTO basis are expressed solely in terms of the KKR resolvent, $K(\varepsilon)^{-1}$, and its first energy derivative, $\dot{K}(\varepsilon)^{-1}$, evaluated at the energy mesh, $\varepsilon = \epsilon_1, ..., \epsilon_N$. Variational

estimates of the one-electron energies, ε_i, such as the red bands in figures 3, 4, and 10 may be obtained from the generalized eigenvalue problem,

$$\left(\left\langle \chi^{(N)} \left| \mathcal{H} \right| \chi^{(N)} \right\rangle - \varepsilon_i \left\langle \chi^{(N)} \mid \chi^{(N)} \right\rangle\right) \mathbf{v}_i = \mathbf{0},$$

with

$$\mathcal{H} \equiv -\Delta + \sum_R v_R \left(|\mathbf{r} - \mathbf{R}| \right),$$

or as the eigenvalues of the one-electron Hamiltonian matrix,

$$H^{LDA} = \left\langle \chi^{(N)\perp} \left| \mathcal{H} \right| \chi^{(N)\perp} \right\rangle \tag{A.3}$$

in the basis of *symmetrically orthonormalized* NMTOs:

$$\left| \chi^{(N)\perp} \right\rangle \equiv \left| \chi^{(N)} \right\rangle \left\langle \chi^{(N)} \mid \chi^{(N)} \right\rangle^{-\frac{1}{2}}. \tag{A.4}$$

The prefactor, $c^{(N)}$, of the leading error of an NMTO set (A.2) depends on the size of the set, and the larger the set, the smaller the prefactor. For that reason we have not bothered to indicate the energy mesh used for the black bands in figures 3, 4, and 10. Assuming that they are exact, the red bands will touch the black bands quadratically at the energy points used to generate the red-band set. That they touch rather than cross is by virtue of the variational principle.

For an isolated set of bands, like the oxygen p-bands or the B t_{2g}-bands, and for energy meshes spanning the range of those bands, as the number of energy points increases and the distances between them decrease, the set of truly minimal NMTOs will converge and be exact. Upon orthonormalization, they will therefore form a set of localized Wannier functions.

The construction of a minimal NMTO basis set is different from standard Löwdin downfolding. The latter partitions a *given*, large (say orthonormal) basis into active (A) and passive (P) subsets, then finds the downfolded Hamiltonian matrix as:

$$\langle A\left(\varepsilon\right) \left| \mathcal{H} \right| A\left(\varepsilon\right) \rangle = \langle A \left| \mathcal{H} \right| A \rangle + \langle A \left| \mathcal{H} \right| P \rangle \left\langle P \left| \varepsilon - \mathcal{H} \right| P \right\rangle^{-1} \langle P \left| \mathcal{H} \right| A \rangle, \tag{A.5}$$

and finally removes the ε-dependence of the downfolded basis by *linearizing* $\left\langle P \left| \mathcal{H} - \varepsilon \right| P \right\rangle^{-1}$ and treating the term linear in ε as an overlap matrix. Obviously, since the NMTO set is exact at $N+1$ energy points, it is more accurate. Nevertheless, since truly minimal NMTOs can be fairly complicated functions, we often use equation (A.5) to *interpret* their (orthonormalized) Hamiltonian in terms of the Hamiltonian represented in a larger basis set whose orbitals are simpler and more localized.

For crystals, all calculations except the generation of the screened structure matrix are performed in the Bloch $\mathbf{k}$-representation

$$\chi^{(N)}_{\bar{R}\bar{l}\bar{m}}\left(\mathbf{k}, \mathbf{r}\right) = \frac{1}{\sqrt{L}} \sum_T \chi^{(N)}_{\bar{R}\bar{l}\bar{m}}\left(\mathbf{r} - \mathbf{T}\right) e^{i\mathbf{k}\cdot\left(\bar{\mathbf{R}}+\mathbf{T}\right)}, \tag{A.6}$$

where T labels the L $(\to \infty)$ lattice translations and $\bar{R}$ the active sites in the primitive cell. In order to obtain the orbitals and the Hamiltonian in configuration space, Fourier-transformation over the Brillouin zone is performed.

In the present paper, the orbitals shown are NMTOs *before* orthonormalization (A.4) because they are (slightly) more localized than the orthonormalized ones. The hopping integrals and on-site elements given in the tables are of course matrix elements of the *orthonormalized* Hamiltonian (A.3).

Appendix B. Technical details of the LMTO-ASA potential calculations

Since our present NMTO code is not self-consistent, we used the current Stuttgart TB-LMTO-ASA code [73] to generate the LDA potentials. Such a potential in the atomic-spheres approximation (ASA) is an overlapping MT-potential, like the one handled by the NMTO method, but with the relative overlaps,

$$\omega_{RR'} \equiv \frac{s_R + s_{R'}}{|\mathbf{R} - \mathbf{R}'|} - 1, \tag{B.1}$$

limited to about 20%. This limitation comes from the LMTO-ASA+cc method[41], which solves Schrödinger's equation by treating the overlap as a perturbation (the socalled combined-correction term, cc) *and* uses screened spherical waves of *zero* kinetic energy in the s-interstitial. Poisson's equation is solved for the output charge density, spherically symmetrized inside the *same* atomic s-spheres. For a given potential, the hopping integrals obtained with the NMTO method are more accurate than those obtained with the LMTO method, first of all because the NMTOs do not use the zero-kinetic-energy approximation in the interstitial region and, secondly, because we use $N > 1$ with well-chosen energy meshes. However, since the on-site matrix elements of the LDA Hamiltonian (A.3) turned out to be crucial for the present study, it is possible that our ASA treatment of the potential leads to an *under*estimation of the electrostatic contribution to the crystal field.

We now specify our computational set-up. The radii of the potential spheres, s_R, were dictated by our use of the LMTO-ASA method to generate the LDA potentials. In order to limit the overlaps defined by equation (B.1), interstital –or empty– spheres (E) were inserted in the non-cubic structures. Table B1 gives the radii of the potential spheres. As a result, the overlap between atomic spheres was <16%, between atomic and empty spheres <18%, and between empty spheres <20%. We used the guidance given by the current version of the code in choosing the potential spheres appropriately.

With these reasonably large oxygen spheres, the oxygen $2s$ electrons could be treated as part of the core. The self-consistent valence-electron densities were calculated with the LMTO bases listed in Table B2. In order to describe properly the A–O–B covalency we found it important to downfold the oxygen d partial waves, rather than to neglect them (*i.e.* to approximate them by spherical Bessel functions when solving Schrödingers equation, and to neglect them in the charge density). Since the LMTO calculations were used to produced the self-consistent charge densities, the energies, ϵ_{Rl}, for the linear $\phi_{Rl}, \dot{\phi}_{Rl}$ expansions were chosen at the centres of gravity of the *occupied* parts of the respective DOS Rl-projections.

Table B1. Radii s_R of potential spheres in Bohr atomic units.

ABO_3	A	B	O1	O2	E	E1	E2	E3	E4	E5
$SrVO_3$	3.97	2.29	1.77							
$CaVO_3$	3.34	2.33	1.80	1.80	1.28	1.25	1.17	1.22	1.24	
$LaTiO_3$[44]	3.37	2.51	1.90	1.90	1.50	1.41	1.31	1.29	1.19	1.13
$LaTiO_3$[12]	3.31	2.52	1.93	1.93	1.61	1.49	1.42	1.28	1.08	1.07
$YTiO_3$	2.95	2.51	1.92	1.90	1.93	1.83	1.48	1.44		

Table B2. LMTO basis sets used in the self-consistent calculation of LDA potential. (l) means that the l-partial waves were downfolded within in the LMTO-ASA+cc.

	A	B	O1	O2	E	E1	E2	E3	E4	E5
$SrVO_3$	$s(p)d(f)$	spd	$(s)p(d)$							
$CaVO_3$	$s(p)d$	spd	$(s)p(d)$	$(s)p(d)$	$s(p)$	$s(p)$	$s(p)$	$s(p)$	$s(p)$	
$LaTiO_3$	$s(p)df$	spd	$(s)p(d)$	$(s)p(d)$	$s(p)$	$s(p)$	$s(p)$	$s(p)$	$s(p)$	$s(p)$
$YTiO_3$	$s(p)d(f)$	spd	$(s)p(d)$	$(s)p(d)$	$s(pd)$	$s(pd)$	$s(p)$	$s(p)$		

With the benefit of hindsight, we should have inserted the 12 E spheres above the octahedron edges also in cubic $SrVO_3$. That would have reduced $s_{\rm Sr}$ to 3.46 a.u., a value closer to those for the other systems. As a result, the t_{2g} bandwidth for cubic $SrVO_3$ would be reduced by 8%. This seems to be the largest computational "error" of the present calculations. This inaccuracy only concerns cubic $SrVO_3$ and it reduces the decrease of rms bandwidth (tables 6 and 8) when going from $SrVO_3$ to $CaVO_3$, from 19 to 11%. Hence, the trend that $CaVO_3$ is a more correlated metal than $SrVO_3$ is somewhat diminished. All remaining results, such as those concerning the Mott transition and the properties of the titanates, of course remain valid.

After completion of the calculations, we also found that the optimal trade off between the errors caused by the confinement of the O $2s$ electrons to the sphere and by the overlap of spheres, is obtained with a larger oxygen radius, 2.04 a.u.. This leads to a small downwards shift of the O $2p$ band and a 4% decrease of the t_{2g} bandwidth, W, for all four materials. Since all materials are influenced the same way, and since our value of U was fitted relatively to W, this error has no effect, except that it might influence the sensitive values of the exchange-coupling constants calculated in section 6.

Finally, in the NMTO calculations, the hard-sphere radii, a_R, for the active channels were chosen as $0.7s_R$.

References

[1] Goodenough John B 1955 *Phys Rev* **100** 564; 1963 *Magnetism and the Chemical Bond* (Wiley, New York)

[2] Imada M, Fujimori A and Tokura Y 1998 *Rev. Mod. Phys.* **70** 1039

[3] Mochizuki M and Imada M 2004 *New J. Phys.* **6** 154

[4] Makino H, Inoue I H, Rozenberg M J, Hase I, Aiura Y and Onari S 1998 *Phys. Rev.* B **58** 4384

[5] Inoue I H, Hase I, Aiura Y, Fujimori A, Haruyama Y, Maruyama T and Nishihara Y 1995 *Phys. Rev. Lett.* **74** 2539; Inoue I H, Goto O, Makino H, Hussey N E and Ishikawa M 1998 *Phys. Rev.* B **58** 4372

[6] Aiura Y, Iga F, Nishihara Y, Ohnuki H and Kato H 1993 *Phys. Rev.* B **47** 6732

[7] Okimoto Y, Katsufuji T, Okada Y, Arima T and Tokura Y 1995 *Phys. Rev.* B **51** 9581

[8] Katsufuji T, Tagouchi Y, and Tokura Y, 1997 *Phys Rev* B **56** 10145

[9] Loa I, Wang X, Syassen K, Lorenz T, Hanfland M, Roth H, and Mathis Y-L, private communication; Loa I, Wang X, Syassen K, Roth H, Lorenz T, Hanfland M, and Mathis Y-L *Preprint* cond-mat/0504383.

[10] Keimer B, Casa D, Ivanov A, Lynn J W, v. Zimmermann M, Hill J P, Gibbs D, Taguchi Y and Tokura Y 2000 *Phys. Rev. Lett.* **85** 3946

[11] Goral J P, Greedan J E and Mac Lean D A 1982 *J. Solid State Chem.* **43** 244; Goral J P and Greedan J E 1983 *J. Mag. Magn. Mater.* **37** 315; Greedan J E 1985 J. Less-Common Mat.**111** 335.

[12] Cwik M, Lorenz T, Baier J, Muller R, Andre G, Bouree F, Lichtenberg F , Freimuth A, Schmitz R, Muller-Hartmann E and Braden M 2003 *Phys. Rev.* B **68** 060401.

[13] Garrett J D, Greedan J E, and MacLean D A *Mater. Res. Bull.* 1981**16**, 145

[14] Gunnarsson O, Koch E and Martin R M 1996 *Phys. Rev.* B **54** 11026; Gunnarsson O, Koch E and Martin R M 1997 *Phys. Rev.* B **56** 1146; qualitatively similar results were obtained with DMFT by Florens S, Georges A, Kotliar G and Parcollet O 2002 *Phys. Rev.* B **66** 205102

[15] Manini N, Santoro GA, Dal Corso A and Tosatti E 2002 *Phys. Rev.* B **66** 115107

[16] Khaliullin G and Okamoto S. 2002 *Phys. Rev. Lett.* **89**, 167201; 2003 *Phys. Rev.* B **68**, 205109.

[17] Khaliullin G 2001 *Phys. Rev.* B **64** 212405

[18] Fritsch V, Hemberger J, Eremin M V, Krug von Nidda H A, Lichtenberg F and Wehn R 2002 *Phys. Rev.* B **65** 212405

[19] Hemberger J, Krug von Nidda HA, Fritsch V, Deisenhofer J, Lobina S, Rudolf T, Lunkenheimer P, Lichtenberg F, Loidl A, Bruns D, and Bühner 2003 *Phys. Rev. Lett.* **91** 066403

[20] Eitel M and Greedan J E 1986 *J. Less-Common Met.* **116** 95

[21] Pavarini E, Biermann S, Poteryaev A, Lichtenstein A I, Georges A, and Andersen O K 2004 *Phys. Rev. Lett.* **92** 176403

[22] Goodenough J B 1971 *Prog. Solid State Chem.* **5** 145

[23] Woodward P M 1997 *Acta Cryst.* B **53** 44

[24] Mochizuki M and Imada M 2003 *Phys. Rev. Lett.* **91** 167203

[25] Mizokawa T and Fujimori A 1996 *Phys. Rev.* B **54** 5368

[26] Mizokawa T, Khomskii D I and Sawatzky G A 1999 *Phys. Rev.* B **60** 7309

[27] Mochizuki M and Imada M 2001 *J. Phys. Soc. Japan* **70** 1777

[28] Mochizuki M and Imada M 2001 *J. Phys. Soc. Japan* **70** 2872

[29] Mochizuki M and Imada M 2004 *J. Phys. Soc. Japan* **73** 1833

[30] Andersen O K and Saha-Dasgupta T 2000 *Phys. Rev.* B **62** 16219 and references therein; Andersen O K, Saha-Dasgupta T, Ezhov S, Tsetseris L, Jepsen O, Tank R W, Arcangeli C, Krier G 2001 *Psi-k Newsletter* **45** 86; Andersen O K, Saha-Dasgupta T and Ezhov S 2003 *Bull. Mater. Sci.* **26** 19; Zurek E, Jepsen O and Andersen O K 2005 *Chem. Phys. Chem.* **6** 1

[31] Solovyev I, Hamada N, and Terakura K 1996 *Phys. Rev.* B **53** 7158

[32] Sawada H and Terakura K 1998 *Phys. Rev. B* **58** 6831

[33] Itoh M, Tsuchiya M, Tanaka H and Motoya K 1999 *J. Phys. Soc. Japan* **68** 2783.
[34] Akimitsu J, Ichikawa H, Eguchi N, Miyano T, Nishi M and Kakurai K 2001 *J. Phys. Soc. Japan* **70** 3475.
[35] For a review, see Georges A, Kotliar G, Kraut W and Rozenberg MJ 1996 *Rev. Mod. Phys.* **68** 13
[36] Anisimov V, Poteryaev A, Korotin M, Anokhin A and Kotliar G, 1997 *J.Phys: Condens. Matter* **9**, 7359; Lichtenstein A I and Katsnelson M I 1998 *Phys. Rev.* B **57** 6884; Held K, Nekrasov I A, Keller G, Eyert V, Blümer N, McMahan A K, Scalettar R T, Pruschke Th, Anisimov V I, and Vollhardt D 2003 *Psi-k Newsletter* **56** 65; Kotliar G and Vollhardt D 2004 *Physics Today* **57** 53
[37] Nekrasov I A, Held K, Blümer N, Poteryaev A I, Anisimov V I and Vollhardt D 2000 *Eur. Phys. J.* B **18** 55
[38] Sekiyama A, Fujiwara H, Imada S, Suga S, Eisaki H, Uchida S I, Takegahara K, Harima H, Saitoh Y, Nekrasov I A, Keller G, Kondakov D E, Kozhevnikov A V, Pruschke Th, Held K, Vollhardt D, and Anisimov V I 2004 *Phys. Rev. Lett.* **93** 156402
[39] Craco L, Laad M S, Leoni S and Müller-Hartmann E 2004 *Phys. Rev.* B **70** 195116
[40] Ulrich C, Khaliullin G, Okamoto S, Reehuis M, Ivanov A, He H, Taguchi Y, Tokura Y and Keimer B 2002 *Phys. Rev. Lett.* **89** 167202
[41] Andersen O K and Jepsen O 1984 *Phys. Rev. Lett.* **53**, 2571.
[42] Rey MJ, Dehaudt Ph, Joubert J C, Lambert-Andron B, Cyrot M and Cyrot-Lackmann F 1990 *J. Solid State Chem.* **86** 101
[43] Jung M H and Nakotte H unpublished
[44] MacLean D A, Ng H N and Greedan EG 1979 *J. Solid State Chem.* **30** 35
[45] Mahadevan P, Shanthi N and Sarma D D 1996 *Phys. Rev.* B **54** 11199
[46] Inoue I H, Bergeman C, Hase I and Julian SR 2002 *Phys. Rev. Lett.* **88** 236403
[47] Haverkort MW, Hu Z, Tanaka A, Ghiringhelli G, Roth H, Cwik M, Lorenz T, Schuessler-Langeheine C, Streltsov S V, Mylnikova A S, Anisimov V I, de Nadai C, Brookes N B, Hsieh H H, Lin H J, Chen C T, Mizokawa T, Taguchi Y, Tokura Y, Khomskii D I and Tjeng L H 2005 *Phys. Rev. Lett.* **94** 056401
[48] Hirsch J E and Fye R M 1986 *Phys. Rev. Lett.* **56** 2521
[49] Gubernatis J E, Jarrel M, Silver R N and Sivia DS 1991 *Phys. Rev.* B **44** 6011
[50] Kanamori J 1963 *Prog. Theor. Phys.* **30** 275; Brandow B H 1977 *Adv. Phys.* **26** 651; Fresard R and Kotliar G 1997 *Phys. Rev.* B **56** 12909
[51] Anisimov V I, Kondakov D E, Kozhevnikov A V, Nekrasov I A, Pchelkina Z V, Allen J W, Mo S.-K, Kim H.-D, Metcalf P, Suga S., Sekiyama A, Keller G, Leonov I, Ren X, and Vollhardt D 2005 *Phys. Rev. B* **71** 125119
[52] Koch E, Gunnarson O and Martin R M 1999 *Phys. Rev.* B **60** 15714
[53] Fujimori A, Hase I, Nakamura M, Namatame H, Fujishima Y, Tokura Y, Abbate M, de Groot F M F, Czyzyk M T, Fuggle J C, Strebel O, Lopez F, Domke M and Kaindl G, 1992 *Phys. Rev.* B **46** 9841; Morikawa K, Mizokawa, T Fujimori A, Taguchi Y and Tokura Y 1996 *Phys. Rev.* B **54** 8446; Fujimori A, Hase I, Namatame H, Fujishima Y, Tokura Y, Eisaki H and Uchida S, Takegahara K, and de Groot FMF 1992 *Phys. Rev. Lett.* **69** 1796
[54] Bocquet AE, Mizokawa T, Morikawa K, Fujimori A, Barman SR, Maiti K, and Sarma DD 1996 *Phys. Rev. B* **53** 1161
[55] Liebsch A 2003 *Phys. Rev. Lett.* **90** 096401
[56] Maiti K, Sarma D D, Rozenberg M J, Inoue I H, Makino H, Goto O, Pedio M and Cimino R 2001 *Europhys. Lett.* **55** 246
[57] Khaliullin G and Maekawa S 2000 *Phys. Rev. Lett.* **85** 3950
[58] Kiyama T and Itoh M 2003 *Phys. Rev. Lett.* **91** 167202
[59] Kubota M, Kakao H, Murakami Y, Taguchi Y, Iwama M and Tokura Y 2004 *Phys Rev* B **70** 245125
[60] Iga F, M. Tsubota, Sawada M, Huang HB, Kura S, Takemura M, Yaji K, Nagira M, Kimura A, Jo T, Takabatake T, Namatame H, and Taniguchi M 2004 *Phys. Rev. Lett* **93** 257207.

[61] Nakao H, Wakabayashi Y, Kiyama T, Murakami Y, v. Zimmermann M, Hill JP, Gibbs D, Ishihara S, Taguchi Y, and Tokura Y 2002 *Phys. Rev. B* **66** 184419
[62] Crandles DA, Timusk T, Garret GD and Greedan JE 1994 *Phys. Rev.* B **49** 16207
[63] Rückamp R, Benckiser E, Haverkort MW, Roth H, Lorenz T, Freimuth A, Jongen L, Möller A, Meyer G, Reutler P, Büchner B, Revcolevschi A, Cheong SW, Sekar C, Krabbes G, and Grüninger M *New J. Phys.* **7** 144
[64] Bourab S, Vega A and Khan MA 1996 *Phys. Rev.* B **54** 11271
[65] Oudovenko V S, Palsson G, Haule K, Savrasov S Y and Kotliar G 2004 *Phys. Rev.* B **70** 125112; Haule K, Oudovenko V, Savrasov SY and Kotliar G 2005 *Phys. Rev. Lett.* **94** 036401
[66] Mahan GD 1993 *Many-particle physics* (Plenum, NY)
[67] Khurana N 1990 *Phys. Rev. Lett.* **64** 1990
[68] Pruschke Th, Cox D L and Jarrel M 1993 *Phys. Rev.* B **47** 3553
[69] Bluemer N and van Dongen P G J 2003 *Preprint* cond-mat/0303204
[70] Iliev M N, Litvinchuk A P, Abrashev M V, Popov V N, Cmaidalka J, Lorenz B and Meng R L 2004 *Phys. Rev.* B **69** 172301
[71] Takada Y 1991 *Phys. Rev.* B **43,** 5979
[72] Kohn W and Rostoker J 1954 *Phys. Rev.* **94** 111
[73] The Stuttgart TB-LMTO-ASA code, version 4.7. See: http://www.fkf.mpg.de/andersen/